UNIVERSITÀ DEGLI STUDI DI NAPOLI
"FEDERICO II"

Scuola Politecnica e delle Scienze di Base

Area Didattica di Scienze Matematiche Fisiche e Naturali

Dipartimento di Fisica "Ettore Pancini"

Laurea Magistrale in Fisica

Octupole Collectivity in ^{96}Zr from Low-Energy Coulomb Excitation with the AGATA+SPIDER Setup

Relatori:
Prof. Antonino Di Leva
Prof.ssa Adriana Nannini
Altri Relatori:
Dott.ssa Naomi Marchini
Prof. Marco Rocchini

Candidato:
Federica Ercolano
Matr. $N94000771$

Anno Accademico 2022/2023

Perché è in questo tuo vagare
Che risposte troverai
Sarai tu sulla montagna
E tu che in cima andrai.
Tratto da "Tarzan, Figlio di un uomo"

Contents

Overview

The concept of deformation in atomic nuclei is a cornerstone of nuclear physics. Multipole moments and transition strengths, which can be directly or indirectly accessed through various experimental techniques, are some of the collective observables used to study the shape of deformed nuclei. The lowest mode of surface deformation corresponds to the quadrupole one, which is the most frequent in nuclei. The octupole deformation is a rarer phenomenon in comparison but it plays a role in intriguing nuclear-structure phenomena. For this reason, it is one of the most studied topics in nuclear-structure physics. The susceptibility of an even-even nucleus to collective octupole correlations is reflected in the low energy of its first 3^- state and the enhancement of the rate of the γ–ray transition depopulating this state to the ground state ($3_1^- \rightarrow 0_1^+$). Throughout the nuclear chart, a few nuclei exhibiting strong octupole correlations have been found.

The subject of this thesis is octupole collectivity in the ^{96}Zr isotope, for which the structure of the first 3^- state has been widely debated in the literature. Previous measurements suggested that the γ–ray transition probability for the $3_1^- \rightarrow 0_1^+$ transition is one of the largest across the nuclear chart. This observation has never been reproduced by any theoretical calculations, and it is puzzling as it does not correspond to a similar increase in the neighbour isotopic chains. However, a recent study provides a significantly reduced γ–ray transition probability for the $3_1^- \rightarrow 0_1^+$ transition, which is in better agreement with state-of-the-art shell-model calculations. Nevertheless, up to now the experimental values were obtained via indirect methods.

The present work aims at extracting for the first time the $3_1^- \rightarrow 0_1^+$ γ–ray transition probability via the low-energy Coulomb-excitation technique. This technique is an experimental method to study the electromagnetic properties of low-lying nuclear states. Its basic feature is that the excitation of nuclear states is caused solely by the electromagnetic field acting between the reaction partners, while the contribution of short-range nuclear forces can be neglected. Hence, unlike in other nuclear reactions, the interaction process can be described in a model-independent way because the theory of electromagnetic interaction is well-known.

The experiment took place at the INFN Legnaro National Laboratories (LNL) with the setup composed of the γ–ray tracking spectrometer AGATA coupled with the heavy-ion

detector array SPIDER. This work reports about one of the first experiments performed with AGATA in its second campaign at LNL, and the first full low-energy Coulomb-excitation analysis performed with AGATA coupled with SPIDER.

This thesis is organized as follows: **chapter 1** focuses on the theoretical background of this work, describing the models aiming at understanding the nuclear structure. The general framework of the zirconium isotopic chain is introduced with a particular focus on ^{96}Zr. The low-energy Coulomb-excitation technique is summarised in **chapter 2**, describing the aspects relevant to the experiments. The GOSIA code, the reference code for low-energy Coulomb-excitation analysis, used in this work, is also briefly introduced. In **chapter 3**, the RBS (Rutherford Backscattering Spectrometry) measurement performed at the INFN LABEC laboratory to characterize the ^{96}Zr target employed in this work is described. The AGATA and SPIDER arrays and their acquisition system are presented in **chapter 4**. The description of the calibrations and the data-reduction procedures is provided in **chapter 5**. In **chapter 6**, the final Coulomb-excitation analysis is reported, together with the results of this work.

Chapter 1

Introduction

The atomic nucleus, discovered by Ernest Rutherford in 1911, is a quantum-mechanical system composed of Z protons and N neutrons (the nucleons), which interact via the electroweak and strong forces. The system's complexity increases with the number of nucleons, $i.e.$, with the mass number $A = N + Z$. A specific nuclear species, or *nuclide*, is indicated by the form ${}^{A}_{Z}X_{N}$, where X is the chemical symbol. The wide landscape of nuclei is well depicted in the *Chart of Nuclides* shown in figure 1.1, also called *Segrè Chart*, from the name of the Italian-American physicist Emilio Segrè who invented it.

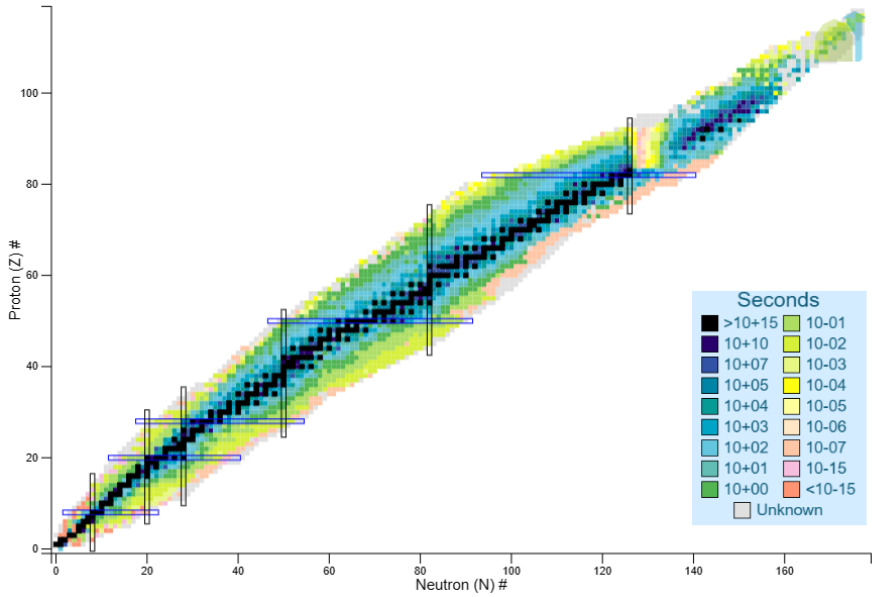

Figure 1.1: Chart of Nuclides. The nuclides are arranged according to the number of protons (vertical axis) and neutrons (horizontal axis). Colors are used to group nuclei according to their half-life, reported on the right. Adapted from Ref. [1].

Studying the atomic nucleus is challenging for two main reasons. First, the difficulty from the mathematical point of view of solving the many-body problem. The mutual interactions of the A nucleons are described by a set of coupled equations that cannot be

solved analytically. Second, the complex nature of the strong interaction. For instance, there is evidence that the nucleons can interact not only through mutual two-body forces but also through three-body forces. Such forces have no classical analogue.

This chapter provides a theoretical background for the description of the nuclear structure, with a specific focus on zirconium isotopes.

1.1 Models in Nuclear Structure

Nuclear structure models offer a simplified view of the actual nuclear structure, still containing the essentials of nuclear physics. Two criteria characterize a successful model:

1. it must agree with measured nuclear properties;
2. it must be capable of predicting additional nuclear properties.

1.1.1 Shell Model

In 1963, Maria Goeppert Mayer and Hans Jensen were awarded the Nobel Prize for their work on the Nuclear Shell Model [2, 3] (from now on in this work, simply the Shell Model). This is one of the earliest nuclear-structure models, arising from the observation that nuclei with specific numbers of protons and/or neutrons are particularly stable compared to their neighbours. These numbers, corresponding to the so-called *Shell-Closures* and known as *Magic Numbers*, were found to be: 2, 8, 20, 28, 50, 82, and 126.

The starting point of the shell model is the Schrödinger equation:

$$H\psi(\mathbf{r}_1, ..., \mathbf{r}_A) = E\,\psi(\mathbf{r}_1, ..., \mathbf{r}_A) \tag{1.1}$$

here ψ is the wave function characterizing the nuclear state, E its energy, and H the Hamiltonian operator. The nuclear Hamiltonian H, neglecting third or higher-order interaction terms, is:

$$H = \left[\sum_{i=1}^{A} \frac{\mathbf{p}_i^2}{2m_i} + \sum_{i<j}^{A} V(\mathbf{r}_i - \mathbf{r}_j) \right] \tag{1.2}$$

where m_i, $\mathbf{r}_i$ and $\mathbf{p}_i$ are mass, position and momentum of the i-nucleon, while A is the total number of nucleons. The first term is the sum of the kinetic energies of the nucleons and the second one is the two-body interaction potential. The fundamental assumptions of the shell model are [4]:

- the motion of a single nucleon is governed by a potential U caused by all the other nucleons;
- the existence of definite spatial orbits determined by the Pauli exclusion principle.

In the mean-field hypothesis, the Hamiltonian (1.2) can be separated into two components:

$$H = \left[\sum_{i=1}^{A} \frac{\mathbf{p}_i^2}{2m_i} + \sum_{i<j}^{A} V(\mathbf{r}_i - \mathbf{r}_j) + \sum_{i=1}^{A} U(\mathbf{r}_i) - \sum_{i=1}^{A} U(\mathbf{r}_i) \right] = H_0 + H_{res} \tag{1.3}$$

where

$$H_0 = \sum_{i=1}^{A} \frac{\mathbf{p}_i^2}{2m_i} + \sum_{i=1}^{A} U(\mathbf{r}_i) \tag{1.4}$$

and

$$H_{res} = \sum_{i<j}^{A} V(\mathbf{r}_i - \mathbf{r}_j) - \sum_{i=1}^{A} U(\mathbf{r}_i) \ . \tag{1.5}$$

The H_0 part is the component describing the motion of the nucleons in the nucleus, while H_{res} is the residual interaction between the nucleons, which is treated as a perturbation. With this assumption, the shell model is also called *Indipendent-Particle Model*, and the many-body problem is reduced to A one-body problems of the type:

$$h_i \, \psi^{\nu_i} = \left[\frac{\mathbf{p}_i^2}{2m_i} + U(\mathbf{r}_i) \right] \psi^{\nu_i} = \epsilon_i \, \psi^{\nu_i} \, . \tag{1.6}$$

The mean-field potential U can be described as a good approximation in terms of the Woods-Saxon potential but the eigenstates associated with this potential can be obtained only numerically. Often, the harmonic oscillator potential is used instead, for simplicity. In addition, the inclusion of a spin-orbit component, which couples the orbital angular momentum **L** with the spin of the nucleus **S**, is necessary to correctly predict the occurrence of the magic numbers. The index ν_i in (1.6) specifies the quantum state of the particle. Nuclei are represented as being filled with nucleons in discrete shells of differing total angular momentum j, parity π, and principal quantum number n. These shells are populated following the Pauli exclusion principle. The wave function ψ^{ν} for one configuration of the nucleus, solution of the Schrödinger equation

$$H_0 \, \psi^{\nu} = \sum_{i=1}^{A} \big[h_i \big] \psi^{\nu} = \sum_{i=1}^{A} \left[\frac{\mathbf{p}_i^2}{2m_i} + U(\mathbf{r}_i) \right] \psi^{\nu} = E_0 \psi^{\nu} \, , \tag{1.7}$$

is given by the Slater determinant[1] of the ψ^{ν_i}. The actual wave function ψ of the nucleus (equation 1.1) becomes:

$$\psi = \sum_{\nu} a^{\nu} \psi^{\nu} \, . \tag{1.8}$$

A detailed description of this derivation can be found in Ref. [5]. As a result, the expectation value of the energy E from the total wave function ψ will be simply the sum of the

[1] Nucleons are fermions, therefore, their wave functions must be antisymmetrized.

product of the single-particle energies ϵ_i weighted by the coefficients of the expansion. Often, the nucleus is treated as an inert core with valence nucleons, and these are limited to exist in a finite number of shells outside the core. This shell structure is a valid starting point in stable nuclei. However, as more neutrons (protons) are added, the shell structure may change, or *evolve*. As more nucleons interact, the strength of residual interactions becomes very important and, thus, in a more rigorous approach, the residual interaction cannot be neglected in the understanding of nuclear structure.

1.1.2 Collective Model

More than half a century has elapsed since the publication of one of the milestones of nuclear physics: *The coupling of nuclear surface oscillations to the motion of individual nucleons*, in the Danish journal *Matematisk-fysiske Meddelelser*, by Aage Bohr in 1952. The collective model was subsequently developed in collaboration with Ben R. Mottelson and James Rainwater, for which the three authors were awarded the Nobel Prize in 1975. The collective model should be regarded, as Bohr was warning, as a complementary approach to the shell model and should be used to shed light only on certain aspects of nuclear structure. In this picture, the nucleus consists of a core treated as a liquid drop and extra-core particles that contribute cooperatively to the nuclear properties. An extension of this model is the Nillson model, or distorted-shell model, in which the shell model potential is assumed non-spherical and the nucleons are not strongly coupled and move, approximately, independently. The slowly varying potential arises from nuclear deformation, which can occur as a result of the polarizing action of one or more loosely bound nucleons on the remaining nucleus. Bohr's paper was confined to the treatment of a single nucleon interacting with the nuclear surface. Overall, all these approaches introduce the concept of deformation in the atomic nucleus, absent in the original form of the shell model.

The deformation of the atomic nucleus has been one of the primary subjects of nuclear structure. The deformation varies as Z or N changes in such a way that it tends to be less pronounced near magic numbers, while it becomes more evident towards the middle of the shells. There are some properties of nuclei that can be reasonably identified not with the motion of a few valence nucleons, but instead with a motion that involves many of (if not all) the nucleons [4]. Such properties are called *collective properties*. In most cases (but not always), the collective properties vary smoothly and gradually with the mass number. The deformation in the shape of the nucleus leads to modes of excitation which are classified as *vibrational* and *rotational*.

Nuclear Vibrations

The Vibrational Collective Model for atomic nuclei is due to Lord Rayleigh, who showed in 1897 that small surface oscillations of an incompressible liquid drop around a spherical shape can be described with time-dependent coefficients $\alpha_{\lambda\mu}(t)$ defined as

$$R(\theta, \phi, t) = R_0 \left[1 + \sum_{\lambda=2}^{\infty} \sum_{\mu=-\lambda}^{\lambda} \alpha_{\lambda\mu}(t) Y_{\lambda\mu}(\theta, \phi) \right]. \tag{1.9}$$

In this equation, R_0 is the radius of the nucleus, (θ, ϕ) are the polar coordinates, $Y_{\lambda\mu}(\theta, \phi)$ are the spherical harmonics, λ is the multipolarity, and the subscript μ takes the values $-\lambda$ to λ. The $\lambda = 0$ term is incorporated into the average radius R_0. The $\lambda = 1$ term gives rise to the *dipole* vibration, which is a net displacement of the centre of mass and, therefore, cannot result from the action of internal nuclear forces. The next lowest modes are the $\lambda = 2$ (*quadrupole*) and $\lambda = 3$ (*octupole*) vibrations, shown in figure 1.2.

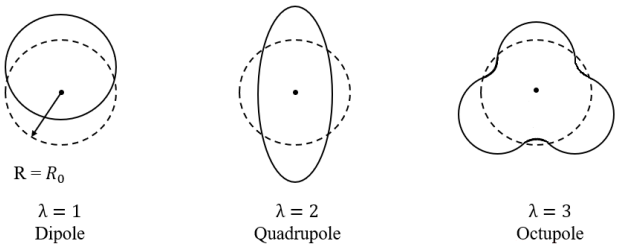

Figure 1.2: Dipole, quadrupole and octupole vibrational modes.

In analogy with the quantum theory of electromagnetism, a quantum of vibrational energy is called a *phonon*. For example, a quadrupole phonon ($\lambda = 2$) carries 2 units of angular momentum. Figure 1.3 shows an energy spectrum that could be treated in terms of a model based on vibrations about a spherical equilibrium shape. The single quadrupole phonon state (first 2^+), the two-phonon triplet, and the three-phonon quintuplet can be seen. The 3^- state presumably is due to the octupole vibration. Above 2 MeV, the structure becomes quite complicated, and no vibrational patterns can be identified.

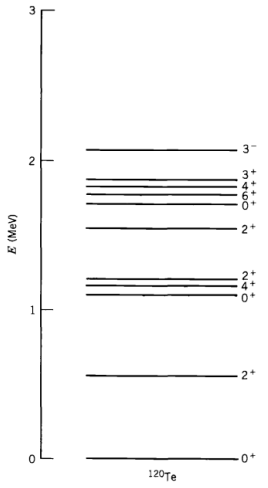

Figure 1.3: The low-lying levels of ^{120}Te. Adapted from Ref. [4].

Nuclear Rotations

The rotational motion can be observed only in nuclei with deformed equilibrium shapes, and can be described in axially-symmetrical nuclei with two sets of orthogonal systems of axes [5, 6]:

1. laboratory-fixed reference frame (x, y, z);
2. body-fixed reference frame (1, 2, 3), with direction 3 used as the symmetry axis.

Figure 1.4 defines some useful quantities for describing nuclear rotations. The vector **R** represents the angular momentum of rotation, which is perpendicular to the symmetry axis 3 due to the axial symmetry. The vector **j** is the angular momentum of the intrinsic nuclear state[2], and its projection Ω on the 3 axis coincides with the projection K of the total angular momentum **I = R + j**.

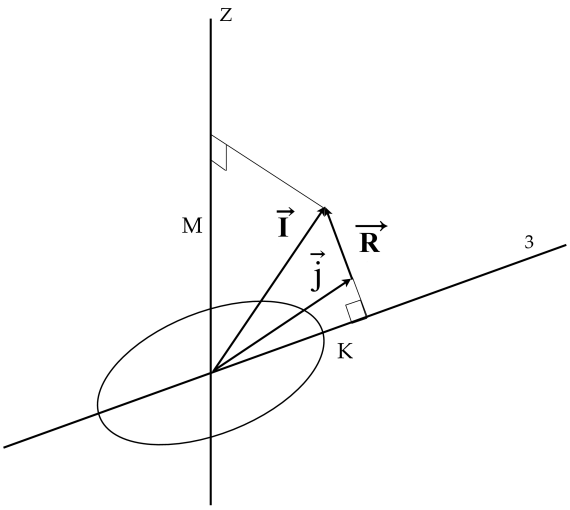

Figure 1.4: Schematic diagram for angular momenta in deformed nuclei.

Considering I_1, I_2 and I_3 as the components of **I** along the body-fixed axes and $\mathcal{I}_1$ = $\mathcal{I}_2$ = $\mathcal{I}$ as the moments of inertia for rotations around an axis perpendicular to axis 3, the rotational Hamiltonian is given by:

$$H = \frac{\hbar^2}{2\mathcal{I}}\,\mathbf{R}^2 = \frac{\hbar^2}{2\mathcal{I}}\,(\mathbf{I}-\mathbf{j})^2 = \frac{\hbar^2}{2\mathcal{I}}\,j^2 + \frac{\hbar^2}{2\mathcal{I}}\,(I^2 - 2I_3 j_3) + H_{coup} \tag{1.10}$$

where the term

$$H_{coup} = -\frac{\hbar^2}{2\mathcal{I}}\,2(I_1 j_1 + I_2 j_2) \tag{1.11}$$

[2]This description is valid for an even-even core and a loosely bound (unpaired) nucleon. In this picture, **j** is equivalent to the intrinsic angular momentum of the unpaired nucleon.

includes small terms related to the coupling of the intrinsic and rotational motion, which are generally negligible at slow rotations. The rotational wave functions are the D-functions, the transformation function for spherical harmonics under finite rotations. Denoting by M the component of the total angular momentum $\mathbf{I}$ along the z-axis (see figure 1.4), the relations satisfied by the angular momentum operator can be written as:

$$\mathbf{I}^2 \, D^I_{MK} = \big[I(I+1)\big] \, D^I_{MK} \tag{1.12}$$

$$I_z \, D^I_{MK} = M \, D^I_{MK} \tag{1.13}$$

$$I_3 \, D^I_{MK} = K \, D^I_{MK} \tag{1.14}$$

Hence, the energy eigenvalues of the Hamiltonian (1.10) have the form:

$$E_{IK} = \frac{\hbar^2}{2\mathcal{I}} \big[I(I+1) - K^2\big] + E_j(K) \tag{1.15}$$

where $E_j(K)$ is a constant that involves the projection K and quantities related to the intrinsic part of the system. For even-even nuclei (*i.e.*, with even numbers of protons and neutrons), which constitute the case of interest in this work, the intrinsic part does not contribute to the total angular momentum and, therefore, $K = 0$. Hence, the energy of the rotational band is given by:

$$E_I = \frac{\hbar^2}{2\mathcal{I}} \big[I(I+1)\big] \quad \text{with} \quad I = 0, 2, 4, \ldots . \tag{1.16}$$

Figure (1.5) shows the excited states of a typical rotational nucleus. Notice that the concept of a shape has meaning for a rotating nucleus. This motion is far slower than the internal motion of the nucleons [4]. Therefore, the correct picture of a rotating deformed nucleus is a stable equilibrium shape determined by nucleons in rapid internal motion in the nuclear potential. The rotational model is sometimes described as *adiabatic* for this reason.

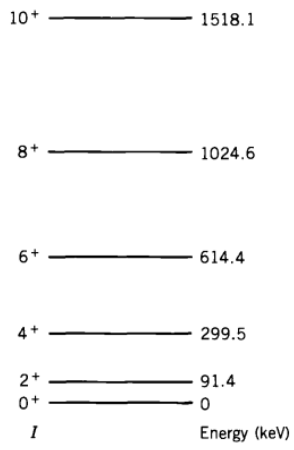

Figure 1.5: Excited states resulting from rotation of the ground state in ^{164}Er. Adapted from Ref. [4].

1.2 Nuclear Shape

Equation (1.9) can be used to describe static shapes by removing the dependence on time:

$$R(\theta,\phi) = R_0\left[1 + \sum_{\lambda\,\mu} \alpha_{\lambda\mu}\; Y_{\lambda\mu}(\theta,\phi)\right]. \tag{1.17}$$

The complex coefficients $\alpha_{\lambda\mu}$ become the deformation parameters and are equal to zero when the nucleus is a sphere. The index λ (multipolarity) indicates the type of deformation. For a fixed multipolarity λ, there are $2\lambda + 1$ modes of deformation ($\mu = -\lambda, ..., \lambda$). The requirement of reality for the nuclear radius implies that

$$\alpha_{\lambda\mu} = (-1)^{\mu}\; \alpha^{*}_{\lambda-\mu} \quad .$$

Equation (1.17) constitutes the starting point for the study of nuclear surface deformations. The lowest mode of surface deformation corresponds to the quadrupole mode $\lambda = 2$ since a deformation of order $\lambda = 1$ is equivalent to a translation of the system. Considering quadrupole deformations $\lambda = 2$ (the most frequent in even-even nuclei at low energy), the expansion parameters $\alpha_{2\mu}$ are $\mu = -2, -1, 0, 1, 2$. These five coefficients can be mapped to a set of other five variables $(\beta, \gamma, \theta_1, \theta_2, \theta_3)$, known as Hill-Wheeler coordinates. The Euler angles θ_i describe the relative orientation between the body-fixed reference frame (1, 2, 3) and the laboratory-fixed reference frame (x, y, z). The subset (β, γ) defines a two-dimensional polar coordinate system, where β is a measure of the

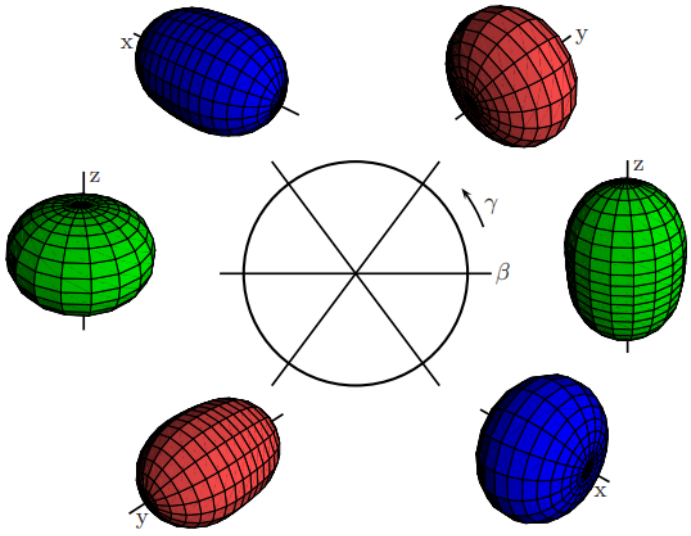

Figure 1.6: Quadrupole deformed shapes as a function of the Hill-Wheeler parameters (β, γ). Different colours identify the symmetry axis of the intrinsic reference frame. Adapted from Ref. [7].

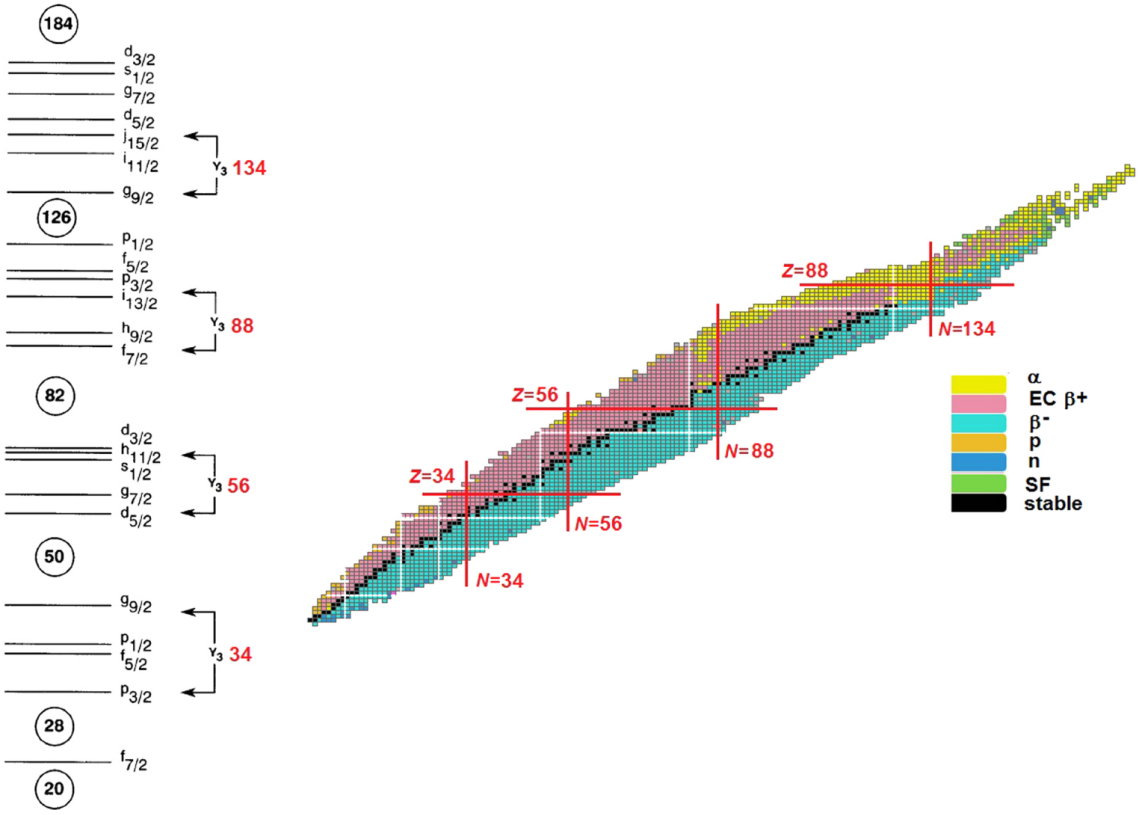

Figure 1.7: (Left) The nuclear spherical single-particle levels with the most important octupole correlations. (Right) Chart of the nuclides with the proton and neutron numbers having the strongest octupole correlations. The white lines indicate the positions of the magic numbers. Adapted from Ref. [8].

deviation from sphericity (the larger the value of β, the more deformed the surface) and γ determines the shape of the nucleus, as shown in figure 1.6. For instance, for $\beta \neq 0$, the nuclear shape is prolate if $\gamma = 0$ and oblate if $\gamma = 180°$. For most studies, the relevant information is in the shape itself and not in the symmetry axis. Therefore, it is usually sufficient to consider shapes with $0° < \gamma < 60°$.

Octupole deformation $\lambda = 3$ in nuclei is a rarer phenomenon in comparison to the quadrupole one. In this case, the main contribution comes from the spherical harmonic $Y_{3,0}$, and hence from the interaction between nucleons in two opposite parity single-particle states with $\Delta j = \Delta l = 3$. When protons and neutrons approaching the Fermi surface are found in these states and the spacing is small, octupole correlations are enhanced and octupole deformation is more favourable. The regions where this appears are located around the so-called *octupole magic numbers*, which are: 34, 56, 88, 134. Interestingly, these values are just greater than the shell-model magic numbers, where nuclei are nearly spherical. The octupole magic numbers are superimposed on the chart of the nuclides on the right-hand side of figure 1.7, indicating the nuclei having the strongest octupole coupling.

1.2.1 Shape Transition and Shape Coexistence

The transition from spherical to deformed shapes as a function of the neutron and proton numbers is known as *shape transition*. In this regard, the structures of neutron-rich nuclei of mass around 100 provide some of the best examples of the interplay between microscopic and macroscopic effects in shape transition. In this mass region of the nuclide chart, one of the first experimental evidence of shape transition was the observation of rotational-like behaviour in even-even fission fragments (Zr, Mo, Ru, Pd isotopes) from the spontaneous fission of ^{252}Cf [9]. Further supporting demonstrations of shape transition were obtained following the measurement of excitation energies of the first 2^+ states and two neutron separation energies S_{2n}, summarized in figure 1.8. A very sharp drop of the 2^+ energies is observed from $N = 58$ to $N = 60$ for the Sr and Zr isotopes, whereas the transitions are more gradual for Mo and Ru. This behaviour can be explained by a sudden change from a mostly spherical to a well-deformed quadrupole shape at $N = 60$.

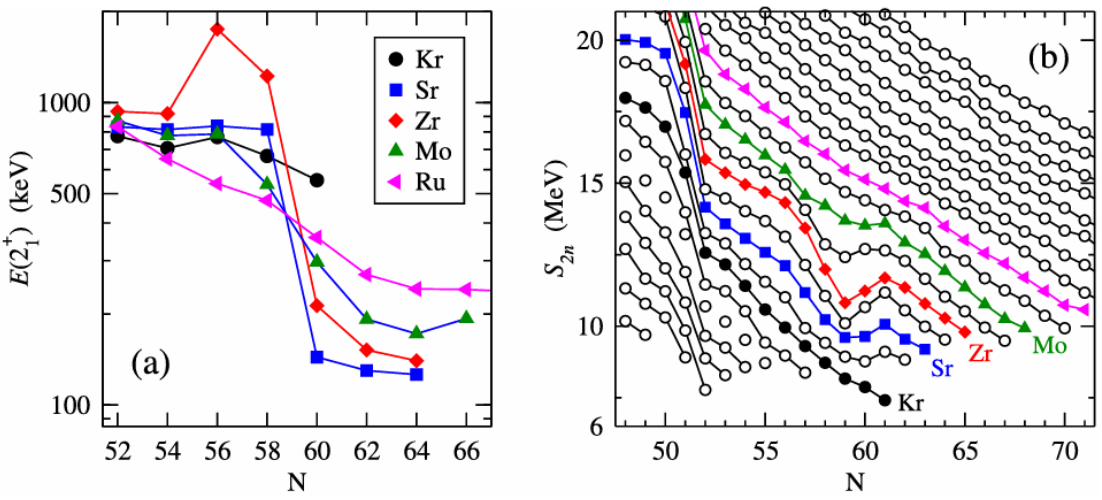

Figure 1.8: (a) Excitation energies of the first 2^+ states and (b) two-neutron separation energies for nuclei around $N = 60$. Adapted from Ref. [10].

Shape coexistence [11] is a very peculiar phenomenon consisting of the presence within the same nucleus, at low-excitation energy, and within a very narrow energy range, of two or more states having well-distinct properties that can be interpreted in terms of different intrinsic shapes. The observation of a specific nuclide exhibiting eigenstates with different shapes is a unique type of behaviour of the nucleus in finite many-body quantum systems. Such behaviour is familiar in molecules but, in this case, the different shapes involve different geometrical arrangements of widely spaced atoms (constrained by identical chemical bonds), at variance with atomic nuclei.

Understanding the occurrence of shape coexistence in atomic nuclei is one of the greatest challenges faced by theories of nuclear structure. The first discovery of the phe-

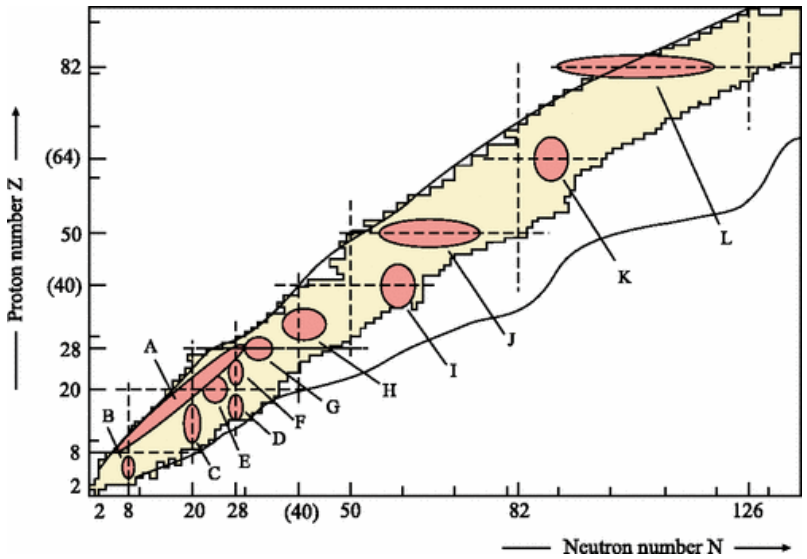

Figure 1.9: Regions of the nuclide chart where shape coexistence has been observed. Adapted from Ref. [11].

nomenon was published in a paper by H. Morinaga in 1956 [12]. The level structures of light nuclei, in particular ^{16}O, show some characteristic features that are not easy to explain from simple shell-model theories. Among these, the presence of a 0^+ excited state at 6.06 MeV. This 0^+ state can be seen as a rotation-less state of a strongly deformed configuration. Since the ^{16}O ground state is a closed-core configuration, it should be spherical. However, eight valence nucleons are excited in the 6.06-MeV state, causing the deformation of the nucleus.

In 1964, G. Brown extended Morinaga's idea to a similar state in ^{40}Ca. This work led to other investigations of nuclear structure, with the collection of extensive data supporting the widespread and unequivocal manifestation of shape coexistence in the mass region characterized by $(Z, N) \sim (82, 104)$ (figure 1.9). The first indication of shape coexistence in this region came from optical hyperfine structure studies[3] of the Hg isotopes ($Z = 80$) [13]. The emerging picture in these isotopes raised the question of the survival of the spherical-shaped closed shell ($Z = 82$). This led to intensive study of the Pb isotopes. A landmark paper, Ref. [14], reported the observation of multiple low-lying excited 0^+ states in ^{186}Pb using decay spectroscopy of ^{190}Po. This study provided the experimental evidence that the lowest three states in the nucleus ^{186}Pb are spherical, oblate and prolate (figure 1.10).

[3]The hyperfine splitting of the atomic electron levels gives direct access to some nuclear properties, such as spin, magnetic dipole and electric quadrupole moments. Such measurements are therefore a direct probe of changes in nuclear size or deformation as a result of the addition or removal of nucleons.

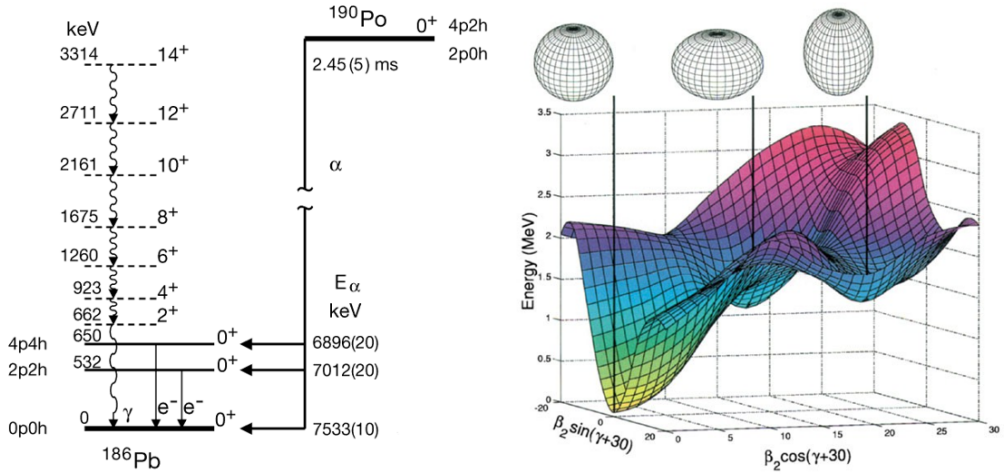

Figure 1.10: (Left) Decay pattern of ^{190}Po and level scheme of ^{186}Pb. (Right) Calculated potential energy surface of ^{186}Pb. Spherical, oblate and prolate minima are indicated by thick vertical black lines. Adapted from Ref. [14].

1.3 Quadrupole and Octupole Collectivity in Zirconium Isotopes

The Zirconium isotopes have been the subject of intensive experimental and theoretical work to gather insight into a variety of different nuclear structure phenomena. They span a wide range of masses from a mid-open-shell region (^{80}Zr$_{40}$), which is thought to be deformed, through a closed neutron shell (^{90}Zr$_{50}$), to a closed neutron subshell[4] (^{96}Zr$_{56}$), and then to a sudden reappearance of deformation (^{100}Zr$_{60}$) [15], which has been shown to persist as far as to another mid-open-shell region [16] (^{110}Zr$_{70}$). This variety of behaviour is unique on the nuclear mass surface.

Recent state-of-the-art shell-model calculations by T. Togashi *et al.* [17] have yielded a wealth of information on the collective properties and shapes of even-even zirconium isotopes at low spin. The experimental energies and those calculated with this model for the $0^+_{1,2}$ and $2^+_{1,2}$ states are reported in figure 1.11, together with their calculated shapes. The ground state of the even zirconium isotopes is predicted to be spherical until neutron number $N = 58$, while it becomes prolate from $N = 60$. The first excited state with $J^\pi = 2^+$ has the same shape as the ground state, except for $N = 50, 58$. Interestingly, the 0^+_2 and 2^+_2 states are predicted to exhibit a variety of shapes including prolate, oblate and even non-axially symmetric (commonly called *triaxial*) shapes as the neutron number evolves.

[4] A *Subshell Closure* is found at a certain proton or neutron number that experimentally has locally enhanced stability, similar to the shell closures in the shell model. Known subshell closures of interest for this work are, for instance, $N = 56$ and $Z, N = 40$.

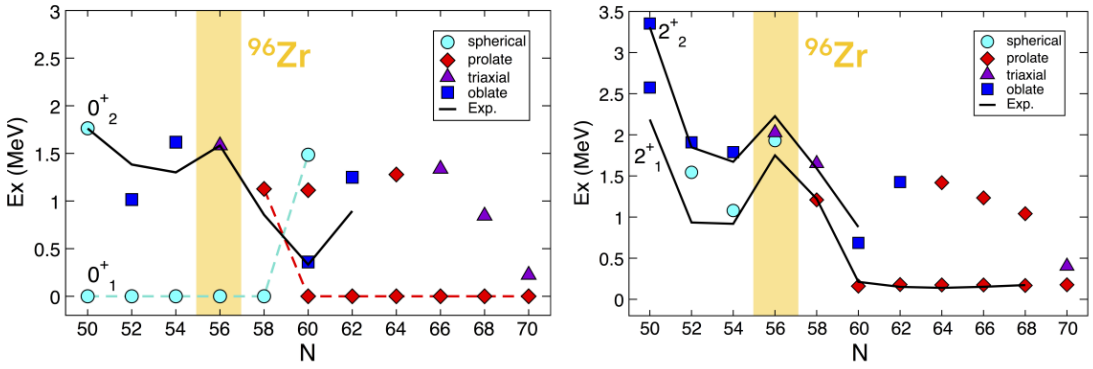

Figure 1.11: Energy of the $0^+_{1,2}$ (left) and $2^+_{1,2}$ (right) states as a function of the neutron number for the zirconium isotopic chain. The different symbols indicate the predicted shapes associated with the states as shown in the legend. The solid lines indicate the experimental data, while the dashed lines are drawn to guide the eye. Adapted from Ref. [17].

In this context, ^{96}Zr$_{56}$ occupies an intriguing position in the zirconium isotopic chain. This isotope is positioned on subshell closures for both protons ($Z = 40$) and neutrons ($N = 56$), which result in locally high-excitation energy for its low-lying states (figure 1.11). Also, the spherical ground state is predicted to coexist with a triaxial structure built on the 0^+_2 state [17] (figure 1.11). This feature is particularly intriguing given the rarity of triaxial shapes in the nuclide chart.

The structure of ^{96}Zr is also particularly interesting regarding octupole deformation. A striking experimental signature of octupole collectivity, either vibrational or rotational, is an enhanced transition probability from the first excited 3^- state to the ground state ($3^-_1 \rightarrow 0^+_1$ transition). In this context, the 3^-_1 state in ^{96}Zr is interesting because this quantity has been the subject of intense debate in the literature. Figure 1.12 shows the experimental energy of the 3^-_1 level (panel a) and the experimental $3^-_1 \rightarrow 0^+_1$ γ–ray transition probability (panel b) as a function of the neutron number for the Zr isotopes and the neighbouring even-even Mo isotopes ($Z = 42$). In ^{90}Zr ($N = 50$), the 3^-_1 level has a relatively high excitation energy, which decreases with the neutron number. On the contrary, the γ–ray transition probability increases going from ^{90}Zr to heavier isotopes. A similar trend is observed in the Mo isotopes but for ^{96}Zr an unusually large value for this quantity has been measured compared to the close ^{92,94}Zr isotopes. Indeed, the γ–ray transition probability found in ^{96}Zr for the $3^-_1 \rightarrow 0^+_1$ transition is one of the largest across the nuclear chart [18] and the strongest in a supposed spherical nucleus. Noteworthy, this experimental value has never been reproduced by any theoretical calculations. A revision of the $3^-_1 \rightarrow 0^+_1$ branch in the decay of the 3^-_1 state in ^{96}Zr has been recently given in Ref. [19], based on a reevaluation of different high-statistics datasets acquired with the Gammasphere γ–ray spectrometer [20]. The obtained results, when combined with the

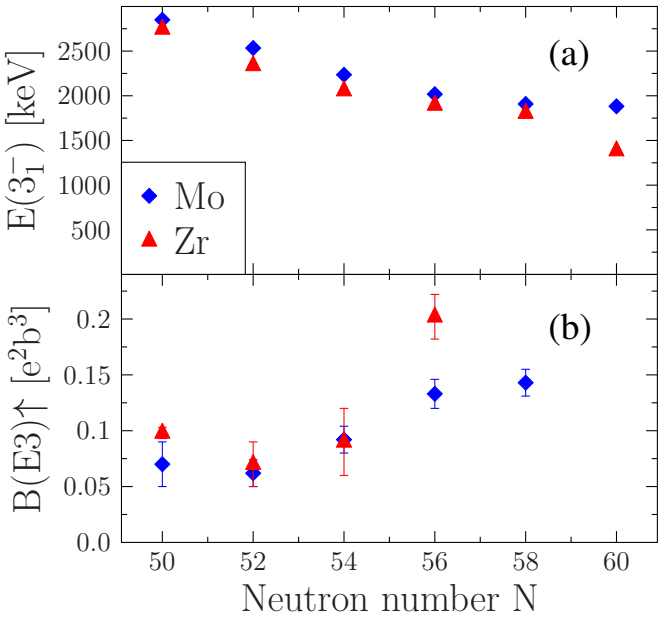

Figure 1.12: Energies of the 3_1^- state (panel a) and γ–ray transition probability for the $3_1^- \rightarrow 0_1^+$ transition (panel b) reported as a function of the neutron number for the zirconium (red, triangular dots) and molybdenum (blue, diamond dots) isotopes. Adapted from Ref. [18].

lifetime of the 3_1^- state from Ref. [21], yielded a γ–ray transition probability in better agreement with the experimental trend.

The present work is dedicated to extracting for the first time the $3_1^- \rightarrow 0_1^+$ γ–ray transition probability via the low-energy Coulomb excitation technique. This technique will allow for obtaining this value directly for the first time instead of extracting it from measurements of branching ratios and lifetimes, as done in previous studies.

Chapter 2

Coulomb-Excitation Technique

Coulomb excitation is an inelastic scattering process in which two colliding nuclei are excited via a mutually-generated, time-dependent electromagnetic field. The purely electromagnetic interaction causes the nucleus to undergo a transition from an initial state to a final state, the latter decaying after a certain amount of time. The Coulomb-excitation experimental technique consists of the exploitation of the Coulomb-excitation process to extract information about the colliding nuclei by measuring γ–ray yields following the decay from the excited states. This technique is one of the best tools for investigating nuclear properties because the electromagnetic interaction is well-known.

In this chapter, after recalling some basic features of the γ decay, the theoretical description of Coulomb excitation will be introduced. After that, the experimental considerations taken into account in Coulomb-excitation experiments will be discussed and the GOSIA code, the standard tool for Coulomb-excitation data analysis, will be introduced.

2.1 Gamma Decay

At the first order, an excited nucleus can decay to a lower-energy state by emission of electromagnetic radiation, *i.e.* a γ–ray, or by internal conversion, *i.e.* an atomic electron. Electromagnetic radiation can be treated either as a classical wave phenomenon or as a quantum phenomenon. The quantum description is most appropriate to describe radiations from nuclei but it is easier to start with the classical theory.

Static distributions of charges and currents give static electric and magnetic fields, which can be analyzed in terms of multipole moments. The simplest distributions of charges and currents deal only with the lowest-order multipole fields. Indeed, a spherical charge distribution produces an electric monopole field, and a circular current loop produces a magnetic dipole field. It is usually enough to measure or calculate only the lowest-order multipole moments to characterize the electromagnetic properties of the nucleus. Another restriction on the multipole moments is directly related to the parity of the

nuclear states. Each electromagnetic multipole moment has a parity, determined by the behavior of the multipole operator when $\mathbf{r} \rightarrow -\mathbf{r}$. The parity of the electric and magnetic moments are:

$$\pi(EL) = (-1)^L \quad \text{and} \quad \pi(ML) = (-1)^{L+1} \tag{2.1}$$

where L is the order of the moment ($L = 0$ for monopole, $L = 1$ for dipole, $L = 2$ for quadrupole, $L = 3$ for octupole, ...). From (2.1) it is visible how electric and magnetic multipoles of the same order have opposite parity. If the charge and current distributions vary with time, a radiation field is produced. This field can be easily studied far from the source (far compared with the size of the source itself) in terms of its multipole character. The average radiated power energy emitted per unit time, using $\sigma = E, M$ to represent electric or magnetic radiation, is:

$$P(\sigma L) = \frac{2(L+1)c}{\epsilon_0 L[(2L+1)!!]^2}\left(\frac{\omega}{c}\right)^{2L+2}[m(\sigma L)]^2 \tag{2.2}$$

where ω is the angular frequency of the electromagnetic field and $m(\sigma L)$ is the amplitude of the time-varying electric or magnetic multipole moment. To switch to the quantum domain, it is necessary to replace the multipole moments $m(\sigma L)$ with appropriate multipole operators that change the nucleus from its initial state ψ_i to the final state ψ_f. The decay probability is governed by the matrix element of the multipole operator:

$$m_{fi}(\sigma L) = \int dV\, \psi_f^*\; m(\sigma L)\; \psi_i \tag{2.3}$$

where the integral is carried out over the volume of the nucleus (the detailed form of the multipole operator can be found in Ref. [22]). If equation (2.2) is seen as the energy radiated per unit time in the form of photons, each of which has energy $\hbar\omega$, the probability per unit time for photon emission (decay constant) is:

$$\lambda(\sigma L) = \frac{P(\sigma L)}{\hbar\omega} = \frac{2(L+1)}{\epsilon_0 \hbar L[(2L+1)!!]^2}\left(\frac{\omega}{c}\right)^{2L+1}[m_{fi}(\sigma L)]^2\,. \tag{2.4}$$

The probability of photon emission is related to the lifetime of the initial state. Specifically, the lifetime is the inverse of the sum of the partial decay rates considering all the possible final states and the different multipolarities that are involved.

The evaluation of the matrix element requires knowledge of the initial and final wave functions. However, it is possible to make some estimates of the γ–ray emission probabilities with the following assumptions:

- the transition is due to a single proton that changes from one shell-model state to another;

L	$\lambda(EL)$	$\lambda(ML)$
1	$1.0 \cdot 10^{14}\ A^{2/3}E^3$	$5.6 \cdot 10^{13}\ E^3$
2	$7.3 \cdot 10^{7}\ A^{4/3}E^5$	$3.5 \cdot 10^{7}\ A^{2/3}E^5$
3	$34\ A^2E^7$	$16\ A^{4/3}E^7$
4	$1.1 \cdot 10^{-5}\ A^{8/3}E^9$	$4.5 \cdot 10^{-6}\ A^2E^9$

Table 2.1: Weisskopf estimates of transition probabilities for some of the low multipole orders, taken from Ref. [4]. A is the mass number and E is the photon energy in MeV.

- the radial parts of the nuclear wave functions ψ_i and ψ_f are constant up to the nuclear radius R and zero for $r > R$.

With these approximations, and using $R = 1.2\ A^{1/3}$ fm for the nuclear radius, the EL and ML transition probabilities for the lower multipole orders assume the values reported in table 2.1. These estimates for the transition rates are known as *Weisskopf estimates* and are meant to provide reasonable values to compare with measured transition rates. For example, if the observed decay rate of a certain γ transition is much greater than the Weisskopf estimate, more than one single nucleon is probably responsible for the transition. The Weisskopf estimates show some general properties of transition probabilities:

- the lower multipolarities are dominant;
- for a given multipole order, electric radiation is more likely than magnetic radiation.

The conservation of angular momentum and parity prohibit certain γ transitions, following the selection rules of the γ decay. A quantum of radiation carries an angular momentum $\mathbf{L}$ of module $\hbar\sqrt{L(L+1)}$ (L corresponds to the multipole order). In a transition between an initial excited state of angular momentum $\mathbf{J}_i$ and a final state $\mathbf{J}_f$ the conservation of angular momentum imposes

$$\mathbf{J}_i = \mathbf{J}_f + \mathbf{L}\,. \tag{2.5}$$

Hence, the possible values for the multipoles are:

$$|J_i - J_f| \leq L \leq J_i + J_f\,. \tag{2.6}$$

It must be pointed out that γ transitions with $L = 0$ are forbidden because the photon has an intrinsic spin of 1, while internal conversion with $L = 0$ is allowed. The conservation of the parity π requires:

$$EL:\ \pi_i \cdot \pi_f = (-1)^L \quad \text{and} \quad ML:\ \pi_i \cdot \pi_f = (-1)^{L+1}\,. \tag{2.7}$$

This means that states with the same parity can be only connected by electric multipoles with even L or by magnetic multipoles with odd L, while states with opposite parity

ΔL	Multipole	$\pi_i \cdot \pi_f = +1$	$\pi_i \cdot \pi_f = -1$
0	Monopole	Forbidden	Forbidden
1	Dipole	$M1$	$E1$
2	Quadrupole	$E2$	$M2$
3	Octupole	$M3$	$E3$

Table 2.2: γ electromagnetic transitions for $\Delta L \leq 3$ allowed by the selection rules.

can only be connected by electric multipoles with odd L or by magnetic multipoles with even L. If the selection rules allow more than one multipolarity σL for a transition, the *mixing ratio* δ is defined as the ratio between the decay rates associated with the different multipolarities.

The γ transition rate between an initial and a final state in equation (2.4) can also be expressed as:

$$\lambda(\sigma L, J_i \rightarrow J_f) = \frac{8\pi(L+1)}{\hbar L[(2L+1)!!]^2}\left(\frac{E_\gamma}{\hbar c}\right)^{2L+1} B(\sigma L; J_i \rightarrow J_f)\,. \tag{2.8}$$

The last term in equation (2.8), $B(\sigma L; J_i \rightarrow J_f)$, is called *reduced transition probability* and is defined as follow:

$$B(\sigma L; J_i \rightarrow J_f) = \frac{1}{2J_i+1}|\,\langle J_f||M(\sigma L)||J_i\rangle\,|^2 \tag{2.9}$$

where $\langle J_f||M(\sigma L)||J_i\rangle$ is the reduced form of the electromagnetic matrix element (2.3). The units of reduced transition probabilities for electric transitions are $e^2\text{fm}^{2L}$, while the magnetic ones are $\mu_N^2\text{fm}^{2(L-1)}$ where μ_N is the nuclear magneton. Using the definitions of the Weisskopf estimates, it is possible to define other common units for reduced transition probabilities, the so-called *Weisskopf units* (or *single-particle units*), given by:

$$EL:\ 1\,W.u. = \frac{1}{4\pi}\left(\frac{3}{L+3}\right)^2 (1.2A^{1/3})^{2L}\,e^2 fm^{2L}\,, \tag{2.10}$$

$$ML:\ 1\,W.u. = \frac{10}{\pi}\left(\frac{3}{L+3}\right)^2 (1.2A^{1/3})^{2L-2}\,\mu_\mu^2 fm^{2(L-1)}\,. \tag{2.11}$$

The experimental values of the nuclear transition probabilities may show strong deviations from the Weisskopf estimates. For instance, electric quadrupole $E2$ and octupole $E3$ transitions are often found to be strongly enhanced with respect to the single particle estimate. In this latter case, the transition is induced by the coherent contribution of several particles, meaning that nuclear collectivity manifests. Reduced transition probabilities are some of the most sensitive probes to characterize how well nuclear models reproduce nuclear-structure properties.

2.2 Coulomb-Excitation Process

The possibility of exciting atomic nuclei using the electromagnetic field was realized already in the 1930s [23]. It was not before 1952, however, that the process was experimentally used and became known as *Coulomb excitation*. In the early Coulomb-excitation experiments, light ions were used as projectiles. Therefore, only a few nuclear states could be populated by the weak electromagnetic forces involved. The construction of accelerators for heavy ions opened up the possibility of performing much more complex experiments. In collisions involving heavy nuclei, the large values of mass, size and electric charge contribute to new dynamical aspects, which are typically absent in collisions with light projectiles.

The reactions involving heavy ions at low energy ($\approx 5-10$ MeV/A) are characterized by a wavelength of the relative motion small compared to the interaction radius R, which is defined as the sum of the radii of the two interacting nuclei ($R = R_P + R_T$). Hence, it is possible to use the semi-classical treatment rather than the quantum-mechanical one to describe the process [24]. In the semi-classical treatment, it is useful to define the impact parameter b, which is the distance between the direction of the initial velocity of the projectile and the parallel straight line passing through the centre of the target (see figure 2.1).

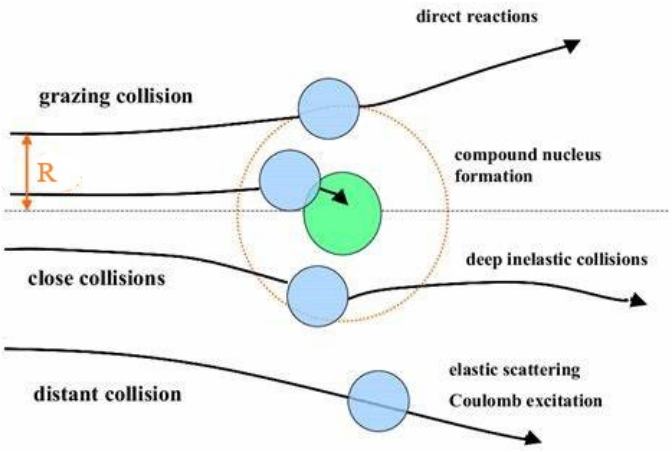

Figure 2.1: Classification of heavy ion collisions based on the impact parameter b.

In this work, we will use the so-called *low-energy* Coulomb-excitation process, *i.e.* the process where the projectile energy is well below the Coulomb barrier so that no penetration into the region of nuclear forces occurs. Hence, the excitation is caused solely by electromagnetic forces. In the case of heavy nuclei ($A > 30-40$), this requirement can be quantified using the so-called *Cline's safe distance criterion* [25], which states that if the distance of the closest approach between the surfaces of the collision partners exceeds 5 fm, the contribution from the nuclear interaction to the excitation cross-sections is below 0.5%. The Cline's criterion is usually satisfied for a beam energy of $\approx 3-5$ MeV/A.

In low-energy Coulomb excitation, the De Broglie wavelength λ associated with the system projectile is small compared to the distance of closest approach a in a head-on

collision:

$$\lambda = \frac{h}{p} = \frac{h}{\sqrt{2mE}} \ll a = \frac{Z_P Z_P e^2}{E} = \frac{2Z_P Z_P e^2}{mv^2} = 2a_0 \tag{2.12}$$

where m is the reduced mass of the system, v is the relative velocity of the two nuclei at infinity, which determines the energy of relative motion $E = mv^2/2$, and Z_P and Z_T are the charge numbers of the projectile and target nuclei, respectively. The requirement in (2.12) can be expressed using the Sommerfeld parameter η as follows:

$$\eta = \frac{Z_P Z_P e^2}{\hbar\nu} = \frac{2\pi a}{\lambda} \gg 1\,. \tag{2.13}$$

This inequality represents the condition for the applicability of a *semi-classical approach* for the description of the Coulomb-excitation process. Specifically, if condition (2.13) is fulfilled, the scattering may be described accurately in terms of wave packets that follow classical hyperbolic orbits. The condition (2.13) is typically satisfied in low-energy Coulomb-excitation experiments involving heavy ions [22]. In these cases, the excitation is caused by the time-dependent electromagnetic field acting between the target and the projectile as the latter moves along the hyperbolic orbit according to the classical equations of motion. However, for the applicability of the semi-classical treatment, another condition is required. The excitation energy ΔE must not modify the orbit significantly, therefore:

$$\Delta E \ll E \rightarrow \Delta E/E \ll 1\,. \tag{2.14}$$

2.2.1 Semi-Classical Treatment

In the semi-classical approximation the projectile trajectories are described by the Rutherford scattering and quantum mechanics is used to describe the effect of the electromagnetic field on the nucleus.

The Hamiltonian of the collision process is given by:

$$H = H_0(P) + H_0(T) + W\big(P, T, \mathbf{r}(t)\big)\,, \tag{2.15}$$

where $H_0(P)$ and $H_0(T)$ are the Hamiltonians of the free projectile and target nuclei, while $W(P, T, \mathbf{r}(t))$ is the mutual electromagnetic interaction, which is a function of time through the relative position vector $\mathbf{r}(t)$. The interaction term W can be expanded in electric and magnetic multipole moments of the two nuclei in their respective rest systems and, hence, decomposed in three parts:

$$W\big(P, T, \mathbf{r}(t)\big) = W_E\big(P, T, \mathbf{r}(t)\big) + W_M\big(P, T, \mathbf{r}(t)\big) + W_{EM}\big(P, T, \mathbf{r}(t)\big)\,. \tag{2.16}$$

In this expression, W_E is the mutual electric multipole-multipole interaction, W_M is the

mutual magnetic multipole-multipole interaction and W_{EM} is the interaction between the electric and the magnetic multipole moments. The main term in W_E is the electric monopole-monopole interaction, corresponding to the Coulomb energy $Z_P Z_P e^2/r$, which determines the relative motion of the two nuclear centres[1]. Next in importance in W_E are the interaction terms between the monopole moment of the projectile (target) and the multipole moments of the target (projectile), which give rise to the target (projectile) excitation. Higher-order multipole-multipole excitations in W_E (dipole-multipole, quadrupole-multipole, ...) can usually be neglected. Concerning the magnetic multipole moments, the monopole-multipole terms of W_{EM} are usually the largest, giving rise to weak magnetic excitations. For this reason, they are treated as perturbations. The equation (2.16), thus, can be approximated as:

$$W\big(P,T,\mathbf{r}(t)\big) \sim \frac{Z_P Z_P e^2}{r} + V_E\big(P,\mathbf{r}(t)\big) + V_E\big(T,\mathbf{r}(t)\big)\,. \tag{2.17}$$

In low-energy Coulomb excitation, the magnitude of the monopole-monopole interaction $Z_P Z_P e^2/r$ is responsible for the great simplification in the theory since it ensures the condition (2.13). In principle, during the collision, one or both nuclei can be excited but in the following, for simplicity, only the target nucleus is considered excited. With P_n the probability of finding the nucleus, after the collision, in the state identified by the quantum number n, the differential scattering cross-section for the excitation to this state is given by:

$$\frac{d\sigma_{Coulex}}{d\Omega} = \frac{d\sigma_R}{d\Omega} \cdot P_n. \tag{2.18}$$

Here $d\sigma_R/d\Omega$ is the Rutherford scattering cross-section.

The excitation probabilities can be found by solving the time-dependent Schrödinger equation:

$$i\hbar\frac{\partial}{\partial t}\,|\psi(t)\rangle = \big[H_0(T) + V_E\big(T,\mathbf{r}(t)\big)\big]\,|\psi(t)\rangle \tag{2.19}$$

where $|\psi(t)\rangle$ is the target-state vector, while the interaction potential can be written as a function of the electric multipole moments M_T as follows

$$V_E\big(T,\mathbf{r}(t)\big) = \sum_{\lambda\geq 1,\mu} \frac{4\pi e\, Z_P}{2\lambda+1}\, M_T(E\lambda,-\mu)\,(-1)^{\mu}\,[\mathbf{r}(t)]^{-\lambda-1}\,Y_{\lambda\mu}(\theta,\phi)\,. \tag{2.20}$$

The wave function $|\psi(t)\rangle$ can be expanded in terms of the eigenstates of the free Hamiltonian H_0 as

$$|\psi(t)\rangle = \sum_n a_n(t)\,|\varphi_n\rangle \tag{2.21}$$

[1]This interaction does not give rise to any excitation because it does not depend on the intrinsic degrees of freedom of the two nuclei.

with

$$H_0 \left|n\right\rangle = E_n \left|\varphi_n\right\rangle \ . \tag{2.22}$$

The coefficients $a_n(t)$ are the time-dependent excitation amplitudes

$$a_n = \langle\varphi_n|\psi(t)\rangle = \langle\varphi_n|\psi\rangle \ \ e^{\frac{iE_nt}{\hbar}} \tag{2.23}$$

and they become time independent for $t = +\infty$, where the interaction V_E vanishes. From these definitions, equation (2.19) is equivalent to the set of linear differential equations

$$i\hbar\frac{da_n}{dt} = \sum_m \langle n|V_E(t)|m\rangle \ \ e^{\frac{i(E_n-E_m)t}{\hbar}} \ \ a_m(t)\,. \tag{2.24}$$

The initial condition of these equations is that at $t = -\infty$ (*i.e.* $V_E = 0$), the nucleus is in its ground state $|\varphi_0\rangle$:

$$|\psi(-\infty)\rangle = |\varphi_0\rangle \ . \tag{2.25}$$

The values a_n are then the excitation amplitudes after the collision[2], and the excitation probabilities are given by:

$$P_{0\to n} = |a_n|^2\,. \tag{2.26}$$

2.2.2 First-Order Perturbation Theory

If the interaction between the projectile and the target nuclei is weak[3], the system of coupled equations (2.24) can be solved using the first-order perturbation theory. This treatment leads to the following expression for the excitation amplitude from the ground state of a given nuclear state:

$$a_n = \frac{1}{i\hbar}\int_{-\infty}^{+\infty} \langle\varphi_n|V_E(t)|\varphi_0\rangle \ \ e^{\frac{i\Delta Et}{\hbar}}dt\,. \tag{2.27}$$

By expanding V_E into multipole components, the amplitude is factorized in a part that depends on the nucleus only through the matrix element of the multipole moments, and an integral that only depends on the excitation energy ΔE and the kinematics of the classical orbit.

The coefficients (2.27) can be used to compute the cross-section of the process. The

[2]Since the effective collision time in Coulomb excitation is of the order of 1 zs, which is 10^8 times shorter than the typical lifetimes of the excited states ($\sim 1 - 10$ ps), it is possible to consider $|\psi(+\infty)\rangle$ as the wave function after the collision.

[3]This condition can be quantified requiring that the excitation probability connecting the involved excited states must be small compared to unity.

differential cross-section for electric excitations is written in the form

$$d\sigma = \sum_{\lambda} d\sigma_{E\lambda} \,, \tag{2.28}$$

where

$$d\sigma_{E\lambda} = \left(\frac{Z_P \, e}{\hbar \, v_P} \right)^2 a^{-2\lambda+2} \; B(E\lambda; I_0 \to I_f) \; df_{E\lambda}(\theta, \xi) \,. \tag{2.29}$$

In this expression $B(E\lambda, I_0 \to I_f)$ is the reduced transition probability defined in (2.9), while $df_{E\lambda}$ is the differential cross-section function, which depends on θ_{CM} and on the so-called *adiabaticity parameter*, which can be expressed as the difference between the final and initial Sommerfeld parameter:

$$\xi = \eta_f - \eta_i = \frac{a \, \Delta E}{\hbar \, v_P} \,. \tag{2.30}$$

The functions df are tabulated and show that an increase of one unity in the multipolarity λ roughly corresponds to an order of magnitude decrease in the value of df. Magnetic excitations can be obtained by replacing $E \to M$ and $v_P \to c$ in (2.29).

2.2.3 Second-Order Perturbation Theory

The second-order perturbation theory provides a method to describe the multi-step excitation, which refers to the population of an excited state starting from the ground state and passing through one or more intermediate states.

Multi-step excitations are processes that occur in the second order when compared to single-step excitations. However, in certain cases, double-step excitations can compete and even become the most important contribution to Coulomb excitation. To understand this point, it is useful to consider the population of a 4_1^+ state in an even-even nucleus. Such a state can be populated from the 0_1^+ ground state in two ways, as shown in figure 2.2. Direct excitation requires a transition of $E4$ multipolarity, whereas two-step excitation, passing through the intermediate 2_1^+ state, requires two successive transitions of $E2$ multipolarity. Considering that the transition probability $E4$ is typically much smaller than $E2$, the dominant process in this case is the two-step excitation. Another interesting case is that of a second, higher-energy 2^+ state. Such a state can be populated both by a direct $E2$ transition from the ground state, as well as by a two-step excitation through the 2_1^+ state (see figure 2.2). In this case, single-step and double-step excitations may be competitive.

Multi-step excitation is more probable for larger values of the scattering angle because in this case the nucleus experiences (on average) a stronger electromagnetic field during the scattering process.

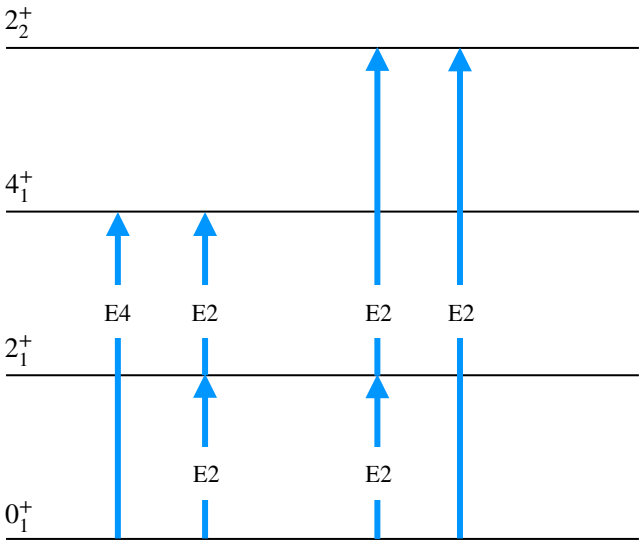

Figure 2.2: Schematic illustration of the multipolarities necessary to populate the 4_1^+ and 2_2^+ excited states in an even-even nucleus.

2.3 Experimental Considerations

In the present work, γ rays from the de-excitation of the Coulomb-excited states were detected in coincidence with the scattered projectile nuclei. By using a segmented particle detector (SPIDER) it was possible to determine the scattering angle to perform a correction on the γ–ray spectra related to the Doppler effect.

The typical lifetimes of the excited states populated in Coulomb excitation are several orders of magnitude smaller than the typical flight time of the scattered ions from the target position to the particle detector. Therefore, the γ rays are typically emitted in flight, and their energy is affected by the Doppler shift, *i.e.* it is shifted to lower or higher energies, depending on the kinematics. This effect is described in the first order in β by the equation:

$$E_{det} = \frac{E_0}{\gamma(1 - \beta\cos(\vartheta))} \tag{2.31}$$

where E_{det} is the detected energy of the γ ray in the laboratory system affected by the Doppler shift, E_0 is the γ–ray energy in the reference system of the nucleus (not shifted), β is the velocity of the excited nucleus ($\beta = v/c$) and γ is the Lorentz factor. The angle ϑ is the angle between the direction of the emitted γ ray and the direction of the de-exciting

scattered nucleus, and can be expressed using spherical coordinates as

$$\cos(\vartheta) = \sin(\theta_p)\sin(\theta_\gamma)\cos(\phi_p - \phi_\gamma) + \cos(\theta_p)\cos(\theta_\gamma) \tag{2.32}$$

where the angles (θ_p, ϕ_p), $(\theta_\gamma, \phi_\gamma)$ define the directions of the emitted γ ray and the corresponding scattered nucleus, respectively, in the laboratory system. If the experimental setup allows to measure (θ_p, ϕ_p), $(\theta_\gamma, \phi_\gamma)$, it is possible to invert the equation (2.31) and get the energy E_0 from the measured energy E_{det}. The quantity β can be obtained by the value of the energy E_p of the scattered ions measured in the particle detector from $\beta = \sqrt{2E_p/m_pc^2}$. The accuracy of the Doppler correction is determined by the precision with which the various quantities are measured, *i.e.* by the degree of segmentation of both the γ–ray and particle detectors and the energy resolution of the latter.

In Coulomb-excitation experiments, the nuclear structure of both the target and the projectile can be studied. Measurements in which the target nucleus is investigated are typically more complicated, because the target material may contain impurities, as in the case of the present work. Sometimes, a projectile-target nuclei combination is chosen to satisfy the relation $A_P < A_T$. In this way, it is possible to diffuse the projectile nuclei at backward angles where, as already mentioned, the probability of multi-step excitation is greater. In addition, when using solid-state particle detectors, this configuration minimizes the damage of the crystal lattice of the detector (the so-called radiation damage) caused by the flux of particles since the Rutherford cross-section is lower for backward scattering.

2.4 GOSIA Code

To extract the observables of interest from the data collected in a Coulomb-excitation experiment, the excitation cross-section must be reconstructed. The complexity of this problem increases with the number of excited states. The GOSIA code [26] is the most advanced tool for data analysis of Coulomb-excitation experiments to date. It was developed in the 1980s, in a collaboration between the University of Warsaw (Poland) and the University of Rochester (US), to simulate and analyze experiments where single γ–rays and/or γ–particle coincidences are detected.

GOSIA exploits the semi-classical Coulomb-excitation treatment, discussed in section 2.2.1, to solve the system of coupled equations (2.24) and, therefore, to evaluate the excitation cross-sections. To get this result, the γ–ray angular distributions and the geometry of the γ–ray detectors with their detection efficiency are taken into account. In addition, many effects are included in the calculations, such as internal conversion de-excitation and relativistic corrections.

The calculated cross-sections are integrated over the scattering angle and the energy

loss in the target in GOSIA. For this reason, the particle-detector geometry and the target thickness have to be known. In GOSIA, datasets corresponding to various scattering angles can be simultaneously analysed to overdetermine the problem and to gain sensitivity to second-order effects. Moreover, known lifetimes of the excited states and experimental values of the branching and mixing ratios of decay transitions, obtained from complementary spectroscopic measurements, can be used to further constrain the analysis.

From the evaluated cross-sections, a sophisticated χ^2 minimization procedure is implemented to extract electromagnetic matrix elements (see section 2.1) from the experimental data, including an estimation of the errors. The additional available spectroscopic data are included in the global χ^2 minimization procedure.

The exact calculation of the number of coincidences is complicated by the possible dead time of the acquisition system and uncertainties related to the setup geometry as well as beam energy and intensity. For this reason, absolute measurements (comparison between experimental data and absolute cross-section) are commonly avoided, and different normalization procedures are used instead. The method adopted in this thesis exploits the normalization to a known lifetime of a state of the nucleus that is studied. In this way, it is not necessary to know absolute values for detector efficiencies and beam intensity. However, the beam-target combination has to be chosen carefully to avoid the energy overlapping of different transitions. Also, the normalization transitions have to be observed with high statistics, and the relative γ efficiency has to be known with high precision. This is the simplest normalization method when different states are excited in the same experiment, and the most employed, also because everything is fitted by the code and there are no additional calculations required by the user.

Further details regarding the GOSIA code can be found in [27], including examples of input files for simulations and data analysis.

Chapter 3

Target Characterization

To analyse data collected in Coulomb-excitation measurements, the energy of the beam, the thickness and the composition of the target need to be known. For this reason, the ^{96}Zr target employed in this work was characterized using the Rutherford Backscattering Spectrometry (RBS) method at the INFN LABEC[1] laboratory in Florence. This chapter describes the RBS method, the experimental setup, and reports the results of this measurement.
It must be pointed out that the target employed is a metallic foil with high enrichment of ^{96}Zr, however other Zr isotopes are also present as will be discussed in Chapter 5.

3.1 Rutherford Backscattering Spectrometry Method

Rutherford Backscattering Spectrometry (RBS) [28] is based on the use of a beam with known energy colliding with the sample to analyse, and the subsequent detection of the scattered beam at backward angles. By analysing the energy spectra collected with a detector (or a set of detectors) placed at known scattering angles, it is possible to extract specific target properties.

3.1.1 Kinematics of the Process

If the beam energy in the RBS measurement is maintained well below the Coulomb barrier, the scattering process can be considered elastic, and can be easily described by applying the principles of conservation of energy and momentum. For an incident particle of mass M_1, the initial velocity and energy are v and E_0. After the collision, the velocities and energies of the projectile and the target are (v_1, E_1) and (v_2, E_2), respectively, and they depend on the scattering angle θ and the recoil angle ϕ defined in figure 3.1.

[1] LAboratorio di tecniche nucleari per i BEni Culturali (laboratory for nuclear techniques applied to cultural heritage).

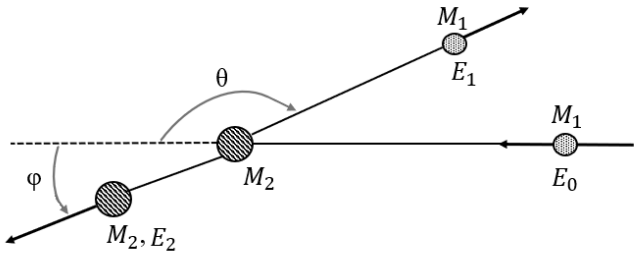

Figure 3.1: Elastic collision between a projectile of mass M_1 and a target of mass M_2.

Conservation laws of energy and momentum imply the following equations:

$$E_0 = E_1 + E_2 \Rightarrow \frac{1}{2}M_1v^2 = \frac{1}{2}M_1v_1^2 + \frac{1}{2}M_2v_2^2, \tag{3.1}$$

$$M_1v = M_1v_1\,cos\,\theta + M_2v_2\,cos\,\phi, \tag{3.2}$$

$$0 = M_1v_1\,sin\,\theta - M_2v_2\,sin\,\phi. \tag{3.3}$$

Extracting $cos\,\phi$ from (3.3), v_2 from (3.1), and replacing them in (3.2), the ratio v_1/v can be deduced:

$$\frac{v_1}{v} = \frac{M_1cos\,\theta \pm \sqrt{M_2^2 - M_1^2sin^2\theta}}{M_1 + M_2}\ . \tag{3.4}$$

Consequently, the ratio between the initial and final projectile energy, called *kinematic factor* K, is determined only by the masses and the scattering angle:

$$K = \frac{E_1}{E_0} = \left[\frac{M_1cos\,\theta \pm \sqrt{M_2^2 - M_1^2sin^2\theta}}{M_1 + M_2}\right]^2. \tag{3.5}$$

Equation (3.5) shows how the mass of the target M_2 can be determined by detecting the scattered beam and measuring its energy E_1 and the scattering angle θ.

In addition to the identification of the atomic species present in the target, RBS can also provide depth profiles. With reference to figure 3.2, the beam loses energy in the target in three ways:

- ΔE_{in} - energy lost on the inward path;
- ΔE_s - energy lost in the elastic scattering process;
- ΔE_{out} - energy lost on the outward path.

By exploiting the differences in the stopping powers for the different atomic species and, therefore, in the measured energy of the scattered beam, it is possible to reconstruct the composition of the target in the different layers.

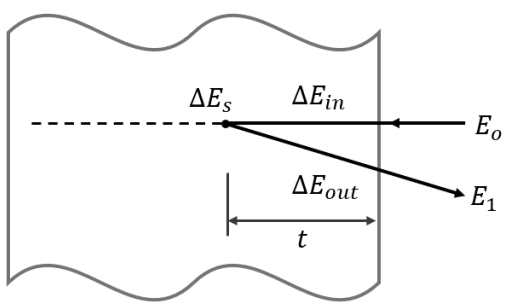

$$\Delta E_{in} \sim \left.\frac{dE}{dx}\right|_{E_0} \cdot t$$

$$E_t = E_0 - \Delta E_{in} \Rightarrow \Delta E_s = (1-K)\cdot E_t$$

$$\Delta E_{out} \sim \left.\frac{dE}{dx}\right|_{E_1} \cdot \frac{t}{\cos\theta}$$

$$E_1 = E_0 - \Delta E_{in} - \Delta E_s - \Delta E_{out}$$

Figure 3.2: Scattering in a depth profile.

The possibility to distinguish between two atomic species in the target that differ in their masses by ΔM_2 depends on the capabilities of the experimental setup to resolve differences ΔE_1 in the energies of scattered particles, indeed:

$$\Delta E_1 = E_0 \frac{dK}{dM_2} \Delta M_2 \Rightarrow \delta M_2 = \frac{\delta E}{E_0} \cdot \left(\frac{dK}{dM_2}\right)^{-1} . \tag{3.6}$$

By using (3.5) and (3.6) it can be demonstrated that ΔE_1 has a maximum for $\theta = \pi$, meaning that the differences in energy for the different atomic species are maximised at backward angles. This property is the reason why the detectors in RBS measurements are placed at backward angles, from which the name of the technique.

3.1.2 Scattering Cross-Section

The differential cross-section $d\sigma/d\Omega$ for scattering at an angle θ and in a differential solid angle $d\Omega$ is given by

$$\frac{d\sigma(\theta)}{d\Omega} \cdot d\Omega \cdot N_s = \frac{\text{Number of particles scattered in } d\Omega}{\text{Total number of incident particles}} \tag{3.7}$$

where N_s is the number of target atoms per unit area (see figure 3.3). In RBS measurements the employed particle detectors are typically small and, therefore, the detector's solid angle Ω is small ($10^{-2}Sr$ or less). In these conditions, it is useful to define an average differential scattering cross-section called *scattering cross-section*:

$$\sigma(\theta) = \frac{1}{\Omega} \int_{\Omega} \frac{d\sigma}{d\Omega} \cdot d\Omega \ . \tag{3.8}$$

The number of target atoms per unit area N_s is related to the yield Y (*i.e.*, the number of detected particles in an ideal 100% efficient detector that subtends a solid angle Ω) by the

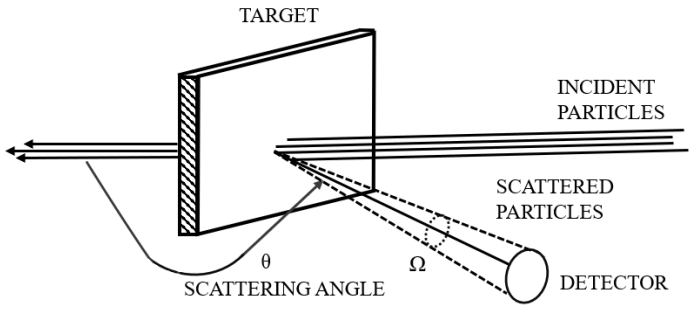

Figure 3.3: Simplified layout of a scattering experiment.

equation:

$$Y = \sigma(\theta) \cdot \Omega \cdot Q \cdot N_s \,. \tag{3.9}$$

Here, Q is the total number of incident particles in the beam and its value is determined by the time integration of the measured beam current. Considerations on the Coulomb repulsion acting between projectile and target during the collision lead to the following scattering cross-section formula:

$$\sigma(\theta) = \left(\frac{Z_1 Z_2 e^2}{4E}\right)^2 \left(sen^4\left(\frac{\theta}{2}\right)\right)^{-1} \,. \tag{3.10}$$

3.2 Experimental Setup

The RBS measurement performed at the LABEC laboratory to analyse the ^{96}Zr target employed a proton beam at an energy of 2 MeV. Three silicon detectors mounted in a vacuum chamber were used to detect the backscattered protons impinging on the target. The target was mounted on a rotating wheel allowing for its positioning without breaking the vacuum (see figure 3.4). A Faraday cup was used to measure the beam intensity.

In the employed setup, the detectors are placed at $165°$, $150°$ and $120°$ degrees with respect to the beam direction, at a distance of 91 mm, 61 mm and 91 mm, respectively. Collimators with the shape of a vertical slit are placed in front of each detector to select the scattering angle with high precision. With the use of the collimators, the active area of the detectors is reduced to a rectangle of 1×13 mm^2.

The rotating wheel hosting the targets is equipped with an X-Y movement in the plane perpendicular to the beam direction, managed by control software. A fluorescent SiO target was used to focus the beam with a precision of about 1 mm. Inside the vacuum chamber, a laser and a camera are also available for the focusing of the beam. Thanks to these instruments it was possible to carefully select the portion of the target to analyse.

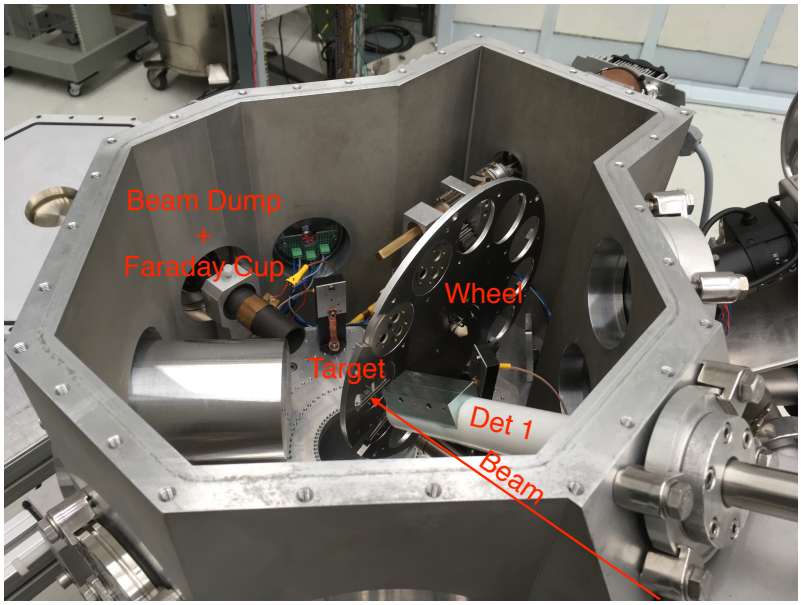

Figure 3.4: Picture of the setup used for the RBS measurement. The rotating wheel supporting the targets and one of the used silicon detectors are visible.

3.3 SIMNRA Code

SIMNRA is the reference code for the simulation and analysis of energy spectra of charged particles obtained in RBS experiments. The code includes elastic and inelastic scattering, as well as a selection of nuclear reactions and ion beams with energies ranging from 100 keV to several MeV. The program makes use of a database of about 3000 different cross-sections for different beam-target combinations and beam energies. SIMNRA can calculate the energy spectra for simple and complex geometries of the setup, and includes various experimental characteristics, such as the presence of dead layers in front of the detectors, finite energy resolutions, finite diffusion angles, and the effect of collimators placed in front of the detectors.

The simulation of a backscattering spectrum resulting from the interaction of an ion beam with initial energy E_0 on a sample is performed by SIMNRA by subdividing the latter into thin layers. The simulated spectrum is made up of the superimposed contributions from each element of each layer. The thickness Δx of each layer is chosen in such a way that the energy loss can be considered constant. When the incident particles penetrate a layer, they lose energy due to electronic and nuclear energy loss and the beam energy is spread due to straggling. As shown in figure 3.5, the contribution of each isotope in each layer constitutes an individual distribution. The area Q of the distribution is determined by the cross-section calculated at the average energy that the particles have in the layer, while the shape is determined by the effect of the stopping power, by the energy straggling in and out of the layer, and by the energy resolution of the detector. The program analyzes

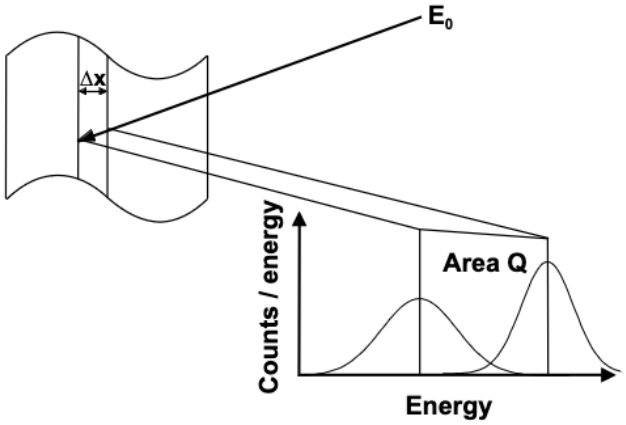

Figure 3.5: Notation used to identify the contribution of each isotope in each target layer.

one layer after the other until the sum of the thicknesses crossed by the beam is equal to the thickness set by the user or when the particles have completely lost their energy.

By using SIMNRA it is possible to simulate an RBS spectrum giving as an input the mass and charge number of the incident beam and its energy, the geometry of the experimental setup, the geometry of the detectors, the energy calibration parameters, and the target description (*i.e.*, the thickness and composition of the different layers). Also, the code includes a fitting procedure, based on the minimization of a χ^2 distribution, which allows for giving as an input an experimental spectrum and getting information about the target.

3.4 Results

Figure 3.6 shows the experimental RBS spectrum resulting from the ^{96}Zr target analysis at LABEC, considering the detector at 165° degrees. The spectrum is dominated by the contribution of the beam backscattered on ^{96}Zr, which produces a distribution in the $\approx 1.7 - 1.9$ MeV energy range. In the spectrum, the finite resolution of the detector, the energy staggering, and the target roughness produce a finite slope at the beginning and the end of the distribution associated with ^{96}Zr. This slope is larger at the beginning of the distribution (≈ 1.7 MeV) than at the end (≈ 1.9 MeV). The beam backscattered on the surface of the target corresponds to the higher energy in the spectrum, while the beam going through the target thickness and backscattering at the end of it corresponds to the last layer as seen by the beam. The slope in this last portion of the spectrum is larger than at the surface because the effects of the energy straggling and target roughness are maximum when going through the whole target thickness.

Other two smaller distributions are visible in the spectrum in figure 3.6. Their energies

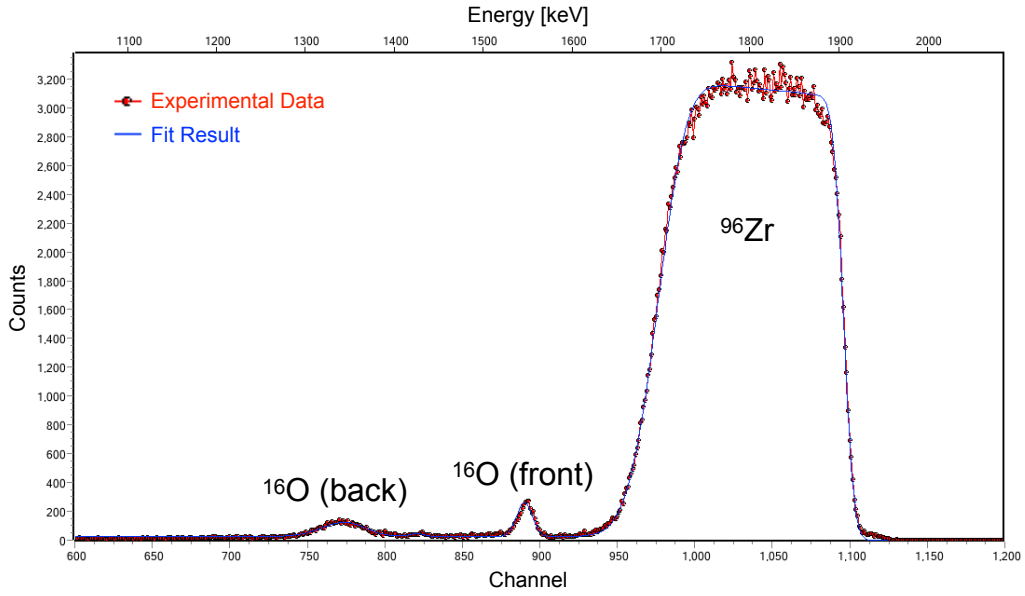

Figure 3.6: The experimental RBS spectrum collected with the silicon detector at 165° degrees is shown in red. The result of the fitting procedure performed with SIMNRA is shown in blue.

are compatible with ^{16}O diffused in the front and back surfaces of the target, which is produced by oxidation of the target. The distribution around 1.55 MeV corresponds to oxygen in the front layer as seen by the beam and has a lower Full Width at Half Maximum (FWHM). The distribution at around 1.35 MeV is associated with oxygen in the back layer and is wider than that on the front layer because of the larger energy straggling.

Figure 3.6 shows the result of the fitting procedure to the experimental spectrum assuming a 100% ^{96}Zr enriched target. The reproduction of the spectrum is satisfactory. The oxidized front and back layers have been approximated as unique layers with fixed distributions instead of a sequence of layers with a gradient in the composition of oxygen versus zirconium. This approximation is good enough for this work because of the low concentration of oxygen. Considering also the energy spectra at 120° and 165° degrees, the following target composition has been deduced:

- Layer 1 - ^{16}O, 2.7(11) μg/cm^2 + ^{96}Zr, 140(20) μg/cm^2
- Layer 2 - ^{96}Zr, 410(50) μg/cm^2
- Layer 3 - ^{16}O, 2.7(11) μg/cm^2 + ^{96}Zr, 140(20) μg/cm^2

These values are the results of the RBS measurement performed to characterize the ^{96}Zr target. They are used as an input for the Coulomb-excitation data analysis described in the following.

Chapter 4

Experimental Setup

In this chapter, the experimental setup used to study the ^{96}Zr nucleus is described (see figure 4.1). The experiment was performed at the INFN Legnaro National Laboratories (LNL) where a 160-MeV beam of ^{58}Ni, delivered by the TANDEM accelerator, impinged on a ^{96}Zr target. The γ–rays emitted by the de-exciting projectile and target nuclei were detected by the AGATA array, which is described in section 4.1. The back-scattered projectiles were detected by the SPIDER array, which is described in section 4.2. The digital acquisition system used for both AGATA and SPIDER is described in section 4.3.

4.1 AGATA Array

AGATA (Advanced GAmma Tracking Array) [29, 30] is a European research project to develop and build a new generation 4π γ-ray spectrometer. In the AGATA collaboration, 40 research institutes and 13 European countries are involved: Bulgaria, Germany, Italy, Finland, France, Hungary, Poland, Romania, Slovenia, Spain, Sweden, Turkey, and the UK. The idea of AGATA is to make use of highly segmented HPGe (Hyperpure Germanium) crystals to detect not only the energies of the photon interactions within the array but also their positions. This allows for the reconstruction of the path taken by the γ–ray, as will be discussed more in detail in the following sections. The ability to reconstruct the γ–ray trajectories makes using Compton shields unnecessary so that the solid-angle coverage can be maximised. Therefore, the array combines the high energy resolution of the HPGe detectors with high efficiency and angular coverage.

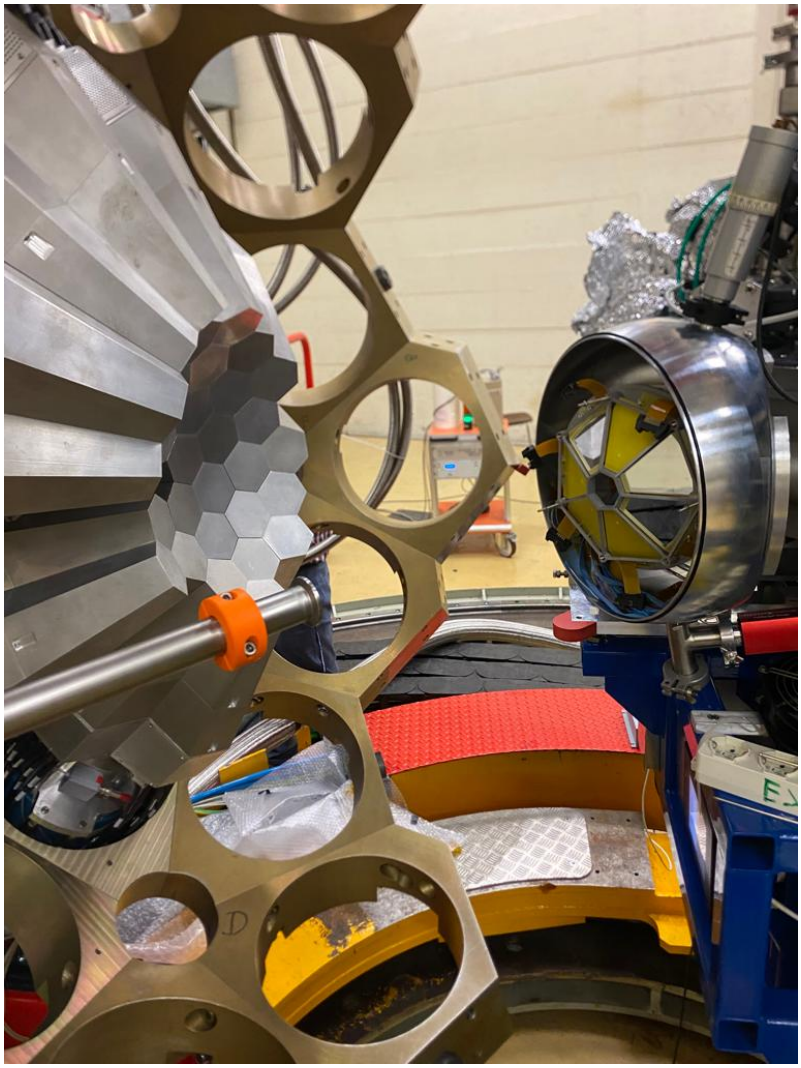

Figure 4.1: The experimental setup, composed of the AGATA and SPIDER arrays.

4.1.1 AGATA Detectors

The AGATA array consists of closed-end, coaxial HPGe crystals tapered with a hexaconical shape (hexagonal in the front, circular in the rear). These crystals have a diameter of 8 cm, a length of 9 cm and are electrically segmented into 36 segments (6 longitudinal, 6 transversal) with a common central hole (core), as shown in figure 4.2. The core has a diameter of 1 cm and extends to 1.3 cm from the front end. All crystals are made of n-type HPGe material with an impurity concentration specified to be between $0.4 \cdot 10^{10}$ cm^{-3} and $1.8 \cdot 10^{10}$ cm^{-3}. The surfaces of these crystals are very delicate; therefore each crystal is encapsulated into a hermetically sealed aluminium canister with a 0.8 mm wall thickness. The distance between the capsule walls and the crystal side faces is from 0.4 mm to 0.7 mm.

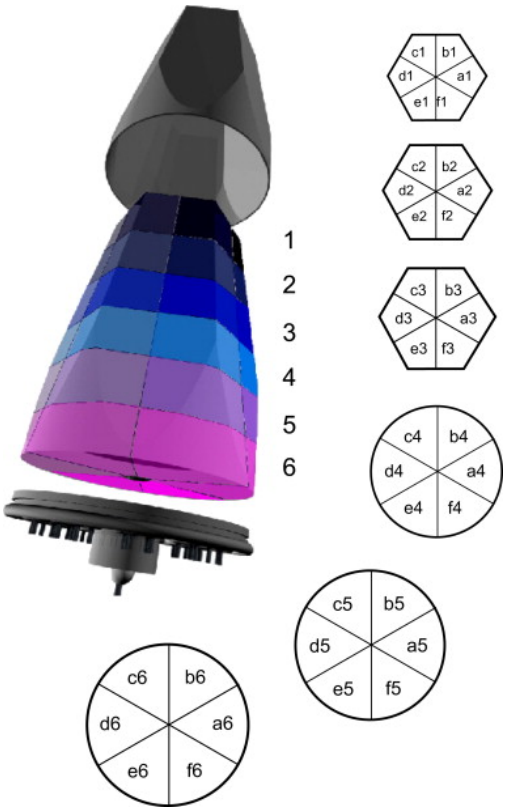

Figure 4.2: Scheme of the AGATA capsules [29], labelled with rings 1 - 6 and sectors a - f.

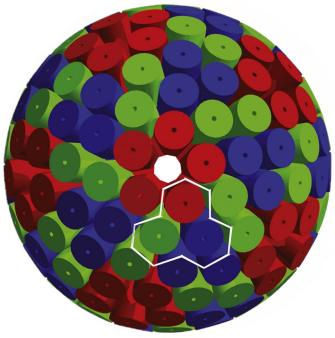

Figure 4.3: AGATA 4π spectrometer [29]. The white line indicates a triple cluster.

To fit into the 4π geometry (figure 4.3), three types of detectors are employed, which differ in their irregular hexagonal shape identified by a letter and a colour as shown in figure 4.4: type A (red), type B (green) and type C (blue). This triplet of crystals represents the AGATA Triple Cluster (ATC). It contains 114 high-resolution spectroscopy channels because each crystal provides 38 independent outputs, 36 from the segments and 2 from the central contact.

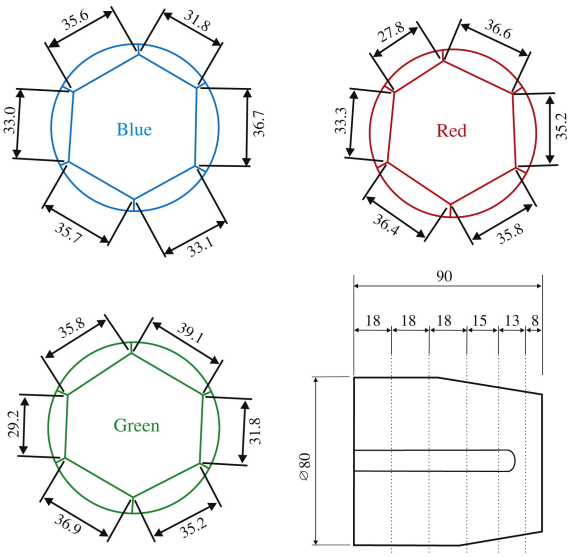

Figure 4.4: Drawing of the three AGATA crystal geometries [29]. Dimensions are given in mm.

In each crystal, the central contact collects the electrons, while the segment contacts collect the holes produced locally. This means that the signal amplitude measured by the core equals the sum of the signals in the segments.

To achieve the best performance, the AGATA HPGe detectors must be maintained at a temperature of ∼80 K. This condition is reached by placing the triplet of crystals in identical cryostats with a system for the periodic liquid nitrogen (LN_2) filling. Installed on the ATCs there are the AGATA charge-sensitive preamplifiers, which have been designed to fulfil the requirements needed for fast and clean transfer function for Pulse-Shape Analysis (PSA, see section 4.1.3) and high-counting rate capability. The AGATA cryostats employ a separated cooling scheme for the encapsulated Ge detector and the cold part of the preamplifier electronics, which is operated at temperatures near 130 K where their noise contribution is minimal. The other adjacent parts of the preamplifier electronics contribute less to the noise performance and are therefore situated outside the vacuum, where they are readily accessible (see figure 4.5).

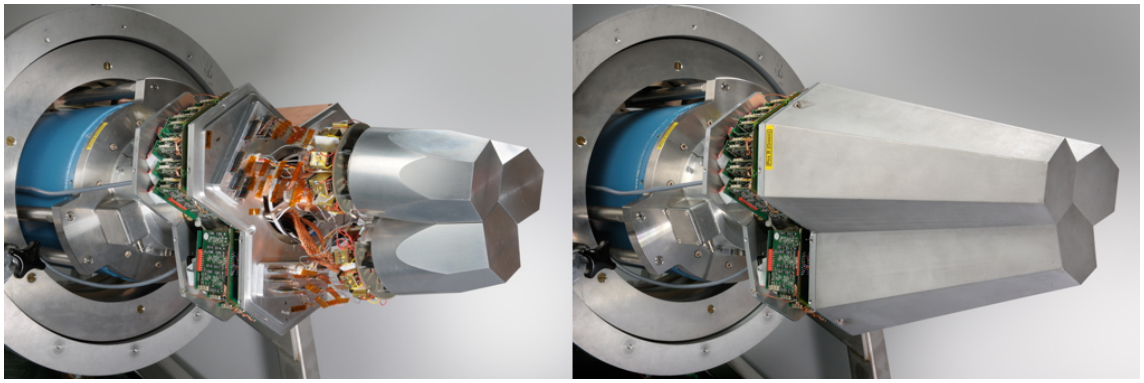

Figure 4.5: Picture of an AGATA triple cluster with (right) and without (left) the aluminium canister. The preamplifier electronics and the Dewar are also visible. Adapted from Ref. [31].

AGATA requires a mechanical structure to accurately support the detector elements and enable their safe insertion and removal. The support structure consists of identical flanges, one for each detector module, assembled to produce a solid structure called *honeycomb* (visible in figure 4.1). The detectors are mounted on the honeycomb with a 0.5 mm space between the sides of two neighbouring ones, with the smallest sides facing the centre of the reaction chamber to achieve a uniform coverage of the solid angle. The distance between the target and the AGATA detectors can be adjusted from the so-called *nominal position*, *i.e.* at a distance between the target and the front of all the ATCs equal to 230 mm, to the *close-up position*, in which the array is translated towards the target by 55 mm.

In the experiment described in the present work, AGATA was in the close-up position and the array was composed of 11 ATC. In the analysis, 28 crystals were considered.

4.1.2 Front-End Electronics

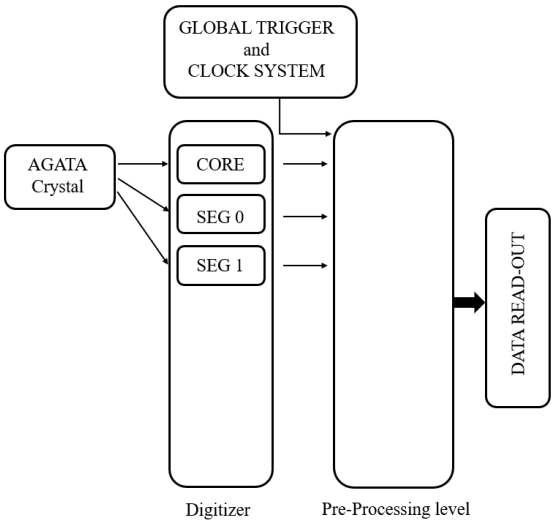

Figure 4.6: Simplified and schematic view of the AGATA front-end electronics and data readout system.

The AGATA Front-End Electronics (FEE) considers the crystals as separate entities. The FEE, for each detector, is made up of a preamplifier, digitizer and pre-processing electronics (see figure 4.6). The digitizer is the interface between the detectors and the signal-processing system. It receives the 38 preamplifier outputs and digitizes them with a sampling rate of 100 MHz and a resolution of 14 bits. Then, the ADC data are sent via optical fibres to the pre-processing stage. Here, the energy and time information for each waveform (trace) are extracted. The energy is obtained by applying a trapezoidal filter, while the first timing information is obtained by using the core signal as a trigger for the whole detector. Therefore, when a pulse is registered in the core, a *local-trigger* output indicates to all the segment electronics that they should also extract a trace from the data stream.

The pre-processing electronics sends the filtered data to the PSA algorithm (see section 4.1.3), which calculates the positions of the γ–ray interactions. The PSA requires timestamped data based on a common clock. The synchronization among the different elements and time tagging is made by the Global Trigger Synchronization (GTS) system, which can perform further filtering according to a trigger processor. In the experiment subject of this work, the additional request (*global trigger*) was a γ–particle coincidence event with SPIDER.

4.1.3 Pulse-Shape Analysis

The interaction of a γ–ray in the detector produces a pulse of current that can be studied to determine the position of the interaction. For instance, the difference in drift velocity between holes and electrons makes the signal dependent on the distance of the interaction from the core central contact (figure 4.7). The Pulse-Shape Analysis (PSA) algorithm in AGATA compares the measured signals in each segment of the crystal with a library of traces corresponding to simulated interactions in a grid of points that maps the crystal volume. This database is called AGATA Detector Library (ADL) and contains simulated pulses of every segment (and core) for the different interactions in the detector. However,

the signals are not only produced in the segments where the interactions take place. Mirror charges (transient electrical signals) can be generated in segments near the one that has been hit. These shapes can also be analyzed because they are dependent on the interaction position. The difference between these two phenomena is that the signal obtained in the hit segment has a net charge with a non-vanishing integrated current, while the integral of the transient signal over the collecting time is zero. The inclusion of this aspect in the algorithm provides an improvement in the determination of the interaction positions.

For an individual AGATA detector, the core energy resolution (Full Width at Half Maximum, FWHM) is specified to be better or equal to 2.35 keV at 1.33 MeV, while the segment FWHM at 1.33 MeV is specified to be better or equal to 2.30 keV. The nominal position resolution depends strongly on the energy of the incident γ–ray [32], and its reference value is set at around 4-5 mm. In practice, both quantities depend on the state of the crystal, namely how much neutron damage is affecting the detector, as will be observed in section 5.1.1.

While the shape of the signal determines the impact position, the total collected charge extracted by applying the trapezoidal filter (see section 4.1.2) is proportional to the deposited energy.

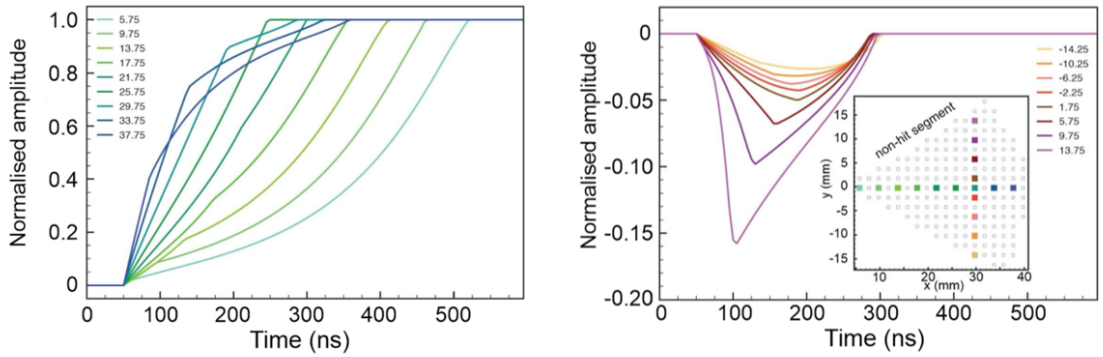

Figure 4.7: (Left) Core signals for different interaction radial positions. Close to the core, the faster electrons are collected immediately while the slower holes still have to drift to the segment electrode. The shortest rise time occurs at an intermediate position. Far from the core, the time for the electrons to be collected is longer than for the holes. (Right) Transient signals. Depending on the distance of the interaction, the amplitude of the transient signal changes. Adapted from Ref. [33].

4.1.4 Gamma-Ray Tracking

A γ ray usually has multiple interactions in AGATA. There can be more than one interaction in one segment or even in multiple segments. The tracking algorithm aims to reconstruct the trajectories of the incident photons to determine their energy and direction. To do this, the algorithm must disentangle the interaction points identified in the

detectors and establish their proper sequences. PSA extracts information on the deposited energy, time, and position of a hit in the detector. However, only a fraction of these interactions provides complete awareness about the original energy of the incident γ ray. The γ ray can interact in the detector with different processes, mainly photoelectric absorption, Compton scattering, and pair production. In photoelectric absorption, all the energy of the γ ray is released in one hit and, therefore, this event contributes to the photopeak in the energy spectrum. In Compton scattering, instead, the γ ray scatters on an electron releasing part of its energy and deviating from the original direction. After this interaction, the γ ray at lower energy can undergo further scatterings and usually is absorbed with a final photoelectric interaction. The partial energy deposit of one Compton-scattered γ ray in a segment of the detector populates the so-called Compton continuum in an energy spectrum, which contributes to the background for γ–ray spectroscopy. Lastly, in pair production, a γ ray passing through matter has the possibility of interacting producing an electron-positron pair. The cross-section of these processes has a strong dependence on the γ–ray energy, as shown in figure 4.8. For low-energy γ rays, the dominant process is photoelectric absorption, while for γ rays beyond hundreds of keV, the typical energy transfer happens through multiple Compton scatterings and a final photoelectric absorption. Therefore, a large fraction of the interactions in the detector will not carry the information on the total energy of the γ ray and thus, the tracking algorithm deals mainly with the Compton-scattered γ rays to reconstruct the total energy of the photopeak.

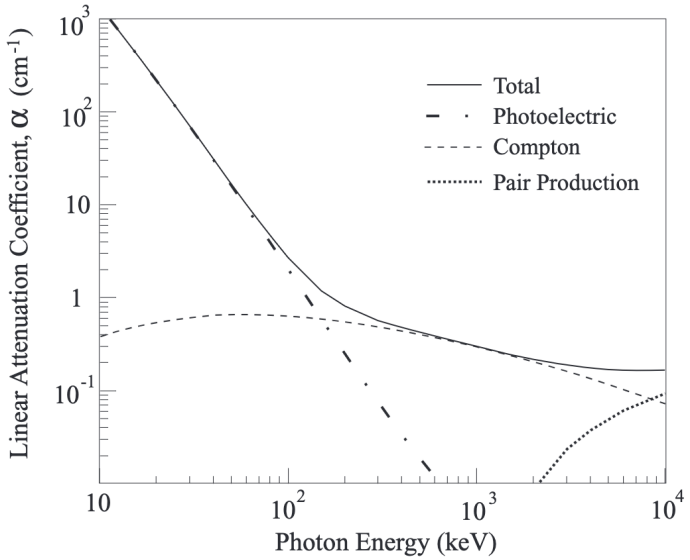

Figure 4.8: Linear attenuation coefficient of different interaction processes of γ rays in germanium at different energies.

Tracking algorithms can be divided into back-tracking and forward-tracking [34]. The feature of back-tracking algorithms is to start to reconstruct the track from the final photoelectric interaction, expected in a fixed energy range of $\approx$ 100 - 200 keV. In forward-

tracking algorithms, instead, the first step of the procedure is to group interaction points into clusters in the (θ, ϕ) space. The most commonly used algorithm with AGATA is the Orsay Forward Tracking (OFT), which belongs to the second category.

4.2 SPIDER Array

SPIDER (Silicon PIe DEtectoR) is an array of heavy-ion detectors developed by the INFN Division of Florence [35] for low-energy Coulomb-excitation measurements. SPIDER is a modular array of trapezoidal-shaped silicon detectors, each one covering $45°$ in the azimuthal angle and 300-μm thick, with dead layers of 50 nm on the junction side and 350 nm on the ohmic side. The detectors are segmented on the front surface (junction side) into eight annular strips, while the back surface (ohmic side) is not segmented (see figure 4.9). A guard ring is located around the strips and, properly biased, minimizes the field distortion effects. The bulk resistivity of the detector is around 3400 Ωcm and the full depletion voltage is 100 V, with a recommended bias of 120 V. The biasing can be performed either independently for each strip or simultaneously for the whole detector.

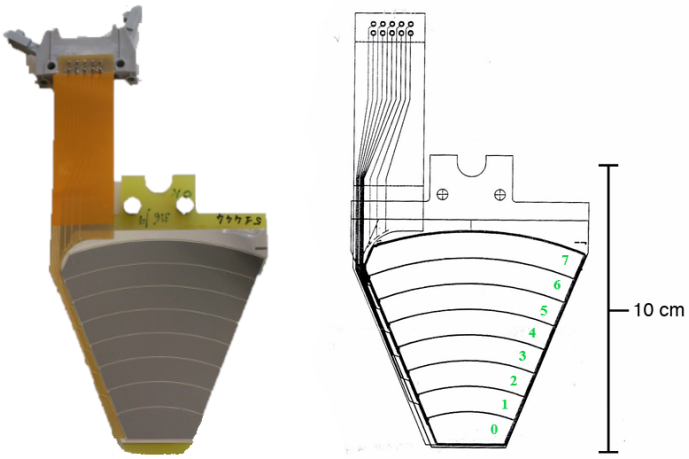

Figure 4.9: Picture (left) and schematic view (right) of one of the SPIDER detectors from the junction side. The 8 strips and the guard ring are visible. The strips are labelled starting from the bottom to the top from 0 to 7.

4.2.1 SPIDER with AGATA

When used with AGATA, SPIDER consists of 7 detectors arranged in a cone-like configuration (see figure 4.10). The distance between SPIDER and the target position can span from 9 to 11 cm, and the angular coverage ranges from $126°$ to $162°$ for the 9 cm distance

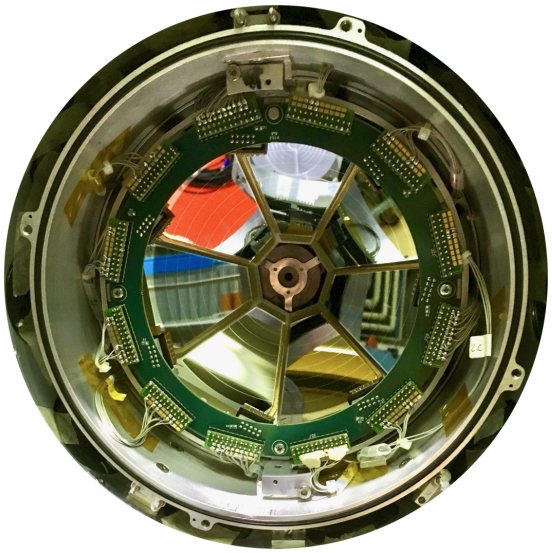

Figure 4.10: SPIDER array in the cone-like configuration.

and from $134°$ to $165°$ for the 11 cm distance (the angles are given relative to the beam direction). The solid-angle coverage is $\approx 16\%$ and $\approx 12\%$ of 4π in the two configurations, respectively.

The ancillary detector and the target are hosted in a vacuum chamber (see figure 4.11). The scattering chamber, for the AGATA installation at LNL, is characterized by a reduced thickness to minimize γ–ray absorption and a service chamber, also named *expansion chamber*, where beam dumps, cables, and front-end electronics for the complementary detectors can be placed (see figure 4.12). The chamber design comprises two independent shells, one rigidly connected, and a set of movable shells that allow the coverage of a wide angle range. The outer radius of the movable shells is 170 mm, resulting in a large space inside the chamber.

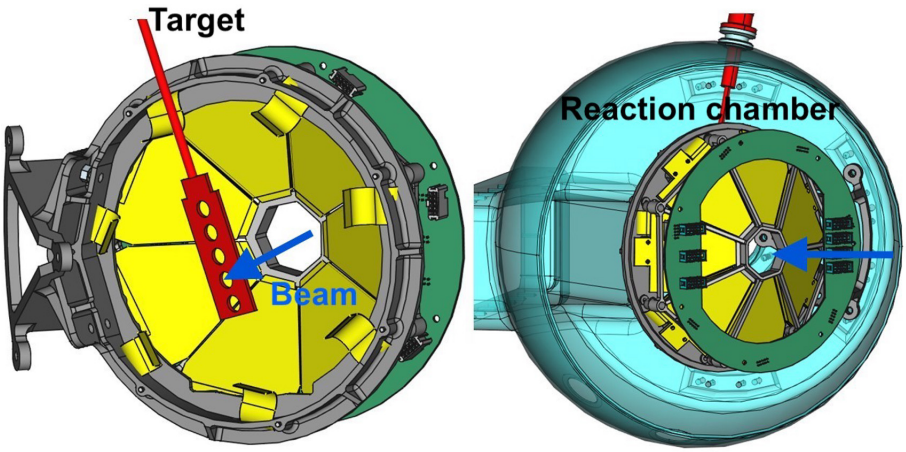

Figure 4.11: CAD visualization of SPIDER mounted in the AGATA reaction chamber from the front (left) and back (right) view. SPIDER is shown in yellow, the target holder in red, and the PCB ring in green. In the right figure, the AGATA reaction chamber is also shown, in cyan. Adapted from [36].

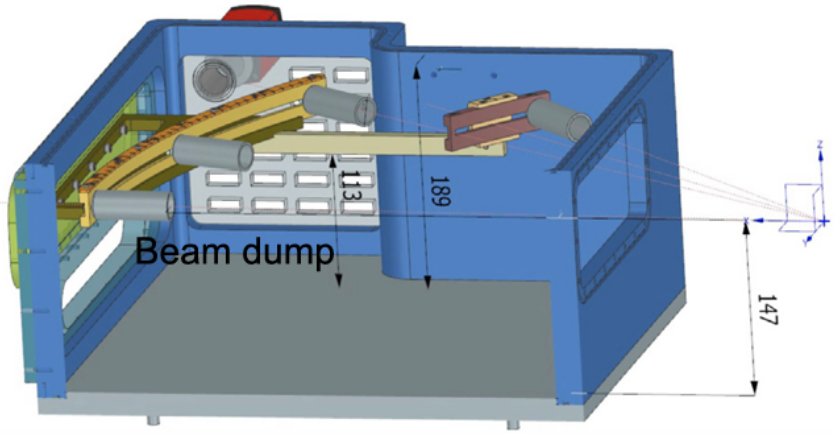

Figure 4.12: Inner view of the expansion chamber where the position of the beam dumps and of flanges for connectors is visible. All numbers are in mm. Adapted from [36].

4.2.2 Read-Out Chain

SPIDER uses two standard MesyTec MPR64 preamplifiers [37]. A dedicated Printed Circuit Board (PCB) is employed to connect the individual SPIDER detectors and the dedicated preamplifiers, and is mounted inside the AGATA reaction chamber as shown in figure 4.11. The SPIDER Read-Out chain is depicted in figure 4.13.

Figure 4.13: Schematic view of the ancillary read-out chain.

Differential signals from the preamplifiers are converted to single-ended ones and sent to CAEN V1725 digitizers [38]. The digitizers produce events which, by means of the read-out unit, are sent to a local filter. This one converts the data from the raw format to the AGATA Data Format (ADF). In the end, a builder unit merges ADF frames based on timestamps. The coupling of AGATA to SPIDER (or any other complementary detector) has two topics of particular importance:

- the AGATA clock distribution works at 100 MHz;
- the clock counter common to all the AGATA electronic branches is not dependent on whether the acquisition is running or not, while the clock signal for SPIDER is internally generated by the boards and it is reset at each start of the acquisition.

To merge the AGATA-timestamp system with the SPIDER front-end circuit, an interface to the GTS system has been developed, called AGAVA. The AGAVA module receives the

trigger requests from the complementary detector, which is passed to the GTS system, and waits for the validation or rejection signal, also produced by the GTS.

4.3 AGATA DAQ

As shown in figure (4.14), the AGATA Data-AcQuisition system (DAQ) receives the preamplifier raw data from the FEE (signal amplitudes, timestamps, and digitally recorded waveforms) and processes them into several stages. Briefly, after the PSA, data from all crystals are merged taking into account the chosen AGATA trigger mode (see section 4.1.2), the γ–ray paths are reconstructed by the tracking algorithm and, finally, the storage of the events is carried out.

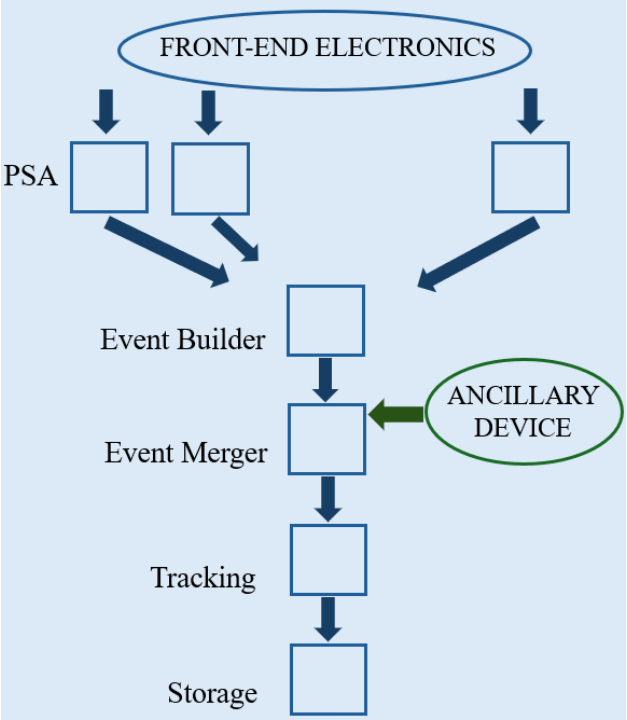

Figure 4.14: Layout of the AGATA data-acquisition system.

The AGATA data acquisition system is managed by the *Nouvelle Aquisition temps-Reel Version Avec Linux*[1] (NARVAL) framework. NARVAL is a highly distributed data acquisition system running across a network and acting like a single program that transports the data to the storage of the reconstructed events. The NARVAL data flow software incorporates a *local-level processing* approach that treats each crystal as an independent entity (it maintains the separation introduced by the FEE) throughout the entire process until the event-builder stage. Here, individual crystal data are merged based on their respective timestamps. This step constitutes the transition to the *global-level processing*. To effectively handle the significant amount of data generated, in addition to the offline sorting procedure, NARVAL integrates online and near-online PSA, γ–ray tracking, and data-analysis tools, thus enabling real-time experiment checks and optimization [39]. NARVAL is organized into *actors* (blocks of actions) corresponding to separate processes that receive and send out data at any stage of the chain. The actors are classified in the following categories:

- *Producers* - read data from the electronics (start a NARVAL chain);

[1] Meaning New Aquisition in Real-time Version Alongside Linux.

- *Filters* - perform operations on the data flow (calibrations, PSA, tracking);
- *Dispatchers* - merge several NARVAL chains in one (event builder, event merger);
- *Consumers* - close a NARVAL chain and write data on disk.

PSA and tracking are intermediary actors since the former is connected to the input data, while the second to the output data. The AGATA data are processed through consecutive calls of NARVAL actors. The sequence of actors chosen for the processing is called *topology*.

Before any processing, an actor is initialized using a configuration file containing the required parameters. To manage the configuration files needed by the actors, a Python script is provided. The script is divided into a few sections, some of which are specific to the offline analysis of each experiment. To optimize the parameters to get the best quality for the data, it is required to apply one or several times the same algorithm, using different configuration files. This is done using *emulators*, *i.e.* frameworks in charge of organizing and running the data processing by the different actors. In this regard, FEMUL (Flat EMULator) is used to run topologies, which is called a *replay*. The spectra produced by the actors are saved in a specific format that can be read by specific analysis tools. One of the most used is TkT [40], a software that displays the spectra from each segment in a crystal all together in a 6×6 grid. The columns of the grid correspond to the radial sectors of the crystal and are labelled with letters $(a - f)$, while the rows refer to the longitudinal segmentation and are labelled with numbers $(1 - 6)$, see figure 4.2. As explained in the next chapter, at the end of the data flow chain, the results are saved in Root files [41].

Chapter 5

Data Reduction

This chapter describes the analysis performed to obtain the experimental γ–particle coincidence spectra from the AGATA and SPIDER setup. The data sorting for AGATA and its calibration are described in section 5.1, while section 5.2 reports the procedures used for the energy calibration of SPIDER. The conditions for selecting the γ–particle coincidences and obtaining the calibrated Doppler-corrected γ–ray spectra are described in section 5.3.

5.1 AGATA

As introduced in section 4.3, the AGATA data analysis is carried out in two stages: the local-level processing, in which the crystals are treated independently, and the global-level processing, in which the different crystals are merged. In the following sections, the roles of the different actors employed in the present analysis will be described. Section 5.1.3 reports the AGATA efficiency measured for the experiment of this work.

5.1.1 Local-Level Processing

In the present analysis, the following *filters* have been used at the local-level processing: *prerocessing*, *PSA*, and *postPSA*. The *preprocessing* filter prepares the traces for the PSA filter. In doing the comparison of the measured signals with the reference basis, the *PSA* filter assumes that the amplitudes of the waveforms are in keV, that all the traces have the same starting time, and that all the segments are properly working. For this reason, the signals have to be calibrated and the traces corresponding to different segments should be aligned. Also, the correct functionality of the segments has to be checked. The *postPSA* filter is responsible for a series of actions that can be performed on the PSA hits, *e.g.* the neutron-damage correction.

Preprocessing Filter

Energy Calibration

A good energy calibration is essential to obtain good performances of the PSA and tracking algorithms. The energy calibration is carried out using a ^{60}Co and ^{152}Eu sources. The calibration, in the case of segmented HPGe detectors, are obtained with longer measurements than traditional detectors to have enough statistics in the segments further from the source. For each segment and core signal the calibration coefficients are deduced from the most intense transitions recorded in the amplitude spectra. The peak positions of these transitions are automatically searched and fitted by an automatic script (called *RecalEnergy*) using a linear function without offset. Figure 5.1 shows the segment amplitude spectra for the tree crystals of one ATC (ATC-06) acquired with a ^{60}Co source, before and after the calibration procedure. The peaks in the spectra at the bottom are aligned thanks to the energy calibration.

Crosstalk and Corrections for Malfunctioning Segments

The crosstalk is an electronic feature affecting segmented detectors and is due to the electronic coupling among channels. It causes spurious signal components yielding amplitude losses and fold-dependent shifts in the energy of the spectral lines. The crosstalk affects the energy resolution of the detector since the gain varies depending on the number of firing segments (segment multiplicity). A ^{60}Co source is used to obtain the parameters for the crosstalk correction. The automatic procedure sorts the energies recorded in the segments according to the segment multiplicity n_s. Hence, for each n_s, the shift from the nominal energy of the two strong transitions of the ^{60}Co source is deduced to build the crosstalk matrix of coefficients. These matrices are used for the correction of the measured energies.

It should be noted that the producer data used for the calibration step is sorted with the condition that just one segment per crystal is fired ($n_s = 1$). This condition allows for considering each segment as an individual detector, thus avoiding the incorrect determination of the calibration coefficients due to the crosstalk effect for higher n_s values.

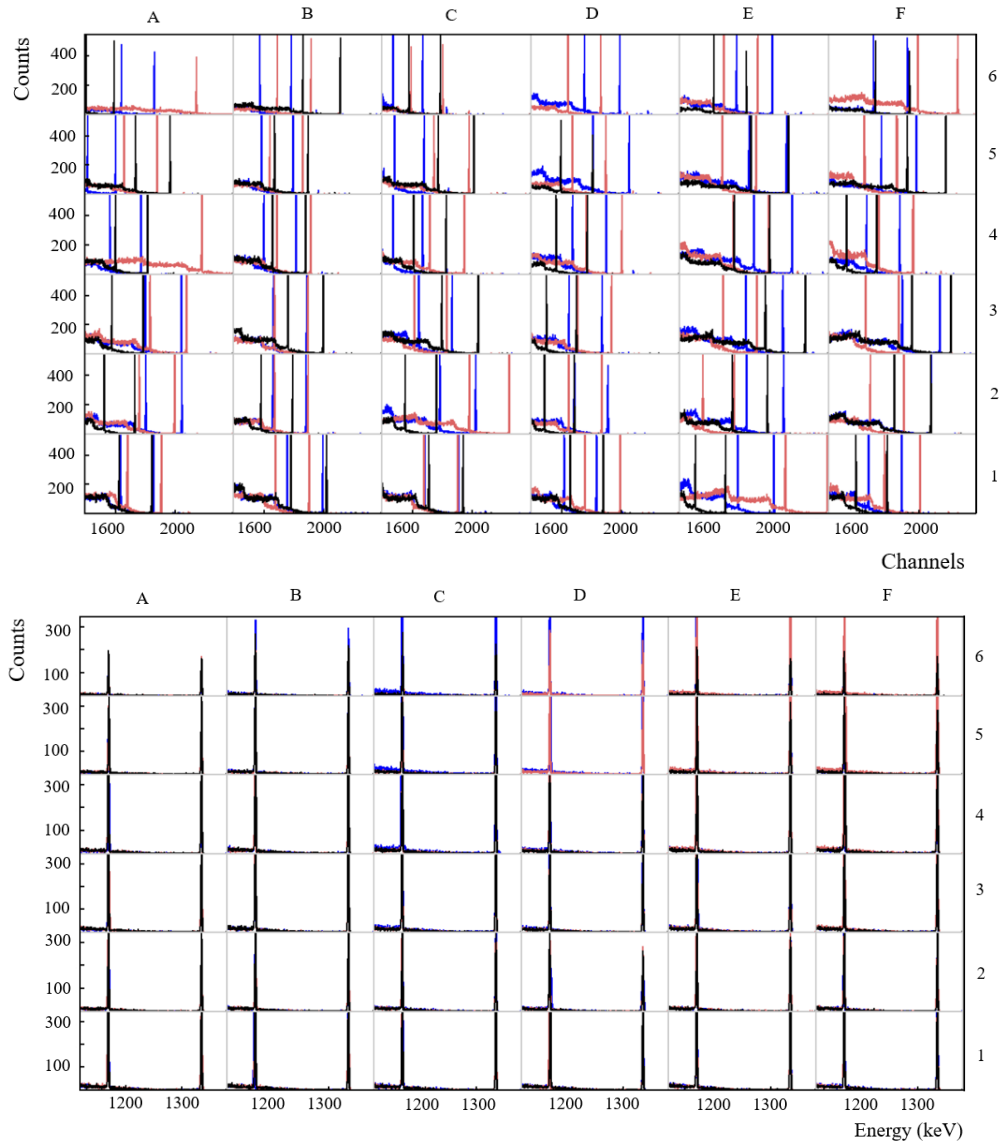

Figure 5.1: (Top) **Producer**: segments amplitude signals. Overlap of ^{60}Co γ–ray spectra for the ATC 06 (06A in pink, 06B in blue and 06C in black). The labels for columns and rows correspond to the nomenclature used in figure (4.2), hence 1 and 6 mean front and back segments of the crystal, respectively. (Bottom) **Preprocessing**: segments calibration. Overlap of ^{60}Co γ–ray spectra for the ATC 06 (06A in pink, 06B in blue, and 06C in black) calibrated in energy.

Sometimes the AGATA crystals can present some malfunctioning segments. This category includes segments either without signals or with extremely noisy ones and segments that show multiple peaks or broader peaks in the energy spectra. In figure 5.3, an example where the energy spectrum of the ^{60}Co source of the crystal 10B is reported: the segments D5, F3, and C2 are clearly malfunctioning. In such cases, it is possible to recover up to one segment per crystal considering that the sum of the energies released in the segments should be equal to the energy observed in the core (see section 4.1.1). When all the segments in a crystal function correctly, the correlation between the two quantities should

follow the bisector as shown in the top part of figure 5.2. In the same figure at the bottom, the correlation for a crystal in which not all the segments work properly is reported.

Time alignment

The signals in the database used for the PSA (section 4.1.3) have been calculated for an ideal detector and hence are well aligned in time [42]. Time misalignment between measured signals can lead to a wrong reconstruction of the interaction point. Therefore, a good performance of the PSA algorithm requires that traces corresponding to different segments of the same crystal are aligned in time. The traces corresponding to the different segments can be aligned in time to the core trace for each crystal, using a set of shift coefficients. These are obtained for each segment acquiring timing spectra when using the core as a trigger. In this way not only the signals are aligned "inside" the crystal, but also among different crystals, since the core signals can be aligned as well based on the "time-zero" histogram as found by the PSA actor (see figure 5.4).

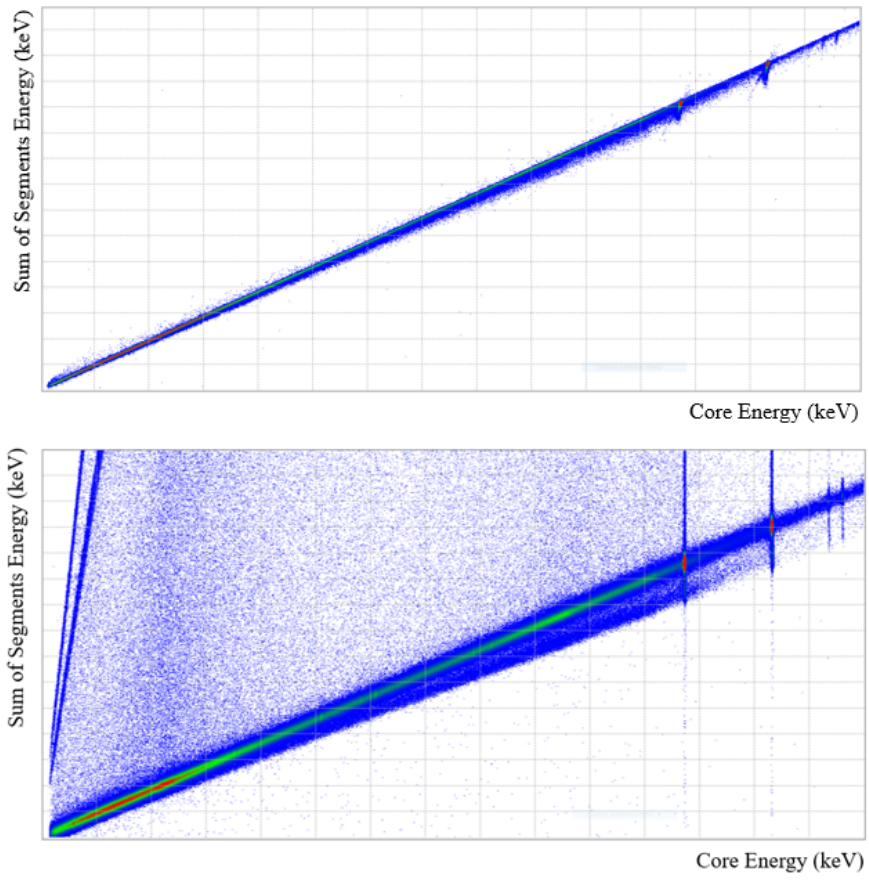

Figure 5.2: Matrices that show the correlation between the energy measured by the core and the sum-energy of all segments. If all function properly the correlation should follow the diagonal as in the case of crystal 05B (top). If not all the segments work properly, the matrix will show an anomalous correlation as for the crystal 08B (bottom).

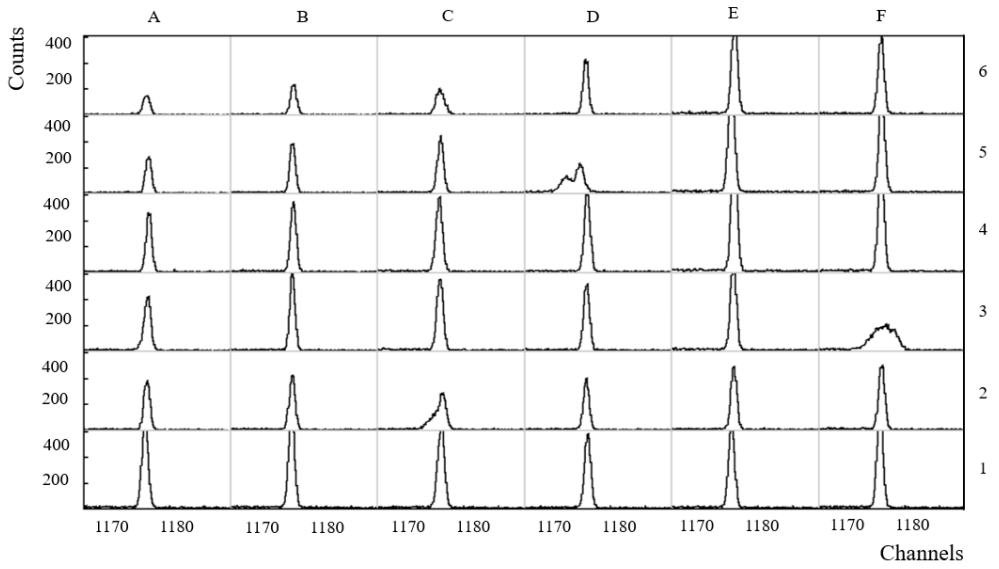

Figure 5.3: Spectrum of the 1.17 MeV γ–ray transition in ^{60}Co for the crystal 10B after the energy calibration. The malfunctioning segments C2, D5 and F3 were removed from topology.

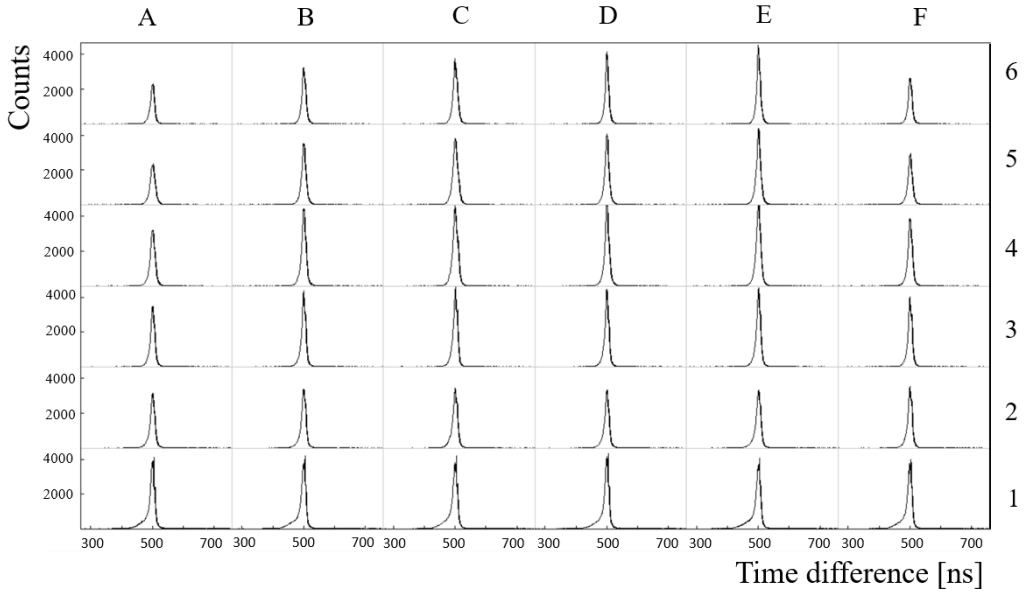

Figure 5.4: **Preprocessing**: segments time alignment to the core. Time spectra of the segments relative to the core for the crystal 00C after the time alignment.

PostPSA Filter

The PostPSA filter implements a set of corrections and refinements, such as neutron damage corrections, final energy calibration, and global time alignment.

Neutron damage correction

In the course of experiments, fast neutrons are produced in different types of reactions. The irradiation of the germanium crystals by fluxes of fast neutrons produces defects in the semiconductor lattice structure, which act as traps for charge carriers. This effect causes the charge collection at the electrodes to be partial and therefore the signal amplitude can be lower than the energy released in the interaction. The typical effect of this damage is a left tail on the peaks. The detector deterioration increases over time and its correction is mandatory to obtain a satisfying energy resolution.

The lattice damage could be recovered by the annealing of the crystals, but this procedure is impractical to apply after every experiment. However, thanks to the high position resolution of the interaction points obtained with the PSA algorithm, it is possible to correct charge trapping effects [43]. In fact, the charge carrier's collection efficiency depends on their travel path to the electrode, which can be easily obtained from the position of the interaction given by the PSA. The aim is to reconstruct the original γ-energy considering the fraction of charge that was not collected. This is obtained by building a grid of correction coefficients, for all the detector channels. Applying them to the PSA hits, it is possible to determine the one that minimizes the FWHM and the left tail of the peaks in the spectra.

During the experiment subject of this thesis, neutron damage was observed on six crystals: 05B, 08A, 08B, 08C, 10C, 11A, and 11B. The correction coefficients were derived from the ^{60}Co calibration run. The result of the correction procedure is shown in figure 5.5 for the crystal 05B.

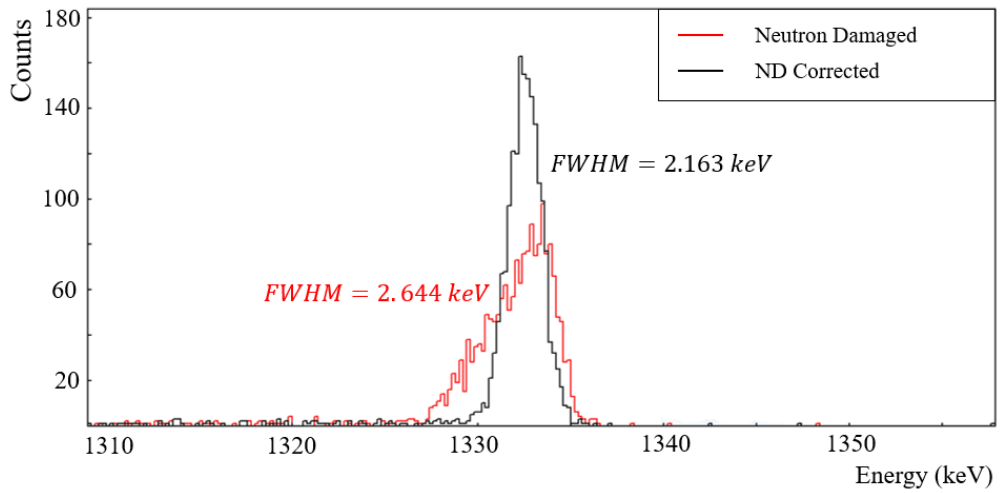

Figure 5.5: **PostPSA**: Neutron damage correction for segment C3 of crystal 05B. Spectra of the 1.3 MeV γ-ray transition in ^{60}Co before (red) and after (black) the correction. (Bottom). The peak after the correction shows an improvement of the FWHM around 18%.

The correction for electrons and holes trapping it is also done for the signals from the core. However, since the AGATA crystals are n-type HPGe detectors, the defects in the lattice caused by neutron irradiation trap more efficiently holes. As a consequence, the effect of the charge trapping on the electrons collected at the central contact is much less than on the holes collected in the segment contacts.

Energy recalibration

After the neutron damage correction, the energy calibration coefficients are refined. A recalibration is applied to all segments and afterwards to the sum of segments and to the core. This time, the calibration function is a linear one with an offset and is evaluated using a ^{152}Eu source, spanning a wider energy range (120 to 1400 keV). The result of this procedure is shown in figure 5.6 for the 11B crystal.

At this level, one can force the sum of the energies of all the segments fired in an event to the value of the energy measured in the core contact. This action reduces the effects of non linearities and/or of not proper functioning of some of the segments.

This procedure can be disadvantageous in the case of high counting rates, as the central core signal suffers a higher pile-up than the segments.

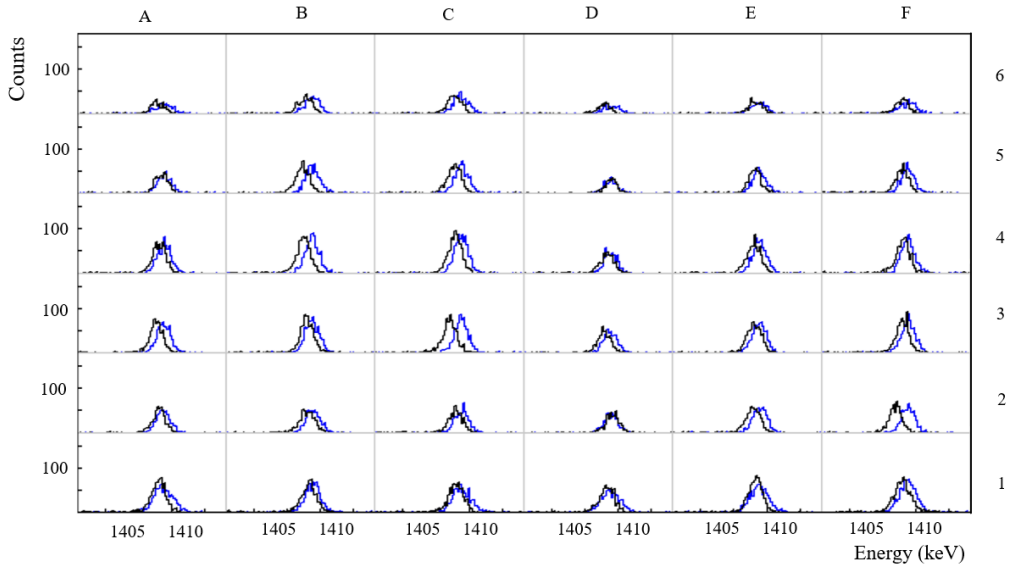

Figure 5.6: **PostPSA**: energy recalibration. Spectra of the 1.408 MeV γ- ray transition in ^{152}Eu for the crystal 11B after NDC (blue) and after recalibration (black).

Global Time alignment

The 36 segments of each crystal are aligned to the respective core in the preprocessing phase (section 4.1.2). The PostPSA filter has been applied to align the crystals with each other and to the ancillary device (in this case SPIDER). This procedure consent to reduce

random coincidences and accordingly to improve the time resolution in the timing spectra. A time matrix is built with the time differences between each combination of detectors. After getting the time position of all the pairs of time peaks, the optimal time shift for each detector is calculated by a dedicated code (*SolveTT* through a global χ^2 minimization procedure.

In the offline analysis, this procedure has been applied to all the measurement runs to avoid problems due to GTS system malfunctions. The result, for a run, is presented in figure 5.7. Here the improvement in the time resolution after the alignment can be appreciated.

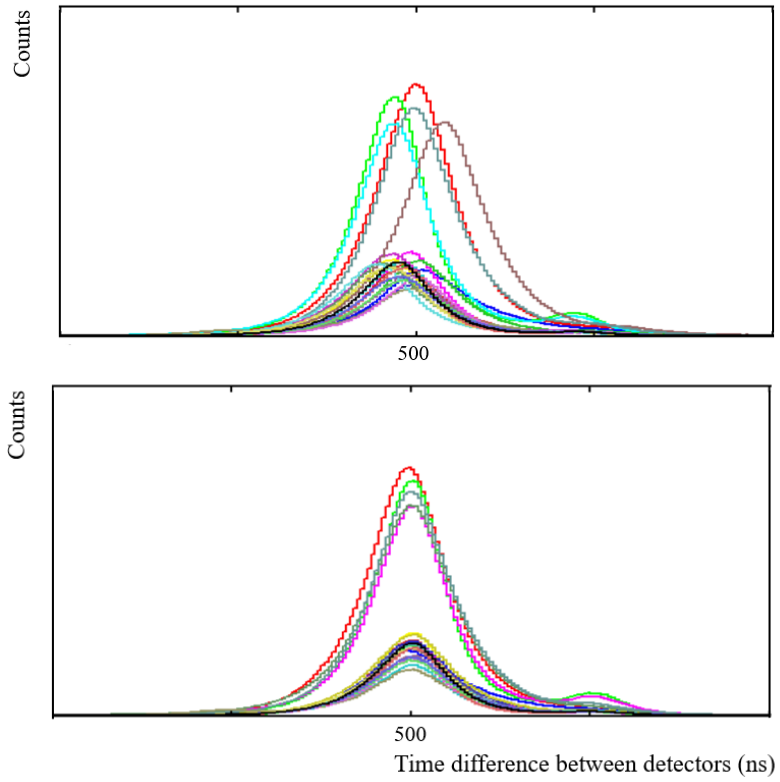

Figure 5.7: **PostPSA**: Overlap of the time difference spectra between the crystal 00C and all the other crystals before (top) and after (bottom) global time alignment for a measurement run.

5.1.2 Global-Level Processing

The Global level actors for a setup with complementary detectors are the *Event Builder*, the *Event Merger*, the *Tracking Filter* and the *Consumer*.

The *Event Builder* is in charge of assembling the signals from the AGATA crystals in events. Its output is then merged with the data from the ancillary detectors (in this case, SPIDER) by the *Event Merger*. These two operations are carried out by selecting signals within a window of timestamp difference to eliminate uncorrelated events. Both the time

coincidence windows used in this experiment for builder and merger cases are equal to 45 timestamp units (450 ns).

The *Tracking filter* performs the reconstruction of the γ–ray trajectories inside the AGATA array. The principles of γ–ray tracking were introduced in Chapter 4. Previous studies [44] proved how after the tracking algorithm the Compton background at low energies is significantly reduced, and the height of the peaks at high energies is increased. The resulting improvement of the peak-to-total ratio is about a factor $\sim$2 for the 1.3 MeV line from a ^{60}Co source. At the same energy, the use of the tracking algorithm leads to an increase in the efficiency of about $\sim$1.3. Figure 5.8 shows the first reconstructed interaction point for each event. The information on the first interaction position inside the AGATA sub-array is essential for the Doppler correction of the detected γ-ray energy.

In the end, the consumer *Tree Builder* stores all the obtained results in ROOT Trees.

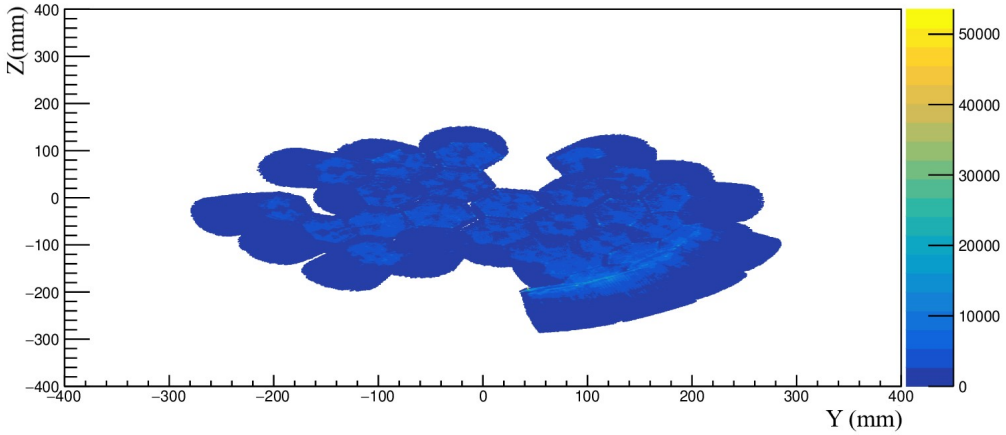

Figure 5.8: **Tracking**: First Interaction pattern. First interaction position of the gamma-rays inside the AGATA sub-array. The configuration of the 11 triple AGATA clusters (28 detectors) present in the setup of this experiment can be appreciated from the reaction chamber point of view. Axes in the AGATA laboratory frame.

5.1.3 Efficiency Measurement

The *photopeak absolute efficiency* for a γ–ray detector is defined as the ratio between the number of γ rays detected N_{meas} in the photopeak and those emitted by the source N_{emit}. The latter value is obtained considering the source activity at the time and date of the measurement, the duration of the measurement, the acquisition dead time, and the relative intensities of each γ transition.

Because of the chosen normalization method for the cross-section evaluation in this work (see section 2.4), the *photopeak relative efficiency* is sufficient, which is defined as the ratio between the number of γ rays N_{meas} and the relative intensities of each γ

transition I_γ:

$$\epsilon_\gamma(E_\gamma) = \frac{N_{meas}(E_\gamma)}{I_\gamma(E_\gamma)} \ . \tag{5.1}$$

The γ–ray sources ^{152}Eu and ^{226}Ra were employed to cover the energy range of interest for this work, which is from $\approx$ 100 keV to $\approx$ 2200 keV. The sources (one at a time) were placed at the centre of the reaction chamber with SPIDER installed and AGATA in the close-up position (the same configuration as in the measurement). From the acquired spectra, only the peaks whose relative intensities are known with high precision were considered.

The experimental data points were fitted with the RadWare function [45]:

$$\epsilon_\gamma = \exp\left\{ \left[(A + Bx + Cx^2)^{-G} + (E + Fx + Cx^2)^{-G} \right]^{-1/G} \right\} \tag{5.2}$$

where $x = \ln E_\gamma/100$, $y = \ln E_\gamma/1000$, E_γ is the γ–ray energy in keV, and $A - G$ are the fit parameters. In the present case, C and G were kept fixed at 0 and 15, respectively. The fitted efficiency curve is shown in figure 5.9, while the results of the fit procedure are reported in table (5.1).

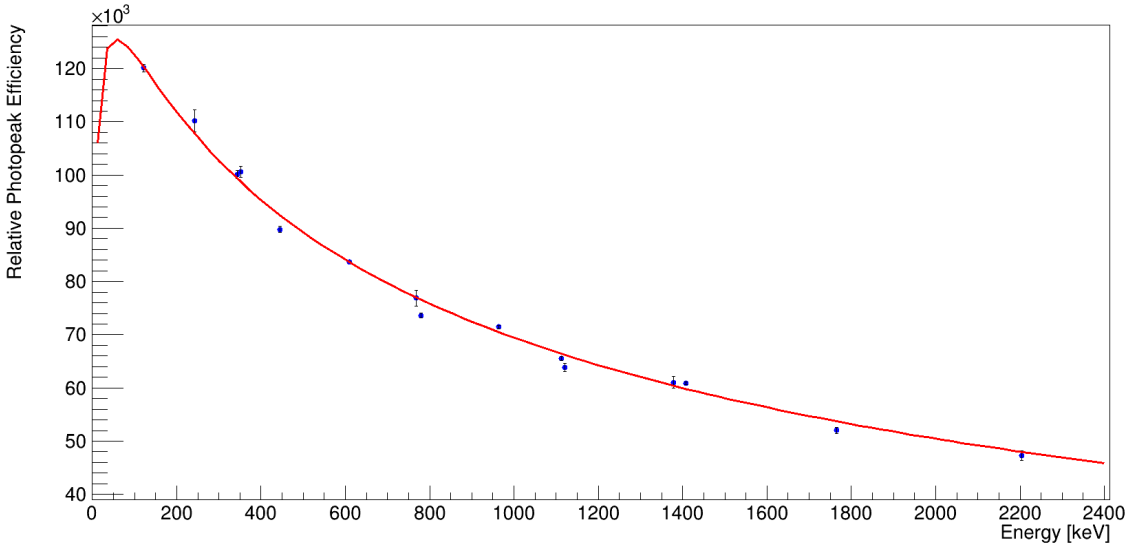

Figure 5.9: Photopeak relative efficiency for the configuration of AGATA used in this work as a function of the γ–ray energy. The measured efficiencies are reported in blue, while the fitted function is shown in red.

A	B	C	D	E	F	G
25(6)	2(3)	* 0	11.150(2)	−0.411(4)	−0.071(2)	* 15

Table 5.1: Fit results for the AGATA efficiency curve shown in figure 5.9. The parameters marked with * were kept fixed in the fit procedure.

5.2 SPIDER

The SPIDER *Look-Up Table* (LUT) is the input file of the AGATA sorting codes containing the information about the SPIDER array, and is shown in figure 5.10. The information contained in the table is experiment-dependent and has to be filled in following dedicated procedures.

The first two columns of the LUT identify the SPIDER boards and channels, respectively. These two values are related to the acquisition system as well as the mapping value, reported in the third column, which is an identifier used in the data frame. The fourth column contains the name of each strip according to a code that indicates the detector (from D1 to D7) and the strip (from S1 to S8). The fifth and sixth columns report, for each strip, the energy thresholds adopted to select the range associated with the back-scattered ^{58}Ni ions and reject the noise. These thresholds were chosen according to the individual SPIDER energy spectra. An example of a spectrum from a strip obtained in the experiment of this work is shown in figure 5.11. The seventh and eighth columns indicate the position of each strip in polar coordinates (θ, ϕ), following the same reference system of AGATA. The ninth column indicates the time-offset values. The time differences between AGATA and SPIDER are shown for each strip after the alignment procedure in figure 5.12. Proper offsets have been added to align all the coincidences to -100 timestamp units. The last

```
####### SPIDER ######
#
# the "map" number conversion into detector and strip:
# strip = (map % 10) + 1
# detector = (map / 10) + 1
#
```

Board	channel	map	name	thr_lo	thr_hi	theta	phi	TimeOffset	ncalpar	calpars	
4	0	66	D7S7	1.5	30	132.3	1.13	12	2	-0.0630677207461566	0.0021881181864141
4	1	67	D7S8	1.5	30	128	1.13	12	2	-0.0667568737174215	0.00218957289973084
4	2	64	D7S5	1.5	30	141.4	1.13	12.5	2	-0.0681702636218202	0.00216031515504544
4	3	65	D7S6	1.5	30	136.8	1.13	12	2	-0.0638052629475714	0.00213947774207694
4	4	62	D7S3	1.5	30	150.6	1.13	12.5	2	-0.0644772363376991	0.00221134551248514
4	5	63	D7S4	1.5	30	146	1.13	12.3	2	-0.0679594408517334	0.00220482709045325
4	6	60	D7S1	1.5	30	159.6	1.13	13	2	-0.0625936286672579	0.00217166091141576
4	7	61	D7S2	1.5	30	155.2	1.13	13	2	-0.0693976336426386	0.0021582741389443
3	0	6	D1S7	1.5	30	132.3	52.56	0.2	2	-0.0595462815414778	0.00211500620958866
3	1	7	D1S8	1.5	30	128	52.56	0	2	-0.0543842169235476	0.00213337859719813
3	2	4	D1S5	1.5	30	141.4	52.56	0	2	-0.0612684001898833	0.00210123803037496
3	3	5	D1S6	1.5	30	136.8	52.56	0.5	2	-0.0562804398530951	0.00209855374473801
3	4	2	D1S3	1.5	30	150.6	52.56	0.8	2	-0.0545233970988379	0.00219687684262444
3	5	3	D1S4	1.5	30	146	52.56	0.8	2	-0.0553656506487666	0.00217223271291602
3	6	0	D1S1	1.5	30	159.6	52.56	0.8	2	-0.0559869425471788	0.00219658618412492
3	7	1	D1S2	1.5	30	155.2	52.56	0.8	2	-0.0584591330935155	0.0021794257598638
3	8	16	D2S7	1.5	30	132.3	103.99	0.8	2	-0.057962213636396	0.00212168473541385
3	9	17	D2S8	1.5	30	128	103.99	0.5	2	-0.0576340230968868	0.00209668457757068
3	10	14	D2S5	1.5	30	141.4	103.99	1	2	-0.0593401509690769	0.00210769294981721
3	11	15	D2S6	1.5	30	136.8	103.99	1	2	-0.059448056440882	0.00213697420286739
3	12	12	D2S3	1.5	30	150.6	103.99	1	2	-0.0550393883410334	0.00210445855994722
3	13	13	D2S4	1.5	30	146	103.99	1	2	-0.0581602367107023	0.00219570702443988
3	14	10	D2S1	1.5	30	159.6	103.99	1	2	-0.0557182914427276	0.0021860821662496
3	15	11	D2S2	1.5	30	155.2	103.99	1	2	-0.0561587865071684	0.00214729127722091
1	0	26	D3S7	1.5	30	132.3	155.42	1	2	-0.0571327861242935	0.00213033542894861
1	1	27	D3S8	1.5	30	128	155.42	1	2	-0.0560542349798646	0.00219922787102376
1	2	24	D3S5	1.5	30	141.4	155.42	1.5	2	-0.0545659794714307	0.00219863729344104
1	3	25	D3S6	1.5	30	136.8	155.42	1.5	2	-0.0563708584360503	0.00221164040639906
1	4	22	D3S3	1.5	30	150.6	155.42	2.3	2	-0.0569662220114633	0.00212374184751397
1	5	23	D3S4	1.5	30	146	155.42	1.5	2	-0.0670220300260428	0.00222298720177183
1	6	20	D3S1	1.5	30	159.6	155.42	1.4	2	-0.0561210874404473	0.0022133071435465

Figure 5.10: SPIDER *Look-Up Table* (LUT) used in the present work. From left to right, the columns contain digitizer details [board, channel], strip unique identifiers [map, name], thresholds in MeV [min, max], physical position [θ, ϕ], time offset in timestamp, number of used energy-calibration coefficients, and energy-calibration coefficients.

three columns in the SPIDER LUT correspond to the number of parameters used for the energy calibration (2 in this case) and their values. These were determined as described in the following section.

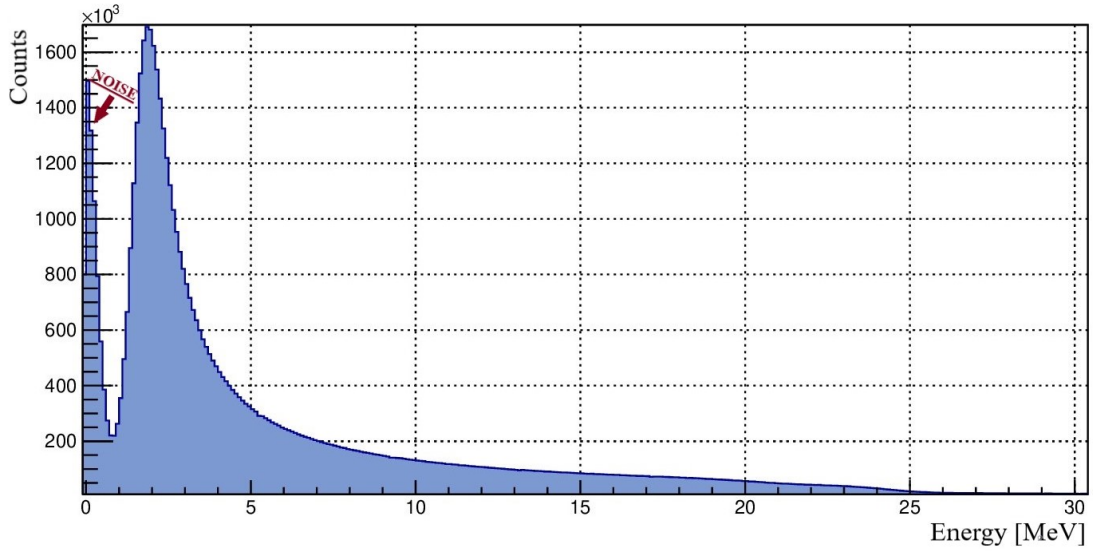

Figure 5.11: Energy spectrum of a SPIDER strip ($\theta = 158°$). The back-scattered projectiles and the noise contribution are visible.

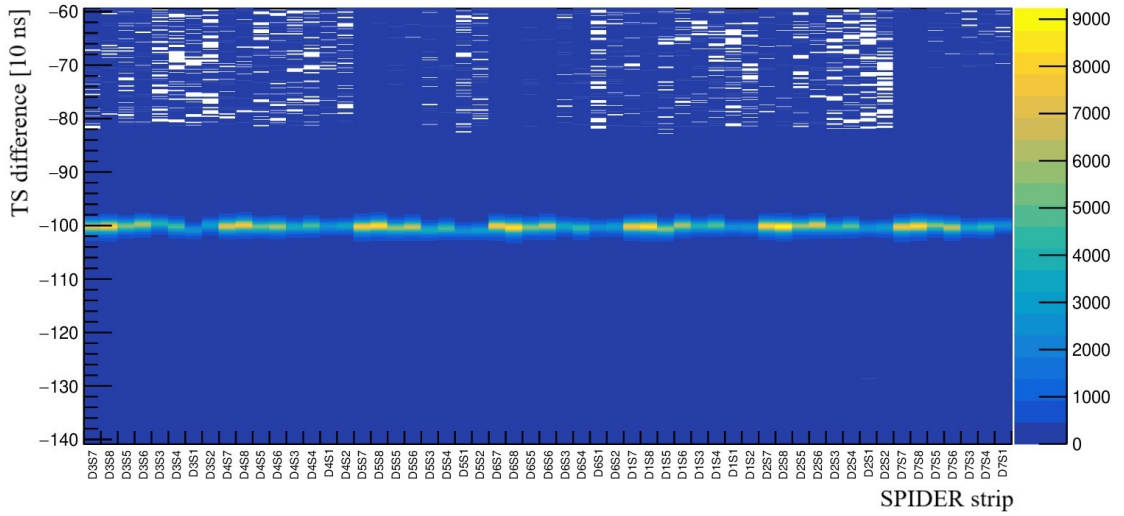

Figure 5.12: The time differences between AGATA and SPIDER for each SPIDER strip after the alignment procedure.

5.2.1 Energy Calibration

In the scattering of the ^{58}Ni beam with the ^{96}Zr target the back-scattered projectiles can reach energies up to 20 MeV. Since no standard source provides reference particles at such energies, the calibration was performed using an α-source, which emits three α-particles

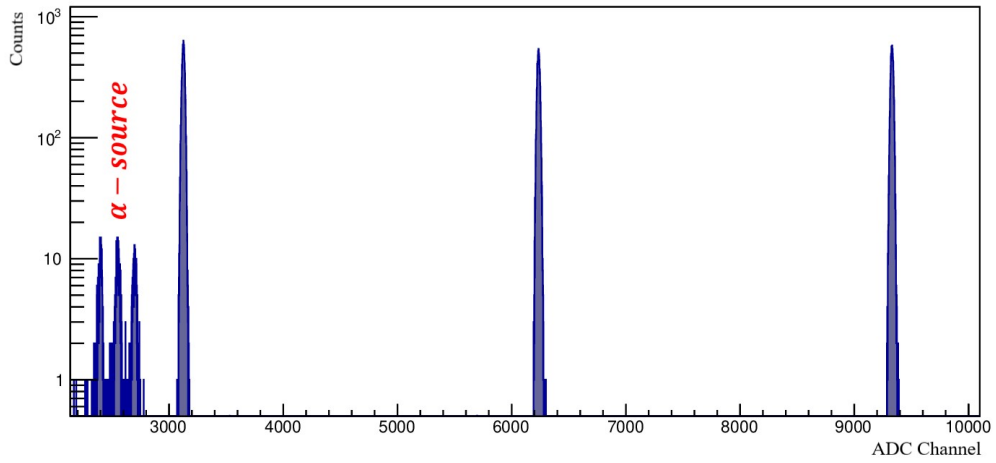

Figure 5.13: Energy-calibration spectrum of a SPIDER strip. The α-particles emitted by a triple alpha source $^{239}\mathrm{Pu} +^{241}\mathrm{Am} +^{244}\mathrm{Cm}$ have been detected together with a set of signals, equally spaced in amplitude, provided by a pulser.

at an energy around ≈ 5 MeV, and an extrapolation to higher energies with a pulse generator. The source, composed of the ^{239}Pu, ^{241}Am, and ^{244}Cm radionuclides, was placed at the target position inside the scattering chamber. A set of signals from a pulser, equally spaced in amplitude, was also fed to the SPIDER preamplifiers individually for each channel (*i.e.* each strip of each detector). The amplitude spacing between consecutive signals was 0.5 V and their minimum amplitude was set to 0.5 V. A calibration spectrum for a single strip of SPIDER is shown in figure 5.13.

To use the pulser peaks for the calibration, it is necessary to obtain the conversion between the signal amplitude in Volt and the channel number from a linear fit:

$$V_{pulser}(ch) = m \cdot ch_{pulser} + q \tag{5.3}$$

where ch is the channel number and m, q are the parameters fitted individually for each strip. The same equation can be applied to the alpha peaks to get the signal amplitude V_α from the channel number ch_α.

The next step in the calibration procedure is to convert the signal amplitude into energy. This can be achieved using an α peak as a normalization value (the central peak $E_\alpha = 5.486$ MeV was used). Hence, assuming $V \propto E$, it is possible to obtain:

$$\frac{V_\alpha}{V_{pulser}} = \frac{E_\alpha}{E_{pulser}} \rightarrow E_{pulser} = E_\alpha \frac{V_{pulser}}{V_\alpha} = E_\alpha \frac{m \cdot ch_{pulser} + q}{m \cdot ch_\alpha + q}\,. \tag{5.4}$$

This relation provides the conversion between the channel number and the energy of the pulser signal. For each strip, the calibration coefficients have been extracted and inserted in the SPIDER LUT.

5.3 AGATA + SPIDER

The last step of the analysis procedure consists of selecting of the coincidences between AGATA and SPIDER. This part is handled by a dedicated Root [41] selector (Ref. [46]) that allows for high-level analyzed data and the generation of histograms for each detector and coincidences between different detectors. The input file of the code contains all the information about the experiment, such as the description of the employed arrays, the reaction mechanism, the characteristics of the target, and the time gate for the coincidences.

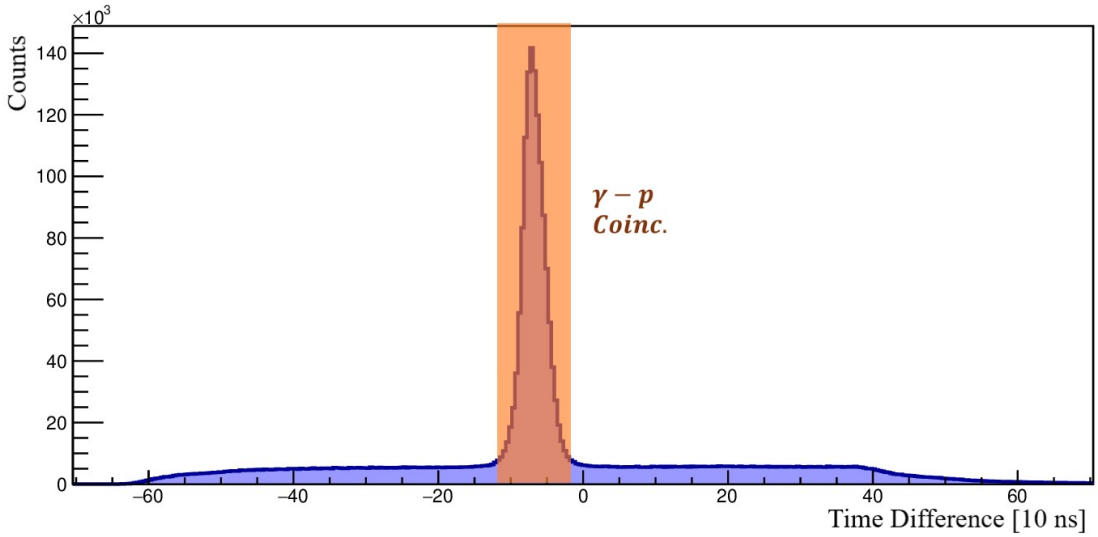

Figure 5.14: Time-difference spectrum of γ–particle coincidences. The gate used for the Coulomb-excitation coincidences is highlighted in orange.

In the selector, the γ–particle coincidences are selected by merging the data from AGATA and SPIDER with a 90-ns time window (see figure 5.14). The final γ–ray energy spectra obtained from the coincidence measurement are reported in panel (a) of figure 5.15. As already mentioned in section 2.3, the de-excitation γ rays are typically emitted in flight, therefore their energy has to be Doppler corrected according to equation (2.31). The spectrum in panel (b) of figure 5.15 is Doppler corrected for the projectile nuclei (^{58}Ni), while in panel (c) for the target nuclei. The direction and the energy of the recoiling target nuclei were reconstructed from the kinematics by using the impact position and energy of the recoiling ^{58}Ni ions detected with SPIDER.

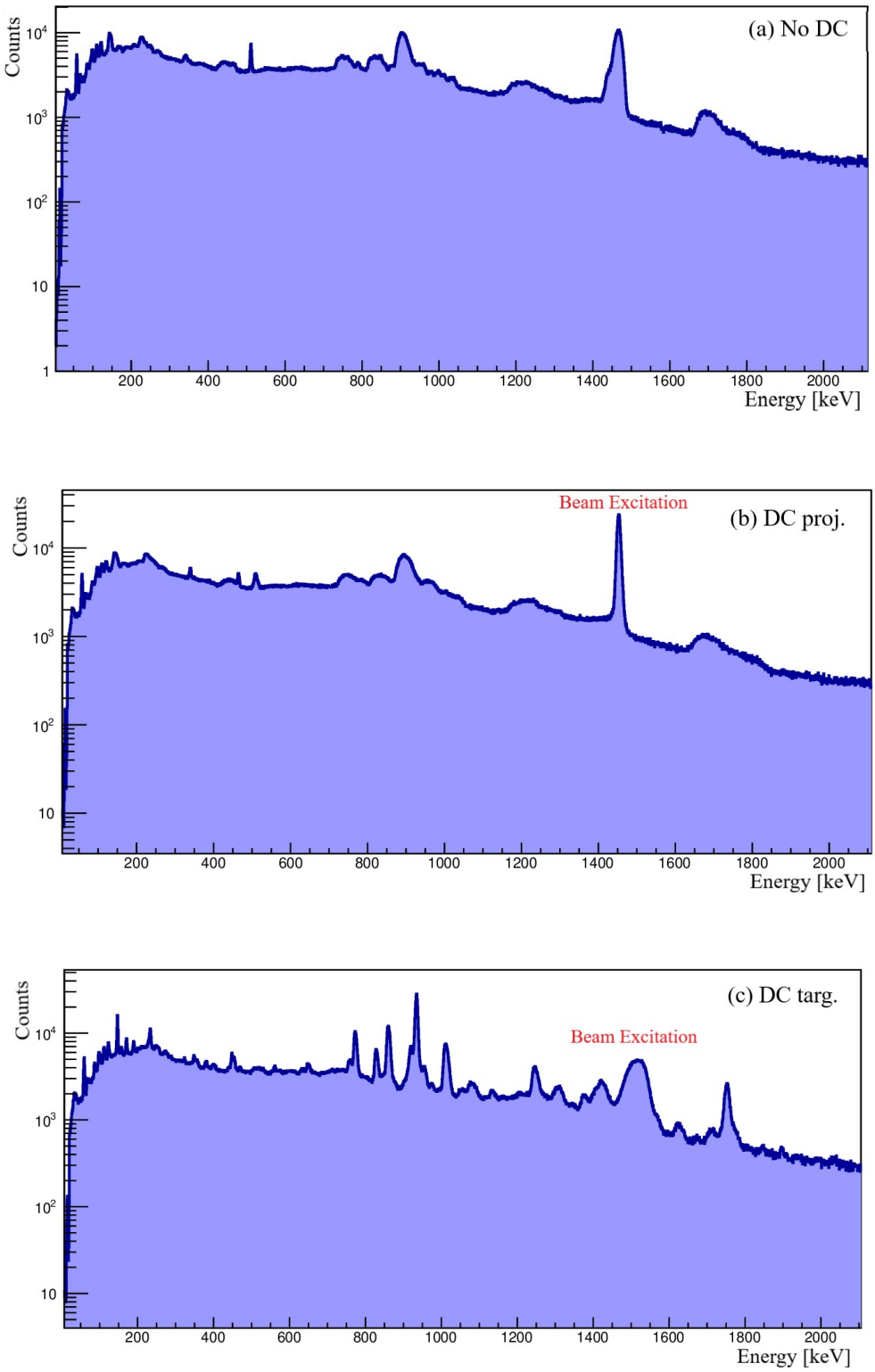

Figure 5.15: γ–ray energy spectra acquired in coincidence with the back-scattered ^{58}Ni ions. In the upper panel (a) no Doppler correction has been applied. In the middle panel (b) the Doppler correction has been applied for the projectile nuclei, while in the lower panel (c) for the target nuclei.

In the spectra, excitation lines from other Zr isotopes ($A = 90, 92, 94$) present in the target are visible. The presence of ^{16}O layers on the target surfaces has been discussed in section 3. The γ–ray transitions corresponding to the γ decay of the ^{72}Br, ^{72}Se, and ^{69}As excited nuclei, visible in the energy range from $\approx$ 300 keV to $\approx$ 1300 keV are the result of the fusion-evaporation reaction $^{58}\mathrm{Ni} + ^{16}\mathrm{O}$ at 160 MeV. The cross sections of the reaction were calculated with the PACE4 code [47], and indeed the (^{72}Br, pn), (^{72}Se, $2p$) and (^{69}As, $3p2n$) reactions resulted to be the most probable evaporation channels.

5.3.1 Excitation-Energy Selection

The total excitation energy of the ^{58}Ni + ^{96}Zr system can be used to minimize the contribution of the fusion-evaporation reactions in the γ–particle spectra. The matrices in figures 5.16 and 5.17 show the γ–ray energy as a function of the total excitation energy calculated from the SPIDER energy spectra and reconstructing the kinematics, *i.e.* by considering energy and momentum conservation and exploiting the knowledge of the target, the beam, and the angles (θ, ϕ) of the backscattered ions from SPIDER. By setting proper energy gates on the matrices in figures 5.16 and 5.17, it is possible to disentangle the contribution of Coulomb excitation from that of fusion-evaporation.

Figures 5.18 and 5.19 show the excitation energy spectra corresponding to gates on the γ–ray energy at 1454 keV and 1750 keV, with a 15-keV width of the gates. These energies refer to the first excited 2^+ state in ^{58}Ni and ^{96}Zr, respectively. An approximately symmetrical distribution around the zero excitation energy is obtained in both cases, representing the elastic scattering of ^{58}Ni on ^{96}Zr. The width of the distributions originated from the target thickness and, indeed, resembles that in figure 3.6. The distributions extend at un-

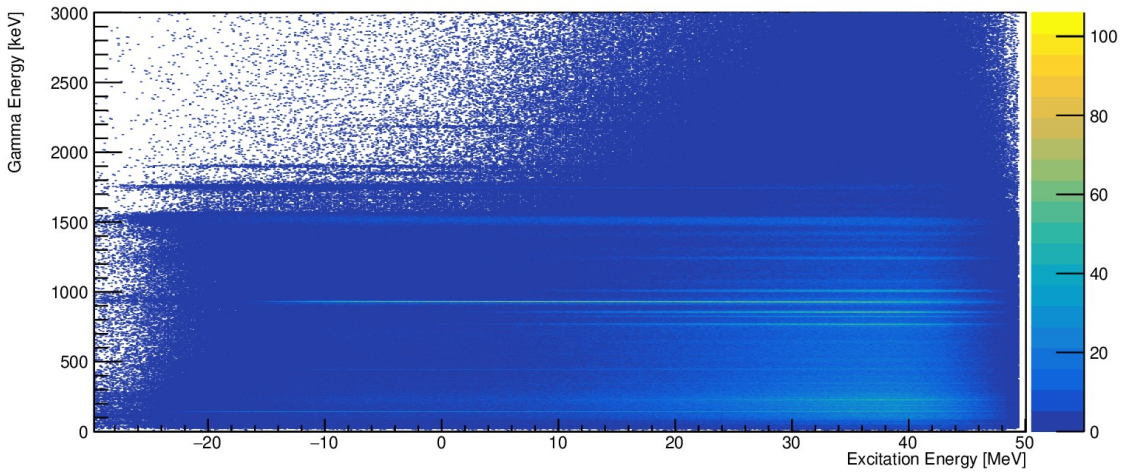

Figure 5.16: γ–ray energy, Doppler-corrected for the back-scattered beam, as a function of the total excitation energy of the ^{58}Ni + ^{96}Zr system.

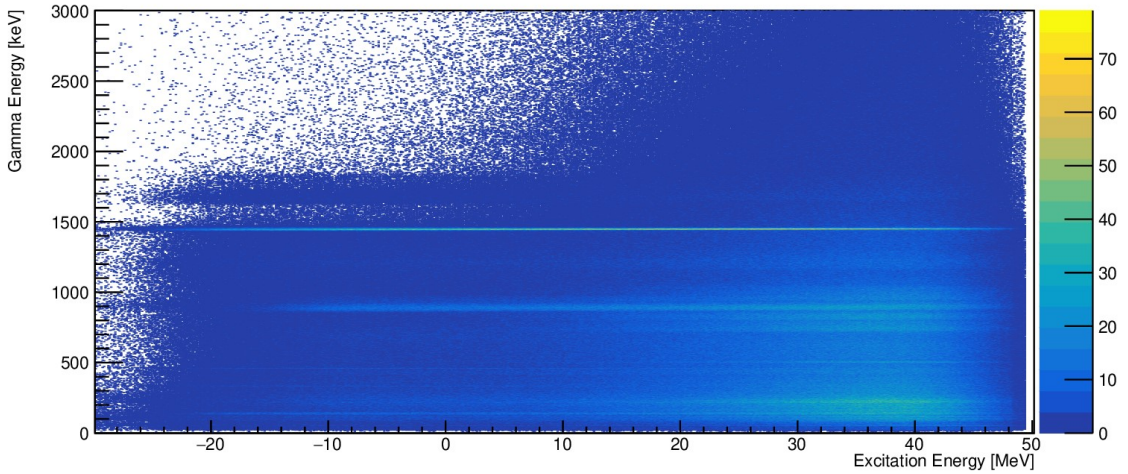

Figure 5.17: γ–ray energy, Doppler-corrected for the target nuclei, as a function of the total excitation energy of the ^{58}Ni + ^{96}Zr system.

physical negative energies becasue of the approximations in the kinematic reconstruction. For example, the straggling of the beam in the target is not considered, and the calculation of the energy loss in the target is assuming that the reaction always takes place at the centre of the target. Also, the finite size of the SPIDER strips is not taken into account. Figure 5.20 shows the distribution obtained setting the gate on the 622-keV γ transition from ^{69}As. The shape in this case is different and reflects a fusion-evaporation spectrum. It should be noted that the kinematic reconstruction is always performed assuming the Coulomb-excitation scattering and, therefore, the shape of the fusion-evaporation spectrum in figure 5.20 does not have a physical meaning. Nevertheless, its shape is different from the case of elastic scattering of ^{58}Ni on ^{96}Zr (figures 5.18 and 5.19) allowing for the identification of the reaction mechanism producing the γ rays.

From figures 5.18, 5.19, and 5.20 it is visible how by selecting the excitation energy it is possible to minimize the contribution from the fusion-evaporation. A gate on the x-axis was set on the matrix in figure 5.17, and the γ–energy spectrum was produced by projecting the onto the y-axis. Figure 5.21 shows the γ–ray energy spectrum obtained by setting a gate from 14 MeV to 50 MeV. The presence of a strong fusion-evaporation component is evident. Figure 5.22 shows the γ–ray energy spectrum obtained by setting a gate from -30 MeV to 6 MeV on the excitation energy. The γ transitions from the ^{96}Zr excitation are clearly visible and, therefore, this spectrum was used for the Coulomb-excitation analysis.

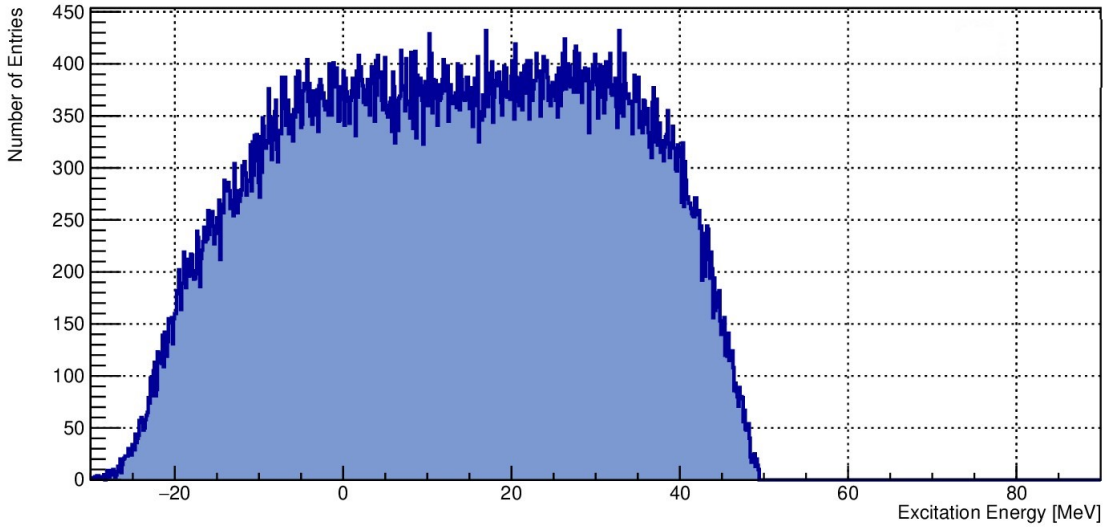

Figure 5.18: Projection of the matrix in figure 5.17 on the x-axis, obtained with a gate on the y-axis on the 1454-keV transition in ^{58}Ni.

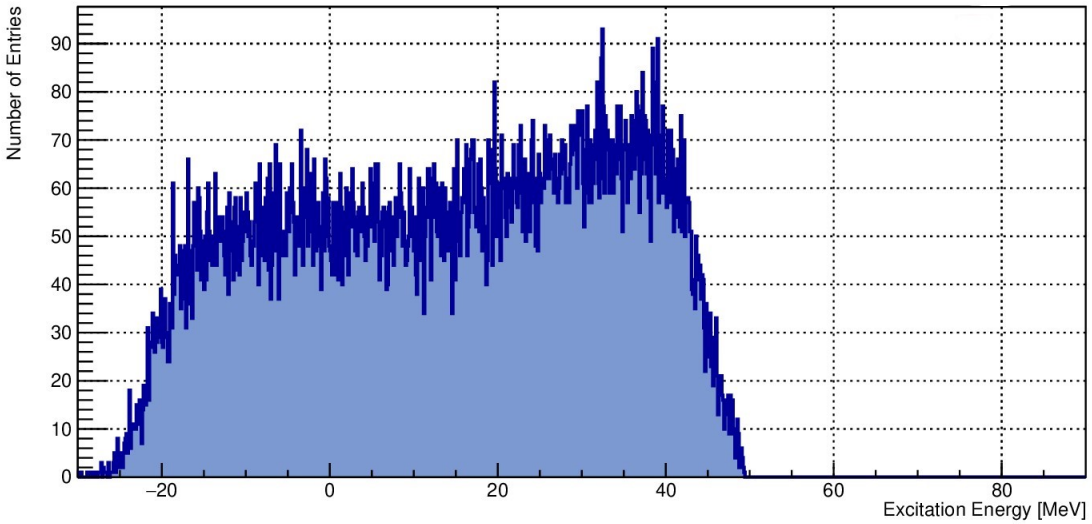

Figure 5.19: Projection of the matrix in figure 5.17 on the x-axis, obtained with a gate on the y-axis on the 1750-keV transition in ^{96}Zr.

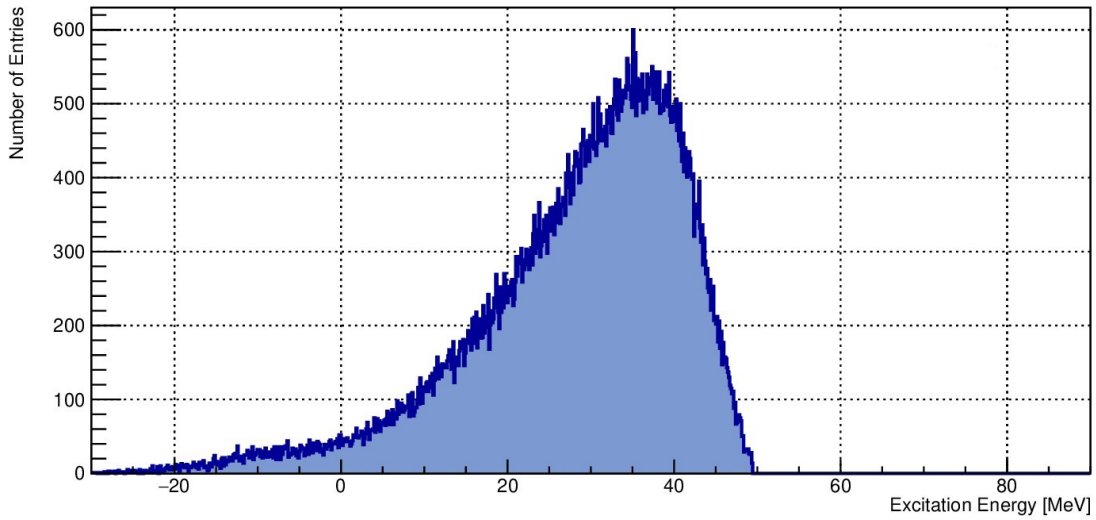

Figure 5.20: Projection of the matrix in figure 5.17 on the x-axis, obtained with a gate on the y-axis on the 662-keV transition in ^{69}As (originating from the $(^{69}\mathrm{As},\ 3p2n)$ fusion-evaporation reaction).

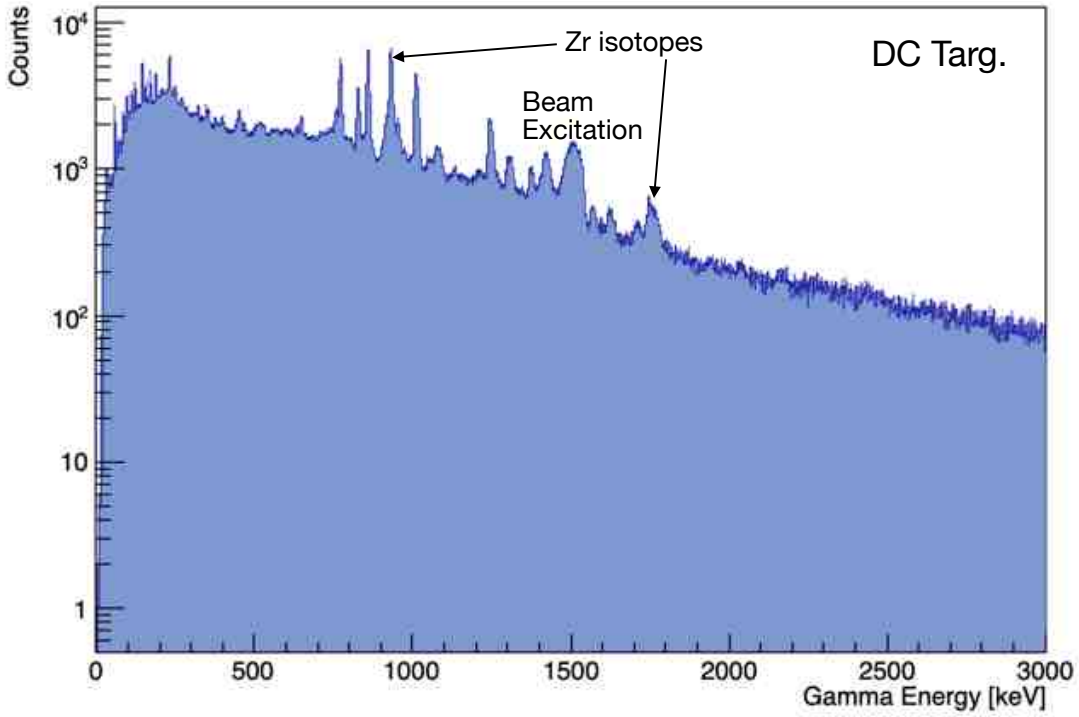

Figure 5.21: Projection of the matrix in figure 5.17 on the y-axis, obtained with a gate on the x-axis from 14 MeV to 50 MeV.

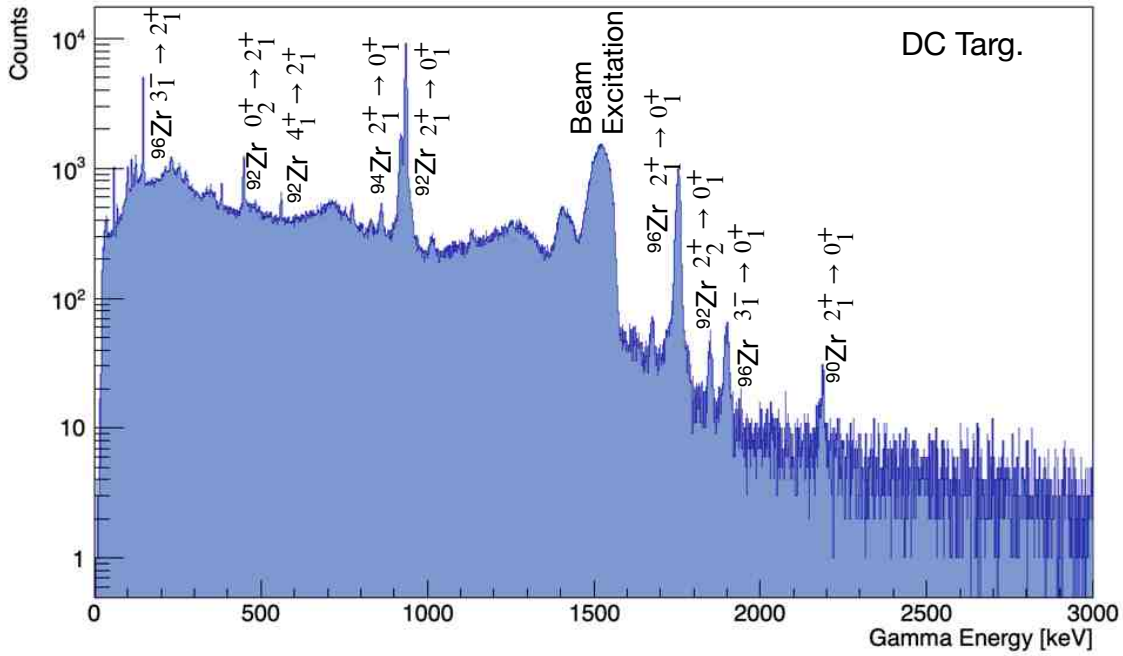

Figure 5.22: Projection of the matrix in figure 5.17 on the y-axis, obtained with a gate on the x-axis from -30 MeV to 6 MeV.

Chapter 6

Coulomb-Excitation Analysis

This chapter describes the Coulomb-excitation analysis performed using the GOSIA code, reports the extracted $B(E1; 3_1^- \rightarrow 2_1^+)$ and $B(E3; 3_1^- \rightarrow 0_1^+)$ values, and discusses the results.

6.1 Setting the GOSIA Input File

The final γ–ray energy spectrum obtained from AGATA in coincidence with the back-scattered ^{58}Ni ions detected by SPIDER, Doppler corrected for the ^{96}Zr target, is shown in the upper part of figure 6.1. The energy peaks of the ^{96}Zr transitions are labelled in

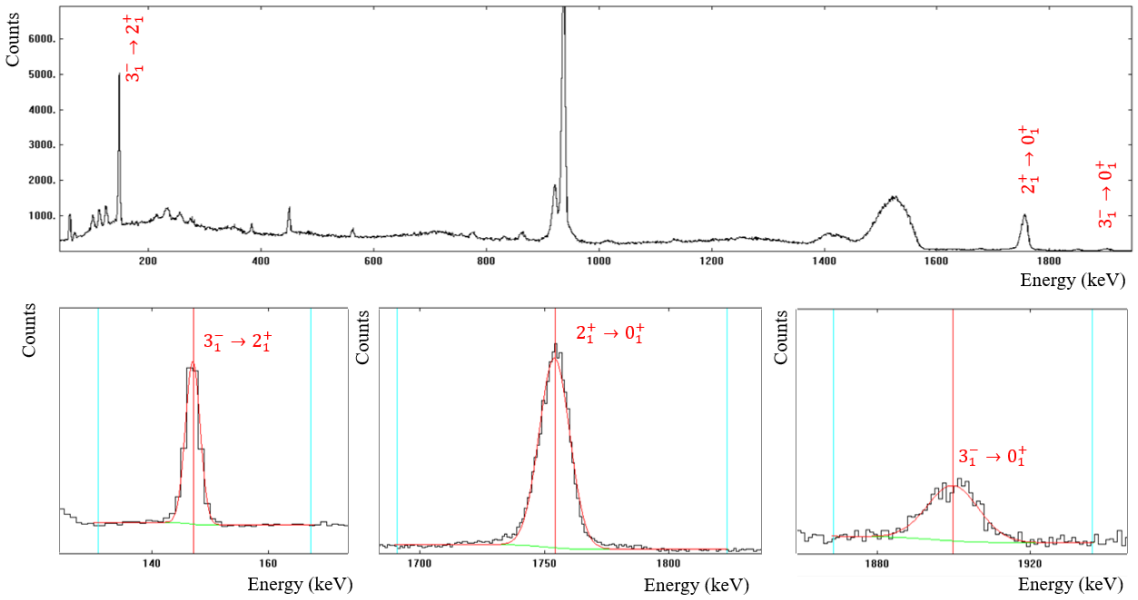

Figure 6.1: (Top) γ–ray energy spectrum obtained from AGATA in coincidence with the back-scattered ^{58}Ni ions detected by SPIDER, Doppler corrected for the ^{96}Zr target. (Bottom) zoom of the spectrum on the top in specific energy regions and Gaussian fit of the transitions of interest.

Transition	Multipolarity	Energy (keV)	Counts
$2_1^+ \rightarrow 0_1^+$	$E2$	1750	14480(190)
$3_1^- \rightarrow 2_1^+$	$E1$	147	13900(200)
$3_1^- \rightarrow 0_1^+$	$E3$	1897	830(60)

Table 6.1: ^{96}Zr transitions observed in the present work (see figure 6.1) and observed number of counts for each transition.

the figure and summarized in table 6.1. Figure 6.1 also shows peaks originating from the target contaminants and a structure around 1500 keV corresponding to the Doppler-broadened $2_1^+ \rightarrow 0_1^+$ transition in the ^{58}Ni projectile nuclei.

The experimental Coulomb-excitation yields were extracted from the spectrum in figure 6.1 by performing a Gaussian fit for each peak reported in table 6.1, and the results are reported in the same table. The TkT software was used to fit the peaks. The extracted yields were corrected for the finite size of the AGATA HPGe detectors, which was included in the GOSIA input file to take into account the γ-energy dependence on the solid-angle attenuation factors.

The level scheme assumed in the GOSIA analysis is shown in figure 6.2. To correctly describe the excitation and de-excitation processes, it was necessary to add the so-called *buffer states* above the populated ones. These states are defined in GOSIA analysis to ensure that the virtual excitation of unobserved states is properly taken into account. In the present analysis, two buffer states were added from the konwn level scheme of ^{96}Zr: the 4_1^+ state at 2857 keV and the 5_1^- state at 3120 keV.
The contribution of unobserved decay via internal conversion was taken into account by providing internal conversion coefficients in the GOSIA input file for the relevant multipolarities (*i.e.*, $E1$, $E2$, and $E3$) and the energy range of interest (*i.e.*, $\approx$ 100 - 2000 keV). The values for the internal conversion coefficients were taken from the BrICC database [48].

The lifetimes obtained in previous experiments were also included in the analysis by declaring them in the GOSIA input file, together with their uncertainties. These values, reported in table 6.2, were used as additional data points, entering the minimization procedure on an equal basis with the γ–ray yields observed in the present Coulomb-excitation experiment. The lifetime of the 3_1^- state was not included in the analysis because it would bias the extracted $B(E3; 3_1^- \rightarrow 0_1^+)$ value, the goal of the present analysis.

The position of each capsule of AGATA was declared in the GOSIA input file by defining their polar and azimuthal angles. SPIDER was considered a symmetric detector in the azimuthal direction, and described by defying a set of mesh points in the θ angle to cover its polar-angular range. GOSIA then calculated the shape of SPIDER from these mesh points, and the cross-section was integrated over it. The cross-section also needs to be integrated over the finite thickness of the target, taking into account the energy loss

State	τ (ps)	$\Delta\tau$ (ps)
2_1^+	0.82	0.10
4_1^+	0.86	0.66
5_1^-	0.84	0.98

Table 6.2: Lifetimes assumed in the present analysis. The values were taken from the ENSDF database [1].

of the beam into it. This was done similarly to the description of the SPIDER geometry by defying a set of mesh points for different beam energies covering the range between the initial beam energy and that at the target's exit in the case of no scattering. For each mesh point, stopping powers calculated using the SRIM software [49] were provided in the GOSIA input file.

6.2 GOSIA Analysis

The lifetime of the 2_1^+ state in ^{96}Zr is known with good precision ($\tau = 0.82(10)$ ps [1]). For this reason, this value was used to normalize the experimental yields (see section 2.4 for more details about the normalization procedures in GOSIA analysis). This choice avoids using experimental information such as the beam current, the duration of the experiment, and the errors related to these quantities. On the other hand, this choice for the normalization means a bias in the $\langle 2_1^+ || E2 || 0_1^+ \rangle$ matrix element. Hence, the $B(E2; 2_1^+ \rightarrow 0_1^+)$

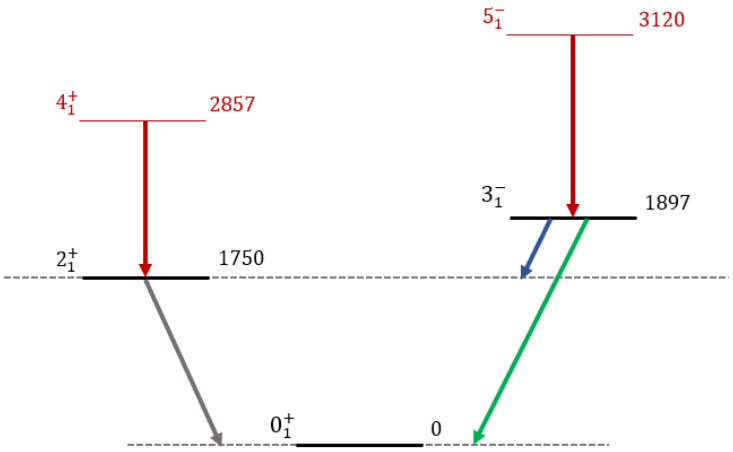

Figure 6.2: ^{96}Zr level scheme used in the GOSIA analysis. The levels related to the observed transitions are shown in black. The $E2$ $2_1^+ \rightarrow 0_1^+$ transition is shown in grey, the $E3$ $3_1^- \rightarrow 0_1^+$ transition in green, and the $E1$ $3_1^- \rightarrow 2_1^+$ transition in blue. The buffer states 4_1^+ and 5_1^- and their de-exciting transitions are marked in red.

value resulting from the present GOSIA analysis cannot be considered an outcome.

The results of the target analysis reported in chapter 3 were used in the GOSIA analysis. The RBS measurement performed at LABEC showed how the oxygen is present in the surfaces of the target and absent in the middle. This is the typical situation when the oxidation of the target happens, caused by exposition to air and by the manufacturing process. Nevertheless, because oxygen is always found together with zirconium in oxidized materials, its presence can be ignored in the GOSIA analysis. Indeed, when the beam scatters on oxygen it proceeds at forward angles, being the heavier partner, and, therefore, it is not detected in SPIDER. The event is, therefore, lost and neglected. If a thick layer of oxygen was instead present on the target surface, the beam energy would have been reduced at the entrance of the ^{96}Zr target, and this effect should have been taken into account. For the ^{96}Zr target thickness, the value 690(60) μg/cm^2 extracted in chapter 3 was used.

The efficiency of AGATA determined as described in section 5.1.3 was included in the GOSIA analysis to calculate the experimental yields. In the present analysis, the efficiency was assumed to be the same for each AGATA HPGe detector, and calculated by scaling that of the total array by the number of detectors.

In addition to the matrix elements of the transitions shown in figure 6.1, the $E2$ diagonal matrix element $\langle 2_1^+||E2||2_1^+\rangle$ related to the spectroscopic quadrupole moment[1] $Q_s(2_1^+)$ was included in the analysis. The present experiment is not expected to have sensitivity to this electromagnetic matrix element, for which at least the $4_1^+ \rightarrow 2_1^+$ transition should have been observed, but the inclusion in the analysis is necessary to properly take into account virtual two-step excitations via the 2_1^+ state.

The GOSIA analysis was performed starting from the initial values for the considered set of matrix elements deduced from known values in the literature, reported in table 6.3. For the $\langle 2_1^+||E2||2_1^+\rangle$ matrix element, unknown in ^{96}Zr, the value measured in a recent experiment in the close ^{94}Zr [50] was assumed as a starting value. For the $\langle 3_1^-||E3||0_1^+\rangle$ matrix element, the analysis was repeated with both the two discrepant values known in the literature [18, 19] as the starting values.

The results from the GOSIA fit are reported in table 6.3. The uncertainties reported in the table refer to the 68.3% confidence limit. The $\langle 2_1^+||E2||0_1^+\rangle$, $\langle 4_1^+||E2||2_1^+\rangle$ and $\langle 5_1^-||E2||3_1^-\rangle$ matrix elements were constrained from the assumed lifetimes, and (as already pointed out) the $\langle 2_1^+||E2||0_1^+\rangle$ matrix element was used to normalize the experimental yields. Hence, these values cannot be considered outcomes of the present analysis. The $\langle 2_1^+||E2||2_1^+\rangle$ matrix element resulted to be larger than what was assumed as the

[1]The quadrupole moment of a nuclear state J indicates the deviation of the nuclear charge distribution from sphericity and it is, therefore, related to the shape of the state. The spectroscopic quadrupole moment $Q_s(J)$ is the quadrupole moment measured in the laboratory frame and is proportional to the $\langle J||E2||J\rangle$ matrix element that is (in principle) observable in Coulomb excitation [23].

Matrix Element	Initial Value	Analysis Result
$\langle 3_1^- \|\| E1 \|\| 2_1^+ \rangle$	0.011 eb$^{1/2}$ [1]	0.0104(6) eb$^{1/2}$
$\langle 2_1^+ \|\| E2 \|\| 0_1^+ \rangle$	0.173 eb [1]	* 0.174(4) eb
$\langle 2_1^+ \|\| E2 \|\| 2_1^+ \rangle$	0.130 eb [50]	* 0.32(3) eb
$\langle 4_1^+ \|\| E2 \|\| 2_1^+ \rangle$	0.613 eb [1]	* 0.72(12) eb
$\langle 5_1^- \|\| E2 \|\| 3_1^- \rangle$	0.634 eb [1]	* 0.62(11) eb
$\langle 3_1^- \|\| E3 \|\| 0_1^+ \rangle$	0.467 eb$^{3/2}$ [18]	0.398(14) eb$^{3/2}$
	0.401 eb$^{3/2}$ [19]	

Table 6.3: Initial values for the matrix elements considered in the present analysis and results of the GOSIA minimization procedure. The matrix elements marked with * cannot be considered as outputs of the present work (see the text for the explanation). Two initial values were considered for the $\langle 3_1^- || E3 || 0_1^+ \rangle$ matrix element, which both gave the same experimental result.

initial value but is still a reasonable value for a mid-mass nucleus as ^{96}Zr. Nevertheless, this matrix element cannot be considered an outcome of the present work as previously explained and could include unobserved contributions from virtual excitations to higher-lying states. The two matrix elements free to vary in the GOSIA minimization and constrained only by the experimental results of the present experiment were the $\langle 3_1^- || E1 || 2_1^+ \rangle$ and $\langle 3_1^- || E3 || 0_1^+ \rangle$ ones. The most striking result of the GOSIA analysis is the obtained $\langle 3_1^- || E3 || 0_1^+ \rangle$ matrix element:

$$\langle 3_1^- || E3 || 0_1^+ \rangle = 0.398(14)\ e\mathrm{b}^{3/2}\,.$$

This value resulted in being the same in both analyses when assuming the two discrepant values known in the literature [18, 19] as the starting value.

6.3 Discussion of the Results

The present experiment provided the first direct extraction of the $\langle 3_1^- || E3 || 0_1^+ \rangle$ matrix element in ^{96}Zr, previously only indirectly deduced from measured lifetimes and branching ratios. The inconvenience of the previous estimations is that possible discrepancies in the results could be ascribed to both an incorrect lifetime of the 3_1^- state and/or an incorrect $3_1^- \rightarrow 2_1^+ / 3_1^- \rightarrow 0_1^+$ branching ratio.

To compare the present results with the previous measurements, the γ–ray $3_1^- \rightarrow 0_1^+ / 3_1^- \rightarrow 2_1^+$ branching ratio and the lifetime of the 3_1^- state have been calculated from the extracted matrix elements. Using equation 2.8, the γ–ray $3_1^- \rightarrow 0_1^+ / 3_1^- \rightarrow 2_1^+$ branching ratio can be calculated as

$$BR\left(\frac{E3; 3_1^- \rightarrow 0_1^+}{E1; 3_1^- \rightarrow 2_1^+}\right) \equiv \frac{\lambda(E3; 3_1^- \rightarrow 0_1^+)}{\lambda(E1; 3_1^- \rightarrow 2_1^+)} = 15(2)\%,$$

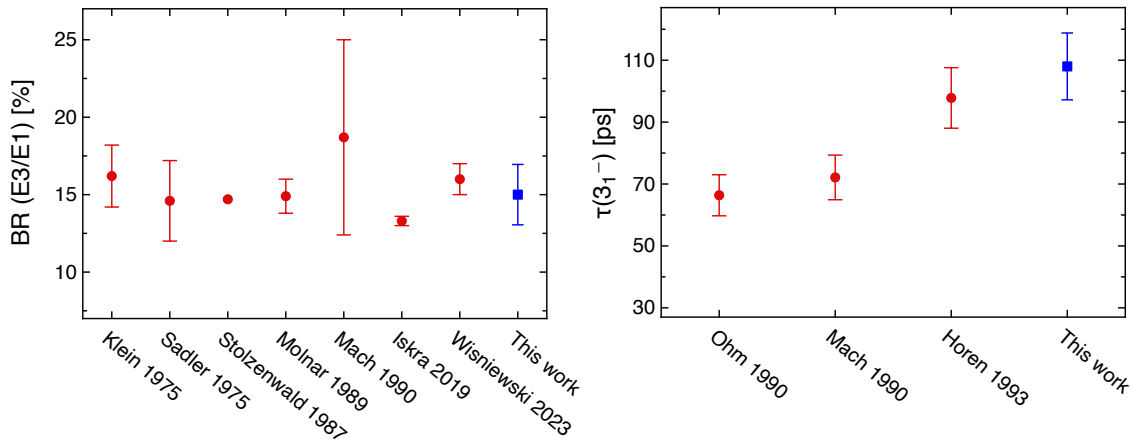

Figure 6.3: (Left, in red and circled dots) Measured γ–ray $3_1^- \to 0_1^+/3_1^- \to 2_1^+$ branching ratio in ^{96}Zr from Refs [53, 54, 55, 51, 56, 19]. The value marked Iskra 2019 has been corrected to esclude the total electron conversion contribution to the 147 keV transitions, and obtain the pure γ branching.(Right, in red and circled dots) Measured lifetime of the 3_1^- state in ^{96}Zr from Refs [52, 57, 56, 21]. (Left and right, in blue and squared dots) Values calculated from the matrix elements extracted in the present work.

To evaluate the lifetime of the 3_1^- state also the internal electron conversion branch of the 146.6 keV $E1$ transition has to be taken into account. The total $E1$ transition probability is then $\lambda_{tot}(E1; 3_1^- \to 2_1^+) = \lambda(1 + \alpha_{E1}(147\ \mathrm{keV}))$, where $\alpha_{\sigma L}$ is the internal conversion coefficient. The value of the internal conversion coefficient $\alpha_{E1}(147\ \mathrm{keV}) = 0.0376(6)$ from the BrICC database [48] has been used. The internal electron conversion branch of the 1897 keV $E3$ transition ($\alpha_{E3}(1897\ \mathrm{keV}) = 0.000440(6)$) is negligible.

$$\tau(3_1^-) \equiv \frac{1}{\sum_f \lambda(\sigma L; 3_1^- \to J_f)} = \frac{1}{\lambda_{tot}(E1; 3_1^- \to 2_1^+) + \lambda(E3; 3_1^- \to 0_1^+)} = 108(10)\ \mathrm{ps}.$$

The calculated quantities are compared with the previous measurements in figure 6.3. The new branching ratio is in agreement with all the previous measurements, including the newest one [19]. The value from Ref. [51] was used in the literature review of Ref. [18] (compiled before the work of Ref. [19]) because of the highest precision. Regarding the newly calculated $\tau(3_1^-)$ value, this agrees with its most recent direct measurement [21] and disagrees with all the previous measurements, except for the oldest one [52], which, however, has a large uncertainty.

The $E1$ and $E3$ electromagnetic matrix elements extracted in the present work have been used to calculate the $B(E1; 3_1^- \to 2_1^+)$ and $B(E3; 3_1^- \to 0_1^+)$ reduced transition probabilities. Using equation 2.9 and remembering that 100 fm^2 = 1 b, the transition probabilities of interest are

$$B(E1; 3_1^- \to 2_1^+) = \frac{1}{7}|\langle 3_1^- || E1 || 2_1^+ \rangle|^2 = 114(13) \cdot 10^{-4}\ \mathrm{W.u.}$$

and

$$B(E3; 3_1^- \rightarrow 0_1^+) = \frac{1}{7}|\langle 3_1^- || E3 || 0_1^+ \rangle|^2 = 41(3) \text{ W.u.}$$

The obtained $B(E3; 3_1^- \rightarrow 0_1^+)$ value is in excellent agreement with the one determined in Ref. [19], $B(E3; 3_1^- \rightarrow 0_1^+) = 42(3)$ W.u., which was obtained from a newly measured γ–ray $3_1^- \rightarrow 0_1^+ / 3_1^- \rightarrow 2_1^+$ branching ratio and the adopted and most precise value for the lifetime of the 3_1^- state reported in Ref. [21].

The matrix elements extracted in this work are in agreement with the most recent measurements of the $3_1^- \rightarrow 0_1^+ / 3_1^- \rightarrow 2_1^+$ branching ratio and the lifetime of the 3_1^- state. The results confirm the recent results of the indirect determination of the $B(E3; 3_1^- \rightarrow 0_1^+)$ value in ^{96}Zr from Ref. [19].

Conclusions

This thesis described the first low-energy Coulomb-excitation data analysis with the γ–ray tracking spectrometer AGATA coupled with the heavy-ion detector array SPIDER. The experiment subject of this work is one of the first experiments with AGATA in its second campaign at the INFN Legnaro National Laboratories, and it was performed by employing a 160-MeV energy beam of ^{58}Ni, delivered by the TANDEM accelerator, impinging on a ^{96}Zr target. The γ–rays de-exciting Coulomb-excited states of the target and beam nuclei were detected with AGATA in coincidence with the back-scattered ^{58}Ni nuclei detected with SPIDER.

The suite of codes developed for AGATA and SPIDER were used to perform the analysis, and fully tested for the first time. The analysis started with the energy calibrations, using radioactive sources, and the pre-sorting of the AGATA data coupled with SPIDER. The pulse shape analysis and tracking algorithms reconstruction were applied to increase the efficiency and the peak-to-total ratio of the the final coincidence γ–ray spectra. The Doppler correction of the γ rays emitted in flight was performed event by event considering the back-scattered ions measured with SPIDER, the kinematic reconstruction for the binary partner, and the first interaction hit of every reconstructed γ ray from the tracking algorithm.

The yields extracted from the final γ–ray energy spectrum, in conjunction with previously measured spectroscopic data, were used in the least-squares search code GOSIA. To study the target characteristics, which are needed as inputs in the GOSIA analysis, a dedicated Rutherford backscattering spectroscopy experiment was performed at the INFN LABEC laboratory.

The present work provides the first direct extraction of the $\langle 3_1^- || E3 || 0_1^+ \rangle$ matrix element in ^{96}Zr, previously only indirectly deduced from measured lifetimes and branching ratios. The obtained $B(E3; 3_1^- \rightarrow 0_1^+) = 41(3)$ W.u. value shows how this quantity, widely debated in the literature, is not as large as previously thought. Therefore, it does not represent a puzzling, outstanding value in the nuclide chart anymore.

The quadrupole deformation of the first $J^\pi = 0^+, 2^+$ states will be a follow-up to the present thesis work. A new dedicated experiment with AGATA will be performed at LNL: **Combined lifetime and transition- probability measurements in ^{96}Zr via unsafe Coulomb excitation**. *Spokespersons: M. Zielińska (CEA Saclay, France), F. Ercolano, N. Marchini (INFN Firenze), J.J. Valiente Dobón (INFN LNL).*

Bibliography

[1] National Nuclear Data Center. `http://www.nndc.bnl.gov/`. [Online; accessed 2-March-2024].

[2] M. Goeppert Meyer. On closed shells in nuclei. *Physical Review*, 75(12):1969, 1949.

[3] O. Haxel, J. Hans, D. Jensen, and H.E. Suess. On the "magic numbers" in nuclear structure. *Physical Review*, 75(11):1766, 1949.

[4] K.S. Krane. *Introductory nuclear physics*. John Wiley & Sons, 1991.

[5] R.R. Roy and P.B. Nigam. *Nuclear physics: theory and experiment*. John Wiley & Sons, 1967.

[6] C.A. Bertulani. *Nuclear physics in a nutshell*. Princeton University Press, 2007.

[7] L. Fortunato. Solutions of the Bohr Hamiltonian, a compendium. *The European Physical Journal A - Hadrons and Nuclei*, 26(Suppl 1):1, 2005.

[8] P. Butler. Octupole collectivity in nuclei. *Journal of Physics G: Nuclear and Particle Physics*, 43(7):073002, 2016.

[9] E. Cheifetz, R.C. Jared, S.G. Thompson, and J.B. Wilhelmy. Experimental information concerning deformation of neutron-rich nuclei in the $A \sim 100$ region. *Physical Review Letters*, 25(1):38, 1970.

[10] A. Görgen and W. Korten. Coulomb-excitation studies of shape coexistence in atomic nuclei. *Journal of Physics G: Nuclear and Particle Physics*, 43(2):024002, 2016.

[11] K. Heyde and J.L. Wood. Shape coexistence in atomic nuclei. *Reviews of Modern Physics*, 83(4):1467, 2011.

[12] H. Morinaga. Interpretation of some of the excited states of 4n self-conjugate nuclei. *Physical Review*, 101(1):254, 1956.

[13] B.A. Marsh, T. Day Goodacre, S. Sels, et al. Characterization of the shape-staggering effect in mercury nuclei. *Nature Physics*, 14(12):1163, 2018.

[14] A.N. Andreyev, M. Huyse, P. Van Duppen, et al. A triplet of differently shaped spin-zero states in the atomic nucleus ^{186}Pb. *Nature*, 405(6785):430, 2000.

[15] A. Chakraborty, E.E. Peters, B.P. Crider, et al. Collective structure in ^{94}Zr and subshell effects in shape coexistence. *Physical Review Letters*, 110:022504, 2013.

[16] N. Paul, A. Corsi, A. Obertelli, et al. Are there signatures of harmonic oscillator shells far from stability? First spectroscopy of ^{110}Zr. *Physical Review Letters*, 118:032501, 2017.

[17] T. Togashi, Y. Tsunoda, T. Otsuka, and N. Shimizu. Quantum phase transition in the shape of Zr isotopes. *Physical Review Letters*, 117:172502, 2016.

[18] T. Kibedi and R.H. Spear. Reduced electric-octupole transition probabilities, $B(E3; 0_1^+ \rightarrow 3_1^-)$ - An update. *Atomic data and nuclear data Tables*, 80(1):35, 2002.

[19] Ł.W. Iskra, R. Broda, R.V.F. Janssens, et al. Revised $B(E3)$ transition rate and structure of the 3^- level in ^{96}Zr. *Physics Letters B*, 788:396, 2019.

[20] I-Y. Lee. The GAMMASPHERE. *Nuclear Physics A*, 520:c641, 1990.

[21] D.J. Horen, R.L. Auble, G.R. Satchler, et al. Lifetime of the 3_1^- state and octupole collectivity in ^{96}Zr. *Physical Review C*, 48:R2131, 1993.

[22] C.A. Bertulani. Theory and applications of Coulomb excitation, 2009. arXiv:0908.4307.

[23] K. Alder and A. Winter. *Electromagnetic excitation*. North-Holland, 1975.

[24] R. Bass. *Nuclear reactions with heavy ions*. Springer Berlin, Heidelberg, 1980.

[25] D. Cline. Nuclear shapes studied by Coulomb excitation. *Annual Review of Nuclear and Particle Science*, 36(1):683, 1986.

[26] GOSIA: Coulomb excitation code. `https://www.pas.rochester.edu/%7Ecline/Gosia/index.html`. [Online; accessed 2-March-2024].

[27] GOSIA user manual. `http://www.pas.rochester.edu/~cline/Gosia/Gosia_Manual_20120510.pdf`. [Online; accessed 2-March-2024].

[28] L.C. Feldman and J.W. Mayer. *Fundamentals of surface and thin film analysis*. North-Holland, 1986.

[29] S. Akkoyun, A. Algora, B. Alikhani, et al. AGATA—Advanced GAmma Tracking Array. *Nuclear Instruments and Methods in Physics Research Section A: Accelerators, Spectrometers, Detectors and Associated Equipment*, 668:26, 2012.

[30] AGATA website. `https://www.agata.org/`. [Online; accessed 2-March-2024].

[31] INFN Legnaro National Laboratories photogallery. `https://gallery.lnl.infn.it/`. [Online; accessed 2-March-2024].

[32] P.-A. Söderström, F. Recchia, J. Nyberg, et al. Interaction position resolution simulations and in-beam measurements of the AGATA HPGe detectors. *Nuclear Instruments and Methods in Physics Research Section A: Accelerators, Spectrometers, Detectors and Associated Equipment*, 638:96, 2011.

[33] A.J. Boston, F.C.L. Crespi, G. Duchêne, et al. AGATA characterisation and pulse shape analysis. *The European Physical Journal A - Hadrons and Nuclei*, 59(9):213, 2023.

[34] A. Lopez-Martens, K. Hauschild, A. Korichi, J. Roccaz, and J.P. Thibaud. γ-ray tracking algorithms: a comparison. *Nuclear Instruments and Methods in Physics Research Section A: Accelerators, Spectrometers, Detectors and Associated Equipment*, 533:454, 2004.

[35] M. Rocchini, K. Hadyńska-Klęk, A. Nannini, et al. SPIDER: A Silicon PIe DEtectoR for low-energy Coulomb-excitation measurements. *Nuclear Instruments and Methods in Physics Research Section A: Accelerators, Spectrometers, Detectors and Associated Equipment*, 971:164030, 2020.

[36] J.J. Valiente-Dobón, R Menegazzo, A Goasduff, et al. Conceptual design of the AGATA 2π array at LNL. *Nuclear Instruments and Methods in Physics Research Section A: Accelerators, Spectrometers, Detectors and Associated Equipment*, 1049:168040, 2023.

[37] Mesytec Website. `https://www.mesytec.com/`. [Online; accessed 2-March-2024].

[38] CAEN Website. `https://www.caen.it/`. [Online; accessed 2-March-2024].

[39] A. Korichi, E. Clément, N. Dosme, et al. AGATA DAQ-box: a unified data acquisition system for different experimental conditions. *The European Physical Journal A - Hadrons and Nuclei*, 59:211, 2023.

[40] D. Bazzacco, unpublished.

[41] R. Brun and F. Rademakers. ROOT — An object oriented data analysis framework. *Nuclear Instruments and Methods in Physics Research Section A: Accelerators, Spectrometers, Detectors and Associated Equipment*, 389:81, 1997.

[42] B. Bruyneel, B. Birkenbach, and P. Reiter. Pulse shape analysis and position determination in segmented HPGe detectors: The AGATA detector library. *The European Physical Journal A - Hadrons and Nuclei*, 52:70, 2016.

[43] B. Bruyneel, B. Birkenbach, J. Eberth, et al. Correction for hole trapping in AGATA detectors using pulse shape analysis. *The European Physical Journal A - Hadrons and Nuclei*, 49, 2013.

[44] FILIPPO ANGELINI. Commissioning of the agata gamma-ray tracking array. 2022.

[45] D.C. Radford. ESCL8R and LEVIT8R: Software for interactive graphical analysis of HPGe coincidence data sets. *Nuclear Instruments and Methods in Physics Research Section A: Accelerators, Spectrometers, Detectors and Associated Equipment*, 361:297, 1995.

[46] AGATA Root selector. `https://baltig.infn.it/gamma/agataselector/`. [Online; accessed 2-March-2024].

[47] LISE++ webpage. `https://lise.nscl.msu.edu/lise.html`. [Online; accessed 2-March-2024].

[48] BrIcc conversion coefficient database. `https://bricc.anu.edu.au/`. [Online; accessed 2-March-2024].

[49] J.F. Ziegler, M.D. Ziegler, and J.P. Biersack. Srim–the stopping and range of ions in matter (2010). *Nuclear Instruments and Methods in Physics Research Section B: Beam Interactions with Materials and Atoms*, 268:1818, 2010.

[50] M. Marchini, M. Rocchini, A. Nannini, et al. Shape coexistence in ^{94}Zr studied via Coulomb excitation. *The European Physical Journal - Web of Conferences*, 223:01038, 2019.

[51] G. Molnár, T. Belgya, B. Fazekas, et al. Particle-hole and vibrational states in doubly closed subshell ^{96}Zr from in-beam inelastic neutron and proton scattering. *Nuclear Physics A*, 500:43, 1989.

[52] G. Molnár, H. Ohm, G. Lhersonneau, and K. Sistemich. Enhanced octupole collectivity at double subshell closure in the ^{96}Zr region. *Zeitschrift für Physik A Atomic Nuclei*, 331:97, 1988.

[53] G. Klein, N. Kaffrell, N. Trautmann, G. Herrmann, et al. Identification of ^{96}Y in fission by a rapid chemical separation procedure. *Inorganic and Nuclear Chemistry Letters*, 11:511, 1975.

[54] G. Sadler, T.A. Khan, K. Sistemich, et al. Studies of the β-decay of ^{96}Y and the level scheme of ^{96}Zr. *Nuclear Physics A*, 252:365, 1975.

[55] M.L. Stolzenwald, G. Lhersonneau, S. Brant, et al. The$[g_{9/2}]8^+$ state in ^{96}Zr. *Zeitschrift für Physik A Atomic Nuclei*, 327:359, 1987.

[56] H. Mach, S. Wiok, W. Nazarewicz, et al. Strong octupole and dipole collectivity in ^{96}Zr: Indication for octupole instability in the $A = 100$ mass region. *Physical Review C*, 42:R811, 1990.

[57] H. Ohm, M. Liang, Molnár G., et al. Strong harmonic $E3$ vibrations in ^{96}Zr. *Physics Letters B*, 241:472, 190.

Ringraziamenti

Desidero dedicare questo spazio del presente elaborato a tutti coloro che hanno contribuito alla realizzazione dello stesso.

Innanzitutto ringrazio la Commissione Scientifica Nazionale 3 dell'INFN per avermi introdotta alla ricerca tramite una borsa di studio nell'ambito della struttura nucleare. Questa opportunità mi ha permesso di conoscere e di collaborare con la prof.ssa Adriana Nannini, la dott.ssa Naomi Marchini e il prof. Marco Rocchini dei quali ammiro carattere ed attitudine positiva in ogni circostanza. Sono stata accolta con cura e fiducia e nonostante le tempistiche ridotte ho sempre ricevuto supporto ed incoraggiamento per poter lavorare in tranquillità. Esprimere la mia profonda gratitudine è difficile ed è per questo che posso solo limitarmi a ringraziare la prof.ssa Nannini che nei momenti di sconforto con poche parole è riuscita subito a riorientarmi, la dott.ssa Marchini per essere stata una guida durante tutto il percorso, mostrandomi come affrontare con metodo e risolutezza le difficoltà riscontrate durante l'analisi, ed infine il prof. Rocchini per aver svoltato la fase finale del lavoro dedicandomi prezioso tempo per lunghe e dettagliate spiegazioni.

Ringrazio il dott. Massimo Chiari per avermi seguita nella fase di misure per la caratterizzazione del target presso il LABEC.

I tre mesi trascorsi presso i Laboratori Nazionali di Legnaro sono stati senza dubbio il periodo più stimolante ed arricchente del mio percorso universitario. Ringrazio il dott. José Javier Valiente Dobón e tutti i ricercatori, postdoc e dottorandi che ho incontrato per avermi fatto capire cosa significa vivere di ricerca. In particolare, un sentito ringraziamento va al dott. Daniele Brugnara per essere stato un punto di riferimento durante tutte le fasi dell'analisi. Senza il suo fondamentale contributo tutto sarebbe proceduto più lentamente.

Tornando alle mie radici, ringrazio il prof. Di Leva per aver seguito il lavoro con entusiasmo ed attenzione. Ringrazio, inoltre, il prof. Di Nitto per gli importanti spunti di riflessione emersi durante gli incontri di correlazione. Più in generale, ringrazio tutti i professori che ho incontrato in questi anni. Custodisco con cura gli insegnamenti ricevuti.

Nulla di tutto questo sarebbe stato possibile senza mia mamma, mio papà e mio fratello Vincenzo. Grazie, perchè in qualunque mio passo di questo cammino so di non essere mai sola.

Nessuno riesce a capirti meglio di chi vive le tue stesse esperienze e per me Imma ne è l'esempio. Grazie per aver gioito ad ogni traduardo ed avermi incoraggiato nei momenti più difficili. La tua tenacia è da sempre un esempio.

Infine, la mia sincera riconoscenza agli amici di sempre, fonte inesauribile di sollievo per la testa ed il cuore. Grazie Giovanna, per essere stata la scoperta di questi ultimi anni, uno spirito forte in cui trovare confronto e conforto. A Francesco, Davide e Piergiorgio che sono ormai parte di me, semplicemente grazie.